2014

Coupled mechanochemical theories for reacting systems with application to nanovoid nucleation and Li-ion batteries

Hamed Attariani
Iowa State University

Coupled mechanochemical theories for reacting systems with application to nanovoid nucleation and Li-ion batteries

by

Hamed Attariani

A dissertation submitted to the graduate faculty

in partial fulfillment of the requirements for the degree of

DOCTOR OF PHILOSOPHY

Major: Engineering Mechanics

Program of Study Committee:

Valery I. Levitas, Major Professor

Ashraf Bastawros

Thomas Rudolphi

Pranav Shrotriya

Baskar Ganapathysubramanian

Iowa State University

Ames, Iowa

2014

DEDICATION

I would like to dedicate this thesis to my parents

for their love, support, patience, and sacrifice.

TABLE OF CONTENTS

LIST OF TABLES v

LIST OF FIGURES vi

ACKNOWLEDGEMENTS ix

CHAPTER 1. GENERAL INTRODUCTION 1

1.1 Introduction: Li-ion batteries 1

1.2 Introduction: Hollow nanoparticles 1

1.3 Thesis Organization 3

CHAPTER 2. ANISOTROPIC COMPOSITIONAL EXPANSION IN ELASTO-PLASTIC MATERIALS AND CORRESPONDING CHEMICAL POTENTIAL: LARGE-STRAIN FORMULATION AND APPLICATION TO AMORPHOUS LITHIATED SILICON 7

Abstract 7

2.1 Introduction 8

2.1.1 Thermodynamic treatment of insertion-extraction in elastoplastic material 11

2.1.2 Chemical potential and compositional deformation gradient tensor . . . 14

2.1.3 Plastic Flow Rule 24

2.1.4 Specification of the Constitutive Equations 26

2.1.5 Relationships for Alternative Kinematic Decomposition 29

2.1.6 Verification and Application of the Developed Model 32

2.2 Concluding remarks 43

CHAPTER 3. MECHANOCHEMICAL CONTINUUM MODELING OF NANOVOID NUCLEATION AND GROWTH IN REACTING NANOPARTICLES 57

Abstract 57

3.1 Introduction 58

3.1.1 Governing equations 59

3.1.2 Complete coupled system of equations 66

3.1.3 Void Nucleation Criterion 69

3.1.4 Numerical Method 70

3.1.5 Void and Oxide Growth 72

3.1.6 Comparison with existing approaches 77

3.1.7 Concluding Remarks 78

CHAPTER 4. GENERAL CONCLUSIONS 83

APPENDIX A. DERIVATION OF THE CONSTITUTIVE EQUATION FOR k USING THE POSTULATE OF REALIZABILITY 85

APPENDIX B. APPLICATION OF THE POSTULATE OF REALIZABILITY TO COMPOSITIONAL DISSIPATION RATE 88

APPENDIX C. CHOICE OF THE GENERALIZED THERMODYNAMIC FORCES AND RATES 90

APPENDIX D. SMALL ELASTIC STRAIN APPROXIMATION FOR A THIN FILM AT RIGID SUBSTRATE: ANALYTICAL SOLUTION . . . 92

LIST OF TABLES

2.1 Material properties 34

LIST OF FIGURES

2.1 (a) Anisotropic compositional deformation of Li_xSi during lithiation under deviatoric stresses. (b) When deviatoric stress $\boldsymbol{S}$, applied to a sample, produces the same driving force for insertion and extraction, the Li_xSi sample may be fluctuationally divided into two samples separated by an interface, in one of which insertion occurs and in the other extraction takes place. 23

2.2 Magnitude of the Li flux vs. chemical potential of Li reservoir μ_r under deviatoric stresses (solid line, Eq. (40)). 23

2.3 Schematics of thin film and boundary conditions. The film is constrained at the lateral sides. The Li concentration is homogeneous throughout the film. 35

2.4 Simulated biaxial stress $\sigma(x)$ during lithiation-delithiation of a thin-film on a rigid substrate based on the current theory in comparison with experimental results and atomistic simulations from [20]. Very good correspondence is observed with just single-material parameter Λ fitted to reproduce experiment and DFT simulations at $x = 2$. 36

2.5 (a) Reduction in biaxial stress with time after near completion of delithiation ($x = a$ in Fig. 2.4) under oscillatory change in x. (b) Keeping tensile stresses below 0.8 GPa during delithiation by superposition of multiple oscillatory change in x, $x = x_0 + 0.01cos(\tilde{t})$ when stress reaches 0.8 GPa until it reduces to zero. 37

2.6 Schematics of thin film and boundary conditions. The Li concentration is obtained by solving the diffusion equation. 38

2.7 Variation of average lateral stress σ vs. averaged Li concentration during lithiation and delithiation of a thin film on a rigid substrate for heterogeneous problem involving diffusion. 39

2.8 Time evolution of distribution of Li concentration x (a and c) and lateral stress σ (b and d) for lithiation (a and b) and delithiation (c and d) of a thin film on a rigid substrate. 40

2.9 Comparison of time evolution of Li concentration x for initial time steps with and without excess energy for lithiation/delithiation of a thin film on a rigid substrate. 41

2.10 Effect of the parameter ζ, which is partitioning the part of the compositional stress power that dissipates and the part that contributes to the chemical potential on the Li concentration distribution in a thin film on a rigid substrate for the charging rate $C/0.55$ and $h_0 = 500$ nm. 41

2.11 Schematics of solid nanoparticle and boundary conditions. The surface is traction free. 42

2.12 Concentration (a and d), radial (b and e), and hoop (c and f) stress evolution for lithiation (a-c) and delithiation (d-f) of a solid spherical nanoparticle. 44

2.13 Hoop stress for the surface and the center of a solid nanoparticle during lithiation (a) and delithiation (b). 45

2.14 Schematic of a hollow nanoparticle and its boundary conditions. All surfaces are traction free. 45

2.15 Concentration (a and d), radial (b and e), and hoop (c and f) stress evolution for lithiation (a-c) and delithiation (d-f) of a hollow spherical nanoparticle. 46

2.16 Hoop stress for the outer surface and the inner surface of a hollow nanoparticle during lithiation (a) and delithiation (b). 47

2.17 Hoop stress for the outer surface of different hollow nanoparticles during lithiation with and without relaxation. 47

3.1 Particle geometry: (1) before void nucleation, (2) with all three regions, (3) after metal core disappeared. 60

3.2 Equilibrium concentration of vacancies (Eq.(35)) at the surface of void consisting of q vacancies vs. temperature for different external pressures at the void surface: (a) $p(a)$ =2 GPa, (b) $p(a)$ =0.716 GPa, and (c) $p(a) = 0$. 71

3.3 Oxide layer thickness vs. time for Cu NP of four different core radii: lines are results of simulations, and symbols are experiments from (4); (a) $\theta = 323\,K$, (b) $\theta = 343\,K$, and (c) $\theta = 373\,K$. 73

3.4 Evolution of distribution of vacancy concentration in a core and Cu atoms in a shell for $R_c = 9.05\,nm$ at $\theta = 373\,K$. 75

3.5 Evolution of distribution of vacancy concentration in a core (a) and Cu atoms in a shell (b), as well as pressure in a core (c) for $R_c = 9.05\,nm$ at $\theta = 373\,K$ during the nanovoid growth. 76

3.6 Variation of void radius vs. time for three particle sizes at $\theta = 373\,K$. 77

A.1 Variation of $\Delta\mu(\mathcal{B}, \boldsymbol{k}^*)$ vs. $\boldsymbol{k}^*$ for arbitrarily fixed parameters $\mathcal{B}$ for insertion (a) and extraction (b). 86

D.1 In-plane compositional strain ε_{c2}^{L} (a) and biaxial stress (b) vs. compositional Jacobian for different Λ for lithiation. 93

ACKNOWLEDGEMENTS

I would like to take this opportunity to express my thanks to those who helped me with various aspects of conducting research and writing of this thesis. First and foremost, Dr. Valery I. Levitas for his support throughout this research. I would also like to thank my committee members for their efforts: Dr. Ashraf Bastawros, Dr. Thomas Rudolphi, Dr. Pranav Shrotriya, and Dr. Baskar Ganapathysubramanian. I would additionally like to thank Dr. Mitra, Dr. Sturges, and Dr. Dayal for their inspirational teaching style which led me to a better understanding of my future career goal as a faculty member.

CHAPTER 1. GENERAL INTRODUCTION

1.1 Introduction: Li-ion batteries

Li-ion batteries have attracted great attention throughout the world as rechargeable energy sources. A wide variety of anode materials, including $Si, Sn, C, Sb, Al, Mg, Bi$ [1], $Li_4Ti_5O_{12}$ [2] and transition-metal oxides [3] were extensively studied for their potential in building high-performance batteries. Among these possible anode materials, silicon appears to be most promising because of its large capacity (four times that of traditional anodes). However, the large volumetric expansion and subsequent mechanical failure caused by the insertion of Li represents a significant obstacle hindering the widespread application of Si as an anode [4–8]. As a solution to this problem, researchers are trying the alternative of reducing system size and using nano-structures to reduce the anode stress [9–12]. The first step in understanding the failure mechanism was to model the stress generated during the lithiation/delithiation process. The experimental results show that the induced stress at the fully lithiated or delithiated thin film is on the order of $1 - 2GPa$, below the yield stress of amorphous Si [13, 14]. However, in current models [13, 15–17], plasticity is assumed to be the stress-relaxation mechanism, so there is a need to develop a new stress relaxation model that allows system stress to relax below the yield stress. For this purpose, a new anisotropic compositional strain model in amorphous Si anodes was developed; it excludes plasticity as the dominant factor in stress relaxation and introduces a novel concept for stress relaxation occurring below the yield stress.

1.2 Introduction: Hollow nanoparticles

The specific optical, electrical, magnetic, and thermal properties of hollow nanoparticles make them prominent candidates for biomedical applications (drug delivery, disease diagnosis,

and cancer therapy), lightweight filters, composites, catalysts, waste treatment, insulators, and photoelectric devices [18, 19]. To synthesize a hollow nanoparticle with proper properties, we first must understand the mechanisms and parameters that affect void nucleation and growth to control the synthesis process, so extensive experimental studies have been done on void formation in Cu, Al, Fe, Zn, Co, Mg, Ni, and Cd NPs [20–28]. The oxidation process is a simple method for producing hollow NPs [20–24]. In this case, because of differences in diffusivity of metal atoms in core (metal) and shell (oxide), a net vacancy flux flows toward the core and results in supersaturation of vacancies and nanovoid nucleation. This phenomena can be modeled by the Kirkendall effect [29]. In this section, the experimental and numerical studies on hollow formation of Cu NPs will be summarized.

Experimental studies: Hung, et al. [21] have produced Cu NPs with thermal decomposition of copper (I) acetate (CuOAc) in trioctylamine (TOA). They observed that different solvents (hexane and chloroform) form different final structures (solid and hollow oxidized NPs) at room temperature, and they concluded that differences in solubility of oxygen in different solvents causes this phenomenon. Nakamura et al. [20, 22] have exposed Cu nanoparticles to air at 373 K for 3.6 ks and found that the oxide thickness (Cu_2O) increases to a certain limiting thickness that depends on the diameter of the NPs. In their experiments a single void appears at the center of a NP and oxide thickness is approximately uniform. *Theoretical studies:* Atomistic methods have their own limitations with respect to size and time scales, so one must work near the melting temperature to be capable of modeling void nucleation and growth using these methods [28,29]. However, hollow formation can occur near room temperature [20,21,23] and continuum approaches can overcome this limitation. In continuum approaches [30–32], nucleation of void and mechanics were neglected. The common wisdom in these approaches is that the void nucleates due to tensile stress in the core [32]. This hypothesis also explains the difference between the calculated growth time and the experimental growth time. However, surface tension induces compressive stress in the core, and this compressive pressure can reduce the equilibrium concentration of vacancies and promote void nucleation. A comprehensive model is thus needed to consider all these parameters and use to predict hollow formation.

1.3 Thesis Organization

Chapter 2 describes development of a general large-strain thermodynamic approach introducing anisotropic (tensorial) compositional expansion/contraction in elastoplastic material under stress tensor. Employing a consistent thermodynamic method, a simple kinetic equation for the deviatoric part of the compositional deformation rate is derived and introduced as the new mechanism for stress relaxation below the yield stress. Consequently, a nontrivial expression for the chemical potential is found, and this new chemical potential has an additional term resulting from deviatoric stresses, resulting in an increase in the driving force for both compositional expansion and contraction. This coupled diffusion and mechanical model is applied to lithiation and delithiation of thin-film, solid, and hollow spherical nanoparticles.

Chapter 3 describes development of a coupled continuum-mechanics approach for nucleation and growth of a nanovoid in reacting nanoparticles (copper nanoparticles). The effects of several parameters (i.e. pressure, temperature, and size of a vacancy) on void nucleation criteria are investigated. The results show that compressive pressure and reduced temperature increases void nucleation probability. This is explained by decreasing in the equilibrium concentration of vacancies at the void surface. Finally, a method for controlling void nucleation and growth is suggested.

Bibliography

[1] Zhang, S. S. *J. Power Sources*, **2006**, 162, 1379.

[2] Tang, Y.; Yang, L.; Qiu, Z.; Huang, J. *J. Mater. Chem.*, **2009**, 19, 5980.

[3] Poizot, P.; Laruelle, S.; Grugeon, S.; Dupont, L.; Tarascon, J. M. *Nature*, **2000**, 407, 496.

[4] Bhandakkar, T.K.; Gao, H.J. *Int. J. Solids Struct.*, **2010** 47, 1424-34.

[5] Bhandakkar, T.K.; Gao, H.J. *J. Mech. Phys. Solids*, **2011**, 48, 23042309.

[6] Haftbaradaran, H. and Gao, H.J. *Appl. Phys. Lett.*, **2012**, 100, 121907.

[7] Hu, Y.H.; Zhao, X.H.; Suo, Z. *J. Mater. Res.*, **2010**, 25, 1007-1010.

[8] McDowell, M.T.; Ryu, L.; Lee, S.W.; Wang, C.; Nix, W.D.; Cui, Y. *Adv. Mater.*, **2012** 24, 6034-6041.

[9] Arico, A.S.; Bruce, P.; Scrosati, B.; Tarascon, J.M.; Schalkwijk, W.V. *Nat. Mater.*, **2005**, 4, 366-377.

[10] Chan, C.K.; Peng, H.; Liu, G.; McIlwrath, K.; Zhang, X.F.; Huggins, R.A.; Cui, Y. *Nat. Nanotechnol.*, **2008**, 3, 31-35.

[11] Liu, X.H.; Wang, J.W.; Huang, S.; Fan, F.; Huang, X.; Liu, Y.; Krylyuk, S.; Yoo, J.; Dayeh, S.A.; Davydov, A.V.; Mao, S.X.; Picraux, S.T.; S., Zhang; Li, J.; Zhu, T.; Huang, J.Y. *Nat. Nanotechnol.*, **2012**, 7, 749-756.

[12] Wu, H.; Chan, G.; Choi, J.W.; Ryu, I.; Yao, Y.; McDowell, M.T.; Lee, S.W.; Jackson, A.; Yang, Y.; Hu, L.; Cui, Y. *Nat. Nanotechnol.*, **2012**, 7, 310-315.

[13] Zhao, K.; Tritsaris, G.A.; Pharr, M.; Wang, W.L.; Okeke, O.; Suo, Z.; Vlassak, J.J.; Kaxiras, E. *Nano Lett.*, **2012**, 12, 4397-4403.

[14] Sethuraman, V.; Srinivasan, A.F.; Bower, Guduru; P.R. *J. Electrochem. Soc.*, **2010**, 157, A1253-A1261.

[15] Bower, A.F.; Guduru, P.R.; Sethuraman, V.A. *J. Mech. Phys. Solids*, **2011**, 59, 804-828.

[16] Cui, Z.; Gao, Z.; Qu, J. **J. Mech. Phys. Solids**, *2012*, 60, 1280-1295.

[17] Zhao, K.; Pharr, M.; Cai, S.; Vlassak, J.J.; Suo, Z. *J. Am. Ceram. Soc.*, **2011**, 94, S226-S235.

[18] Hosokawa, M.; Nogi, K.; Naito, M.; Yokoyama, T. Nanoparticle technology handbook; Elsevier, 2007; p 100.

[19] Shpak, A. P.; Gorbyk, P. P. Nanomaterials and Supramolecular Structures: Physics, Chemistry, and Applications; Springer, 2009; p 207.

[20] Tokozakura, D.; Nakamura, R.; Nakajima, H.; Lee, J. G.; Mori, H. *J. Mater. Res.* **2007**, 22, 2930-2935.

[21] Hung, L. I; Tsung, C. K; Huang, W.; Yang, P. *Adv. Mater.* **2010**, 22, 1910-1914.

[22] Nakamura, R.; Tokozakura, D.; Nakajima, H.; Lee, J. G.; Mori, H. *J. Appl. Phys.* **2007**, 101, 074303.

[23] Wang, C. M.; Baer, D. R.; Thomas, L. E.; Amonette, J. E.; Antony, J.; Qiang, Y.; Duscher, G. *J. Appl. Phys.* **2005**, 98, 094308.

[24] Cabot, A.; Puntes, V. F.; Shevchenko, E.; Yin, Y.; Balcells, L.; Marcus, A. M.; Hughes, M.; Alivisatos, A. P. *J. Am. Chem. Soc.* **2007**, 129, 10358-10360.

[25] Yin, Y.; Erdonmez, C. K; Cabot, A.; Hughes, M.; Alivisatos, A. P. *Adv. Funct. Mater.* **2006**, 16, 1389-1399.

[26] Cabot, A.; Ibanez, M.; Guardia, P.; Alivisatos, A. P. *J. Am. Chem. Soc.* **2009**, 131, 11326-11328.

[27] Smigelskas, A. D; Kirkendall, E. O. *Trans. Am. Inst. Min. Metall. Eng.* **1947**, 171, 130-142.

[28] Evteev, A. V.; Levchenko, E. V.; Belova, I. V.; Murch, G. E. *J. Nano Res.* **2009**, 7, 11-17.

[29] Gusak, A. M; Zaporozhets, T. V. *Phys. Condens. Matter.* **2009**, 21, 415303.

[30] Yu, H. C.; Yeon, D. H.; Li, X. F.; Thornton, K. *Acta Mater.* **2009**, 57, 5348-5360.

[31] Gusak, A. M.; Tu, K. N. *Acta Mater.* **2009**, 57, 3367-3373.

[32] Svoboda, J.; Fischer, F. D.; Vollath, D. *Acta Mater.* **2009**, 57, 1912-1919.

CHAPTER 2. ANISOTROPIC COMPOSITIONAL EXPANSION IN ELASTOPLASTIC MATERIALS AND CORRESPONDING CHEMICAL POTENTIAL: LARGE-STRAIN FORMULATION AND APPLICATION TO AMORPHOUS LITHIATED SILICON

Modified from papers published in the Journal of Mechanics and Physics of Solids and Scientific Report

Valery I. Levitas[1] and Hamed Attariani [2]

ABSTRACT

A general large-strain thermodynamic approach with anisotropic (tensorial) compositional expansion/contraction in elastoplastic material under stress tensor is developed. The dissipation rate due to compositional expansion/contraction is introduced. Adapting and utilizing a previously formulated postulate of realizability, we derived a simple equation for the deviatoric part of the compositional deformation rate. This leads to a nontrivial generalization of the concept and expression for the chemical potential. It receives a contribution from deviatoric stresses, which leads to an increase in the driving force for both the compositional expansion and contraction and to some new phenomena. Our model provides a remarkable description of the known experimental and atomistic simulation data on the biaxial stress evolution during lithiation-delithiation of Li_xSi on a rigid substrate with just one constant kinetic coefficient. In contrast to known approaches, it does not involve plasticity, because the yield strength is higher than the stresses generated during lithiation-delithiation. This allowed us to suggest a method for reduction in internal stresses by cyclic change in Li concentration with a small

[1]Iowa State University, Departments of Aerospace Engineering, Mechanical Engineering, and Material Science and Engineering, Ames, Iowa 50011, U.S.A.

[2]Iowa State University, Department of Aerospace Engineering, Ames, Iowa 50011, U.S.A.

amplitude, and our simulations were in qualitative agreement with known experiments. The coupled diffusion and mechanical model was applied to lithiation and delithiation of thin-film, solid, and hollow spherical nanoparticles. The importance of the contribution of the deviatoric stress on the diffusion is demonstrated.

2.1 Introduction

Starting with the celebrated work by [1,2], the concept of the chemical potential of multi-component materials with diffusion under nonhydrostatic stresses received significant development. More recent large-strain formulations have been presented in [3–7]. Practical motivation for large-strain formulations was recently received from the development of lithium-ion batteries. In particular, Si is a promising anode material for Li-ion batteries since it is able to absorb a large amount of Li [8,9]. The maximum insertion of Li corresponds to $Li_{4.4}S$, which possesses a theoretical Li capacity of 4200 mAh/g, an order of magnitude larger than for a graphite anode [8,9]. However, insertion of such an amount of Li is accompanied by a 334% volumetric expansion, which under constraint conditions leads to huge stresses that may cause fracture of an Li_xSi anode [10–14]. This is one of the main problems that prevents industrial application of Si anodes, and it is why understanding of the stress development and relaxation during lithiation-delithiation is of great applied and basic importance. For nanoscale anodes (nanowires, particles, and films [15–18]), fracture is suppressed, and large compositional volumetric deformations of Li_xSi under constrained conditions are believed to be accommodated by plastic flow [5,6,19,20]. All continuum approaches to stress relaxation in Li_xSi anodes are based on classical viscoplasticity theory [5,6,19,20], but recent density functional theory (DFT) simulations [20] have demonstrated that the yield strength of Li_xSi is at least two times higher than the stresses generated during lithiation-delithiation in a thin film on a rigid substrate for all x. This practically excludes plasticity as a relaxation mechanism and requires approaches different from those in [5], [19,20], and [6]. The fact that atomistic simulations for crystalline materials without defects (for example, dislocations and grain boundaries) usually overestimate the yield strength cannot be used as an excuse. For amorphous nanomaterial, the same atomistic calculations [20] describe satisfactory experimental data on biaxial stress

relaxation in Si film during insertion-extraction. In the most recent model [21, 22], the flow (change in shape) and reaction (change in composition) are assumed to be the concurrent non-equilibrium processes that are coupled thermodynamically. It has two fitting material parameters, but it was not checked against atomistic calculations or experiments. One of our goals in this paper was to suggest and develop a different approach in which stress relaxation in Li_xSi anodes occurs not due to classical plasticity when the yield condition is satisfied but due to anisotropic (tensorial) compositional straining that occurs during insertion-extraction reaction at any deviatoric stresses (i.e., below the yield strength). The anisotropic swelling in nanowires was observed and modeled in [23] and [24]. The source of anisotropy is orientation-dependent mobility of the core/shell interface, where the core is the crystalline Si and the shell is the amorphous Si, which is much different from the model considered here. Also, plasticity is the active mechanism for the stress relaxation in [23] and [24]. Here, we derive constitutive equations for anisotropic compositional expansion in a material point–i.e., without involving interfaces. [25] and [26] showed that the first lithiation of amorphous Si thin film and nanoparticles is an interface-controlled process rather than diffusion-controlled. However, after the first cycle, the amorphous-amorphous interface disappears, and diffusion becomes the rate-controlling mechanism which means that our approach can be used after the first cycle of lithiation. Using the irreversible thermodynamic approach and adapting a previously formulated postulate of realizability [7, 27–32], we derived a simple rate equation for the deviatoric part of the compositional deformation rate. This equation, together with the elasticity rule and just one fitted kinetic constant, provides a remarkable description of known experimental and atomistic simulation data on the biaxial stress evolution during lithiation-delithiation of Li_xSi on a rigid substrate [20]. This proves the conceptual correctness and necessity of using tensorial compositional strain for initially isotropic (amorphous) materials. After proving validity, we utilized the same model for justification of a method of reduction of internal stresses in a constrained Si anode by cyclic lithiation-delithiation with a small magnitude of variation in Li concentration. The results of our simulations are in qualitative agreement with available experiments [33]. Other problems related to coupled diffusion, compositional expansion, and stress generation and relaxation were solved with the finite-element method (FEM) for thin

film on substrate, solid, and hollow spherical Si anodes.

Tensorial compositional strain and the rate-type equation for it raise some additional questions. Traditionally, the compositional dissipation rate was assumed to be zero, which determined the explicit expression for the chemical potential. Here, we introduced a nonzero dissipation rate related to insertion-extraction as a part of the compositional stress power with some factor ζ $(0 \leq \zeta \leq 1)$, while another part of the compositional stress power with a factor $1-\zeta$ contributes to the chemical potential. In this way, a chemical potential receives additional contribution due to deviatoric stresses, which surprisingly leads to an increase in the driving force for both insertion and extraction simultaneously. This causes some problems in choosing, which process will in fact occur under deviatoric stresses. We postulated that the process leading to the minimal chemical potential will take place–namely, insertion–which leads to a nontrivial relationship for the flux of Li atoms vs. the driving force, including the jump in flux. While there no data to specify the factor ζ, the obtained jump in flux, if confirmed experimentally, would allow us to determine ζ. The effect of parameter ζ and the contribution to the chemical potential due to deviatoric stress on the diffusion is analyzed numerically.

While applications here are based on the simplest model without plasticity, it is clear that in the general case (for example, for a larger sample and a lower yield strength) a combination of anisotropic compositional expansion and classical plasticity should be considered. Our general theory includes both and resolves some related kinematic and thermodynamic issues. In particular, the advantage of additive decomposition of the inelastic deformation rate into compositional and plastic parts in comparison with multiplicative decomposition of the deformation gradient is demonstrated.

A similar approach is applicable to the lithiation-delithiation of other anode materials (for example, Sn) and to large compositional deformation and stress relaxation for other material systems. Also, such an approach can be applied to other processes such as chemical reactions and melting under nonhydrostatic conditions [34, 35] when anisotropic (tensorial) transformation strain can be introduced and described in a similar thermodynamic way. Some preliminary results were reported in a short letter [36].

Direct tensor notations are used. Vectors and tensors are denoted in boldface type; $\boldsymbol{A}\cdot\boldsymbol{B}$

and $\boldsymbol{A}:\boldsymbol{B}$ are the contraction of tensors over one and two indices. A superscript t and -1 denote transposition and inverse operations, subscript s means symmetrization of the tensors, $\boldsymbol{I}$ is the unit tensor of the second order, $dev\,\boldsymbol{A}$ is a deviatoric part of $\boldsymbol{A}$, $|\,\boldsymbol{A}\,| := \left(\boldsymbol{A}^t:\boldsymbol{A}\right)^{1/2}$ is the modulus (amplitude) of tensor $\boldsymbol{A}$, $\boldsymbol{\nabla}$ is the gradient operator in the undeformed configuration, $div = \boldsymbol{\nabla}\cdot$ is the divergence operator, and $:=$ means equals per definition.

2.1.1 Thermodynamic treatment of insertion-extraction in elastoplastic material

While the derivations below are generic for any material with compositional expansion, we will focus on insertion-extraction of the component A in the amorphous (isotropic) matrix B according to the equation $xA + B = A_xB$, where x is the number of moles of the component A per mole of the component B. In particular, we will consider insertion-extraction of Li in amorphous Si, $xLi + Si = Li_xSi$. The initial part of the thermodynamic derivations is similar to that in [2], [4], [5], and [7]. The kinematics of large deformations with multiple intermediate configurations is described in [37] and [30].

Kinematics. The motion of the elastoplastic material with insertion-extraction and diffusion will be described by a vector function $\boldsymbol{r} = \boldsymbol{r}(\boldsymbol{r}_0, t)$, where $\boldsymbol{r}_0$ and $\boldsymbol{r}$ are the positions of points in reference (undeformed) Ω_0 and the actual (deformed) Ω configurations, respectively; t is the time. The reference configuration is chosen to be undeformed component B,–i.e., the state with $x = 0$. The multiplicative decomposition of the deformation gradient, $\boldsymbol{F}$,

$$\boldsymbol{F} := \frac{\partial \boldsymbol{r}}{\partial \boldsymbol{r}_0} = \boldsymbol{F}_e\cdot\boldsymbol{F}_c\cdot\boldsymbol{F}_p, \tag{1}$$

into elastic, compositional (insertional), and plastic parts will be used. Plastic deformation gradient $\boldsymbol{F}_p$ transforms the reference configuration Ω_0 into the intermediate configuration Ω_p, and compositional deformation gradient $\boldsymbol{F}_c$ transforms the configuration Ω_p into the unloaded configuration Ω_c. Alternative kinematic decompositions will be considered in Section 6. We define the rate of deformation gradient as

$$\dot{\boldsymbol{F}} = \frac{\partial \boldsymbol{v}}{\partial \boldsymbol{r}_0} = \dot{\boldsymbol{F}}_e\cdot\boldsymbol{F}_c\cdot\boldsymbol{F}_p + \boldsymbol{F}_e\cdot\dot{\boldsymbol{F}}_c\cdot\boldsymbol{F}_p + \boldsymbol{F}_e\cdot\boldsymbol{F}_c\cdot\dot{\boldsymbol{F}}_p, \tag{2}$$

where $\boldsymbol{v} := \dot{\boldsymbol{r}}$ is the particle velocity, and the inverse deformation gradient as

$$\boldsymbol{F}^{-1} = \boldsymbol{F}_p^{-1}\cdot\boldsymbol{F}_c^{-1}\cdot\boldsymbol{F}_e^{-1}. \tag{3}$$

Then, the multiplicative decomposition Eq. (1) results in the additive decomposition of the velocity gradient $\boldsymbol{l} := \frac{\partial \boldsymbol{v}}{\partial \boldsymbol{r}} = \dot{\boldsymbol{F}} \cdot \boldsymbol{F}^{-1}$ and the deformation rate $\boldsymbol{d} := (\boldsymbol{l})_s$:

$$\boldsymbol{l} = \dot{\boldsymbol{F}}_e \cdot \boldsymbol{F}_e^{-1} + \boldsymbol{F}_e \cdot \dot{\boldsymbol{F}}_c \cdot \boldsymbol{F}_c^{-1} \cdot \boldsymbol{F}_e^{-1} + \boldsymbol{F}_e \cdot \boldsymbol{F}_c \cdot \dot{\boldsymbol{F}}_p \cdot \boldsymbol{F}_p^{-1} \cdot \boldsymbol{F}_c^{-1} \cdot \boldsymbol{F}_e^{-1} = \boldsymbol{l}_e + \boldsymbol{l}_c + \boldsymbol{l}_p, \tag{4}$$

$$\boldsymbol{d} = \left(\dot{\boldsymbol{F}}_e \cdot \boldsymbol{F}_e^{-1}\right)_s + \left(\boldsymbol{F}_e \cdot \dot{\boldsymbol{F}}_c \cdot \boldsymbol{F}_c^{-1} \cdot \boldsymbol{F}_e^{-1}\right)_s + \left(\boldsymbol{F}_e \cdot \boldsymbol{F}_c \cdot \dot{\boldsymbol{F}}_p \cdot \boldsymbol{F}_p^{-1} \cdot \boldsymbol{F}_c^{-1} \cdot \boldsymbol{F}_e^{-1}\right)_s = \boldsymbol{d}_e + \boldsymbol{d}_c + \boldsymbol{d}_p \tag{5}$$

into elastic, compositional, and plastic parts.

Mass balance. For the molar fraction of A per mole of B, x (similar, for Li and Si), the following mass-balance equation is valid in the reference configuration Ω_0:

$$\dot{x} + \bar{V}_B div\, \boldsymbol{j} = 0; \qquad \dot{x} + \bar{V}_{Si} div\, \boldsymbol{j} = 0, \tag{6}$$

where $\bar{V}_B$ and $\bar{V}_{Si}$ are the molar volumes of B and Si, and $\boldsymbol{j}$ is the flux of the A (or Li) diffusing constituent defined as a number of moles per unit reference area per unit time.

Thermodynamic laws. In the reference configuration Ω_0, consider a volume V_0 of multi-phase and multicomponent material with a boundary S_0. Allow, on one part of surface S_0^p the traction vector $\boldsymbol{p}_0$ to be prescribed and on the other part, S_0^u, the displacement vector $\boldsymbol{u}$ to be given, although mixed boundary conditions are also possible. We will use an energy balance equation (the first law of thermodynamics) and the entropy-balance equation combined with the Clausius-Duhem inequality (the second law of thermodynamics) for the whole volume V_0:

$$\int_{S_0} (\boldsymbol{p}_0 \cdot \boldsymbol{v} - \boldsymbol{h}_0 \cdot \boldsymbol{n}_0 - \mu \boldsymbol{j} \cdot \boldsymbol{n}_0)\, dS_0 - \frac{d}{dt} \int_{V_0} U\, dV_0 = 0\,, \tag{7}$$

$$S_{pr} := \frac{d}{dt} \int_{V_0} s\, dV_0 + \int_{S_0} \frac{\boldsymbol{h}_0}{\theta} \cdot \boldsymbol{n}_0\, dS_0 \geq 0\,. \tag{8}$$

Here, $\boldsymbol{h}_0$ is the heat flux, $\boldsymbol{n}_0$ is the unit normal to S_0, U is the specific (per-unit reference volume) internal energy, s is the specific entropy, S_{pr} is the total entropy production, $\theta \geq 0$ is the temperature, and μ is the chemical potential of the A. We will need the relationship $\boldsymbol{p}_0 = \boldsymbol{P} \cdot \boldsymbol{n}_0$ between the traction vector $\boldsymbol{p}_0$ and the first nonsymmetric Piola-Kirchoff (nominal) stress tensor $\boldsymbol{P}$–i.e., the force per unit area in the undeformed state. Using the Green-Gauss theorem to transform the surface-to-volume integrals, equation $\boldsymbol{p}_0 = \boldsymbol{P} \cdot \boldsymbol{n}_0$, $\nabla \boldsymbol{v} = \frac{\partial \boldsymbol{v}}{\partial \boldsymbol{r}_0} = \dot{\boldsymbol{F}}$, as well as the equilibrium equation $\boldsymbol{\nabla} \cdot \boldsymbol{P} = 0$, we transform Eqs. (7) and (8) to

$$\int_{V_0} \left(\boldsymbol{P}^t : \dot{\boldsymbol{F}} - \dot{U} - div\, \boldsymbol{h}_0 - div\,(\mu \boldsymbol{j})\right) dV_0 = 0\,, \tag{9}$$

$$S_{pr} := \int\limits_{V_0} \left(\dot{s} + div \, \frac{\boldsymbol{h}_0}{\theta} \right) \, d\, V_0 \geq 0 \, . \tag{10}$$

Due to local interaction, Eqs. (9) and (10) allow the equivalent local form

$$\boldsymbol{P}^t : \dot{\boldsymbol{F}} - \dot{U} - div \, \boldsymbol{h}_0 - \mu \, div \boldsymbol{j} - \boldsymbol{j} \cdot \boldsymbol{\nabla} \mu = 0 \, , \tag{11}$$

$$\tilde{S}_{pr} := \dot{s} + \frac{1}{\theta} \, div \, \boldsymbol{h}_0 - \frac{\boldsymbol{\nabla} \theta}{\theta^2} \cdot \boldsymbol{h}_0 \geq 0 \, , \tag{12}$$

where $\tilde{S}_{pr}$ is the local entropy production per unit reference volume. Excluding the expression $div \, \boldsymbol{h}_0$ from Eq. (11) and substituting it in Eq. (12) and multiplying by temperature, we obtain after evident transformations the following inequality:

$$\begin{aligned} \mathcal{D} := \theta \tilde{S}_{pr} = \boldsymbol{P}^t : \dot{\boldsymbol{F}} - \dot{U} + \theta \, \dot{s} - \frac{\boldsymbol{\nabla} \theta}{\theta} \cdot \boldsymbol{h}_0 - \mu \, div \, \boldsymbol{j} - \boldsymbol{j} \cdot \boldsymbol{\nabla} \mu = \\ = \boldsymbol{P}^t : \dot{\boldsymbol{F}} - \dot{\psi} - s \, \dot{\theta} - \frac{\boldsymbol{\nabla} \theta}{\theta} \cdot \boldsymbol{h}_0 - \mu \, div \, \boldsymbol{j} - \boldsymbol{j} \cdot \boldsymbol{\nabla} \mu \geq 0. \end{aligned} \tag{13}$$

Here, $\mathcal{D}$ is the rate of dissipation per unit volume in Ω_0, and $\psi = U - \theta \, s$ is the Helmholtz free energy per unit reference volume. Using the balance Eq. (6), we transform

$$\mathcal{D} = \boldsymbol{P}^t : \dot{\boldsymbol{F}} - \dot{\psi} - s \, \dot{\theta} - \frac{\boldsymbol{\nabla} \theta}{\theta} \cdot \boldsymbol{h}_0 + \bar{V}_B^{-1} \mu \, \dot{x} - \boldsymbol{j} \cdot \boldsymbol{\nabla} \mu \geq 0 \, . \tag{14}$$

We can define the chemical potential of A per unit volume of B,–i.e., per unit reference volume–as $\bar{\mu} := \bar{V}_B^{-1} \mu$. Alternatively, we can define the molar concentration of A per unit volume of B,–as $c := \bar{V}_B^{-1} x$,–i.e., the number of moles of A per unit reference volume. We assume that $\psi = \psi(\boldsymbol{F}_e, \boldsymbol{F}_c, \boldsymbol{F}_p, \theta, x)$, and substituting Eq. (2) and ψ in Eq. (14), we obtain

$$\begin{aligned} \mathcal{D} = \left(\boldsymbol{F}_c \cdot \boldsymbol{F}_p \cdot \boldsymbol{P}^t - \frac{\partial \psi}{\partial \boldsymbol{F}_e^t} \right) : \dot{\boldsymbol{F}}_e - \left(s + \frac{\partial \psi}{\partial \theta} \right) \dot{\theta} + \left(\frac{\mu}{\bar{V}_B} - \frac{\partial \psi}{\partial x} \right) \dot{x} + \\ \left(\boldsymbol{F}_p \cdot \boldsymbol{P}^t \cdot \boldsymbol{F}_e - \frac{\partial \psi}{\partial \boldsymbol{F}_c^t} \right) : \dot{\boldsymbol{F}}_c - \frac{\boldsymbol{\nabla} \theta}{\theta} \cdot \boldsymbol{h}_0 - \boldsymbol{j} \cdot \boldsymbol{\nabla} \mu + \left(\boldsymbol{P}^t \cdot \boldsymbol{F}_e \cdot \boldsymbol{F}_c : - \frac{\partial \psi}{\partial \boldsymbol{F}_p^t} \right) \dot{\boldsymbol{F}}_p \geq 0 \, . \end{aligned} \tag{15}$$

Then, the traditional assumption that the dissipation rate is independent of $\dot{\boldsymbol{F}}_e$ and $\dot{\theta}$ leads to the elasticity rule and the expression for entropy:

$$\boldsymbol{F}_c \cdot \boldsymbol{F}_p \cdot \boldsymbol{P}^t = \frac{\partial \psi}{\partial \boldsymbol{F}_e^t}; \qquad s = - \frac{\partial \psi}{\partial \theta}, \tag{16}$$

as well as to the residual dissipation inequality

$$\begin{aligned} \mathcal{D} = \left(\frac{\mu}{\bar{V}_B} - \frac{\partial \psi}{\partial x} \right) \dot{x} + \left(\boldsymbol{F}_p \cdot \boldsymbol{P}^t \cdot \boldsymbol{F}_e - \frac{\partial \psi}{\partial \boldsymbol{F}_c^t} \right) : \dot{\boldsymbol{F}}_c + \boldsymbol{X}_p^0 : \dot{\boldsymbol{F}}_p - \frac{\boldsymbol{\nabla} \theta}{\theta} \cdot \boldsymbol{h}_0 - \boldsymbol{j} \cdot \boldsymbol{\nabla} \mu \geq 0; \\ \boldsymbol{X}_p^0 := \boldsymbol{P}^t \cdot \boldsymbol{F}_e \cdot \boldsymbol{F}_c - \frac{\partial \psi}{\partial \boldsymbol{F}_p^t}. \end{aligned} \tag{17}$$

For simplicity, we assume that all processes are thermodynamically uncoupled and that inequality (17) splits into four stronger inequalities

$$\left(\frac{\mu}{\bar{V}_B}-\frac{\partial\psi}{\partial x}\right)\dot{x}+\left(\boldsymbol{F}_p{\cdot}\boldsymbol{P}^t{\cdot}\boldsymbol{F}_e-\frac{\partial\,\psi}{\partial\,\boldsymbol{F}_c^t}\right){:}\dot{\boldsymbol{F}}_c\geq 0;$$
$$\boldsymbol{X}_p{:}\dot{\boldsymbol{F}}_p\geq 0;\quad \frac{\boldsymbol{\nabla}\theta}{\theta}{\cdot}\boldsymbol{h}_0\leq 0;\quad \boldsymbol{j}{\cdot}\boldsymbol{\nabla}\mu\leq 0. \tag{18}$$

The linear relationships between the generalized thermodynamic forces and the fluxes for materials isotropic in Ω_0 result in the Fourier's and Fick's laws:

$$\boldsymbol{h}_0=-\lambda\frac{\boldsymbol{\nabla}\theta}{\theta},\quad \lambda>0;\quad \boldsymbol{j}=-bc\boldsymbol{\nabla}\mu=-b\bar{V}_B^{-1}x\boldsymbol{\nabla}\mu,\quad b>0, \tag{19}$$

with λ and b standing for the thermal conductivity and mobility coefficients, respectively. Substituting the Fick's law in the balance Eq. (6), we obtain the diffusion equation

$$\dot{c}\;=\;div\;(bc\boldsymbol{\nabla}\mu)\,,\quad \dot{x}\;=\;div\;(bx\boldsymbol{\nabla}\mu)\,,\quad b=\frac{D_0}{R\theta}exp\left(\frac{\alpha\overline{V}_Bp_0}{R\theta}\right). \tag{20}$$

Here, p_0, D_0, α, and $\overline{V}_B$ are the mean stress, pre-exponential factor, and activation volume of diffusion, respectively.

2.1.2 Chemical potential and compositional deformation gradient tensor

2.1.2.1 Compositional dissipation rate

First, let us transform $\boldsymbol{F}_e{\cdot}\boldsymbol{F}_c=\boldsymbol{F}_e{\cdot}\boldsymbol{R}_c{\cdot}\boldsymbol{U}_c=\bar{\boldsymbol{F}}_e{\cdot}\boldsymbol{U}_c$, where $\boldsymbol{U}_c$ and $\boldsymbol{R}_c$ are symmetric right stretch and proper orthogonal rotation tensors associated with the compositional deformation gradient $\boldsymbol{F}_c$, and $\bar{\boldsymbol{F}}_e=\boldsymbol{F}_e{\cdot}\boldsymbol{R}_c$ is the rotated elastic deformation gradient (the bar will be omitted below without any confusion). Thus, it is sufficient to consider symmetric (i.e., rotation-free) $\boldsymbol{F}_c=\boldsymbol{U}_c=\boldsymbol{U}_c^t$. In this way, rotations are combined with the elastic deformation gradient, and all results (constitutive equations) are independent of the rigid-body rotation in the unloaded configuration Ω_c. Thus,

$$\boldsymbol{F}=\boldsymbol{F}_e{\cdot}\boldsymbol{U}_c{\cdot}\boldsymbol{F}_p;\qquad \boldsymbol{F}^{-1}=\boldsymbol{F}_p^{-1}{\cdot}\boldsymbol{U}_c^{-1}{\cdot}\boldsymbol{F}_e^{-1}. \tag{21}$$

Utilizing the relationship between the true Cauchy stress $\boldsymbol{\sigma}$ and the Piola-Kirchoff stress $\boldsymbol{P}$,

$$\boldsymbol{P}=J\boldsymbol{\sigma}{\cdot}\boldsymbol{F}^{t-1}\quad\rightarrow\quad \boldsymbol{P}^t=J\boldsymbol{F}^{-1}{\cdot}\boldsymbol{\sigma}, \tag{22}$$

where $J = det\boldsymbol{F} = dV/dV_0$ is the volume ratio in the actual and reference configurations, let us transform the compositional power in Eq. $(18)_1$:

$$\boldsymbol{F}_p{\cdot}\boldsymbol{P}^t{\cdot}\boldsymbol{F}_e{:}\dot{\boldsymbol{U}}_c = J\boldsymbol{F}_p{\cdot}\boldsymbol{F}^{-1}{\cdot}\boldsymbol{\sigma}{\cdot}\boldsymbol{F}_e{:}\dot{\boldsymbol{U}}_c = J\boldsymbol{U}_c^{-1}{\cdot}\boldsymbol{F}_e^{-1}{\cdot}\boldsymbol{\sigma}{\cdot}\boldsymbol{F}_e{:}\dot{\boldsymbol{U}}_c = J\boldsymbol{\sigma}{:}\boldsymbol{F}_e{\cdot}\dot{\boldsymbol{U}}_c{\cdot}\boldsymbol{U}_c^{-1}{\cdot}\boldsymbol{F}_e^{-1}$$
$$= J\boldsymbol{\sigma}{:}\boldsymbol{d}_c; \quad \boldsymbol{d}_c := \left(\boldsymbol{F}_e{\cdot}\dot{\boldsymbol{U}}_c{\cdot}\boldsymbol{U}_c^{-1}{\cdot}\boldsymbol{F}_e^{-1}\right)_s, \tag{23}$$

where the symmetry of the Cauchy stress was used, and $\boldsymbol{d}_c$ is the compositional part of the deformation rate $\boldsymbol{d}$; see Eq. (4). Using the component form of the tensors in the Cartesian coordinate system, we express

$$d_c^{ij} = \left(F_e^{ik}\dot{U}_c^{kl}U_c^{lm\,-1}F_e^{mj\,-1}\right)_s = A^{ijkl}\dot{U}_c^{kl}; \quad A^{ijkl} := \left(F_e^{ik}U_c^{lm\,-1}F_e^{mj\,-1}\right)_s, \tag{24}$$

$$\boldsymbol{d}_c = \boldsymbol{A}{:}\dot{\boldsymbol{U}}_c; \qquad \dot{\boldsymbol{U}}_c = \boldsymbol{A}^{-1}{:}\boldsymbol{d}_c, \tag{25}$$

where the fourth-rank tensor $\boldsymbol{A}$ has components A^{ijkl}. Note that the expression for tensor $\boldsymbol{A}$ in component-free form can be found in [37]. Then, the dissipative inequality $(18)_1$ for compositional expansion transforms to

$$\left(\frac{\mu}{\bar{V}_B} - \frac{\partial\psi}{\partial x}\right)\dot{x} + \boldsymbol{X}_c{:}\boldsymbol{d}_c \geq 0; \quad \boldsymbol{X}_c := J\boldsymbol{\sigma} - \frac{\partial\,\psi}{\partial\,\boldsymbol{U}_c}{:}\boldsymbol{A}_c^{-1}. \tag{26}$$

Traditionally, $\boldsymbol{U}_c$ is considered as a spherical tensor describing isotropic volumetric expansion. Although for amorphous isotropic material in a stress-free condition this is the only possibility, stresses can induce anisotropy of A (Li) and B (Si) atom distributions in order to minimize the Gibbs energy of the system and lead to tensorial $\boldsymbol{U}_c$. For crystalline Li_xSi, $\boldsymbol{U}_c$ should be tensorial even under zero stresses since for many values of x crystal lattice is noncubic [38,39]. Below, we will develop a constitutive equation for $\boldsymbol{U}_c$ for amorphous isotropic material and derive a more general expression for the chemical potential.

It is convenient to present $\boldsymbol{U}_c = J_c^{1/3}\boldsymbol{U}_c^S$ [40], where $J_c = det(\boldsymbol{U}_c)$ is the ratio of elemental volumes with concentration of A, x, and zero, and $\boldsymbol{U}_c^S$ is the part of the compositional deformation gradient that describes isochoric change in shape, $det\boldsymbol{U}_c^S = 1$. Then,

$$\dot{\boldsymbol{U}}_c{\cdot}\boldsymbol{U}_c^{-1} = \frac{1}{3}\frac{\dot{J}_c}{J_c}\boldsymbol{I} + \dot{\boldsymbol{U}}_c^S{\cdot}\boldsymbol{U}_c^{S-1}; \quad \boldsymbol{F}_e{\cdot}\dot{\boldsymbol{U}}_c{\cdot}\boldsymbol{U}_c^{-1}{\cdot}\boldsymbol{F}_e^{-1} = \frac{1}{3}\frac{\dot{J}_c}{J_c}\boldsymbol{I} + \boldsymbol{F}_e{\cdot}\dot{\boldsymbol{U}}_c^S{\cdot}\boldsymbol{U}_c^{S-1}{\cdot}\boldsymbol{F}_e^{-1};$$
$$\boldsymbol{d}_c = \frac{1}{3}\frac{\dot{J}_c}{J_c}\boldsymbol{I} + \left(\boldsymbol{F}_e{\cdot}\dot{\boldsymbol{U}}_c^S{\cdot}\boldsymbol{U}_c^{S-1}{\cdot}\boldsymbol{F}_e^{-1}\right)_s; \quad \boldsymbol{I}{:}\boldsymbol{F}_e{\cdot}\dot{\boldsymbol{U}}_c^S{\cdot}\boldsymbol{U}_c^{S-1}{\cdot}\boldsymbol{U}_e^{-1} = \dot{\boldsymbol{U}}_c^S{:}\boldsymbol{U}_c^{S-1} = \frac{\dot{det\boldsymbol{U}_c^S}}{det\boldsymbol{U}_c^S} = 0 \tag{27}$$

Thus, multiplicative decomposition of deformation gradient $\boldsymbol{U}_c$ into the parts characterizing change in volume and shape results in an additive decomposition of the deformation rate into spherical and deviatoric parts that characterize change in volume and shape. Similar to Eq. (25), we express

$$\boldsymbol{d}_c^S = dev\boldsymbol{d}_c = \left(\boldsymbol{F}_e{\cdot}\dot{\boldsymbol{U}}_c^S{\cdot}\boldsymbol{U}_c^{S-1}{\cdot}\boldsymbol{F}_e^{-1}\right)_s = \boldsymbol{A}^S{:}\dot{\boldsymbol{U}}_c^S; \qquad \dot{\boldsymbol{U}}_c^S = \boldsymbol{A}^{S-1}{:}\boldsymbol{d}_c^S, \tag{28}$$

assuming that the inverse tensor $\boldsymbol{A}^{S-1}$ exists since Eq. $(28)_1$ connects the five independent components of the tensors $\boldsymbol{d}_c^S$ and $\dot{\boldsymbol{U}}_c^S$. Because free energy ψ is a function of $\boldsymbol{U}_c$ (i.e., of $\boldsymbol{U}_c^S$ and J_c) and x, and J_c is a function of x, explicit dependence of ψ on J_c can be omitted without loss of generality. Then, decomposing true stress $\boldsymbol{\sigma} = p_0\boldsymbol{I} + \boldsymbol{S}$ into mean stress $p_0 = \frac{1}{3}\boldsymbol{\sigma}{:}\boldsymbol{I}$ and deviatoric Cauchy stress $\boldsymbol{S}$, we transform the compositional power in Eq. (23):

$$J\boldsymbol{\sigma}{:}\boldsymbol{d}_c = J_e p_0 \dot{J}_c + J\boldsymbol{S}{:}\left(\boldsymbol{F}_e{\cdot}\dot{\boldsymbol{U}}_c^S{\cdot}\boldsymbol{U}_c^{S-1}{\cdot}\boldsymbol{F}_e^{-1}\right)_s = J_e p_0 \dot{J}_c + J\boldsymbol{S}{:}\boldsymbol{d}_c^S, \tag{29}$$

where $J_e = det\boldsymbol{F}_e$ is the ratio of elemental volumes in the deformed state and after elastic unloading. Since $J = det\boldsymbol{F} = det\boldsymbol{F}_e det\boldsymbol{F}_c det\boldsymbol{F}_p = J_e J_c$ ($det\boldsymbol{F}_p = 1$ due to plastic incompressibility), $J/J_c = J_e$ in Eq.(29). Substituting Eqs.(28) and (29) in inequality Eq.$(18)_1$ leads to

$$\left(\frac{\mu}{\bar{V}_B} - \frac{\partial\psi}{\partial x} + J_e p_0 \frac{dJ_c}{dx}\right)\dot{x} + J\bar{\boldsymbol{S}}{:}\boldsymbol{d}_c^S \geq 0; \quad J\bar{\boldsymbol{S}} := J\boldsymbol{S} - dev\left(\frac{\partial\psi}{\partial\boldsymbol{U}_c^S}{:}\boldsymbol{A}^{S-1}\right), \tag{30}$$

where $\bar{\boldsymbol{S}}$ is the generalized deviatoric stress. Traditionally (for $\boldsymbol{d}_c^S = 0$), the multiplier of $\dot{x}$ in the dissipation inequality is assumed to be zero, which defines an explicit expression for the chemical potential μ. In our more general case with $\boldsymbol{d}_c^S \neq 0$, we cannot exclude the fact that the structural rearrangements described by $\boldsymbol{d}_c^S$ cause dissipation. Thus, we decompose the compositional power of deviatoric stresses in Eq. (30):

$$\left(\frac{\mu}{\bar{V}_B} - \frac{\partial\psi}{\partial x} + J_e p_0 \frac{dJ_c}{dx}\right)\dot{x} + (1-\zeta)J\bar{\boldsymbol{S}}{:}\boldsymbol{d}_c^S + \zeta J\bar{\boldsymbol{S}}{:}\boldsymbol{d}_c^S \geq 0 \tag{31}$$

into two parts, one of them that is proportional to the parameter $0 \leq \zeta \leq 1$ and produces dissipation and the other that is proportional to $1-\zeta$ and does not:

$$\mathcal{D}_c := \zeta J\bar{\boldsymbol{S}}{:}\boldsymbol{d}_c^S \geq 0; \qquad \left(\frac{\mu}{\bar{V}_B} - \frac{\partial\psi}{\partial x} + J_e p_0 \frac{dJ_c}{dx}\right)\dot{x} + (1-\zeta)J\bar{\boldsymbol{S}}{:}\boldsymbol{d}_c^S = 0. \tag{32}$$

According to inequality $(32)_1$, $\boldsymbol{d}_c^S$ must depend on $\bar{\boldsymbol{S}}$–otherwise, $\boldsymbol{d}_c^S$ and $\bar{\boldsymbol{S}}$ can be chosen in many ways that violate dissipation inequality. Even for $\zeta = 0$, $\boldsymbol{d}_c^S$ should depend on $\bar{\boldsymbol{S}}$, or it is impossible to satisfy equality $(32)_2$ for arbitrary $\bar{\boldsymbol{S}}$ and $\boldsymbol{d}_c^S$. For isotropic amorphous materials, $\boldsymbol{d}_c^S$ is an isotropic function of $\bar{\boldsymbol{S}}$–i.e., tensors $|\boldsymbol{d}_c^S|$ and $\bar{\boldsymbol{S}}$ have the same principal axes. To allow change in $\boldsymbol{U}_c^S$ during insertion-extraction only, we impose $\dot{\boldsymbol{U}}_c^S = 0$ when $\dot{x} = 0$. Thus, in general

$$\begin{aligned} &\boldsymbol{d}_c^S = \boldsymbol{k}(\bar{\boldsymbol{S}}, x)|\boldsymbol{d}_c^S| = \boldsymbol{k}(\bar{\boldsymbol{S}}, x)H(\bar{\boldsymbol{S}}, x, |\dot{x}|)|\dot{x}|; \\ &|\boldsymbol{d}_c^S| := \left(\boldsymbol{d}_c^S{:}\boldsymbol{d}_c^S\right)^{0.5} = H(\bar{\boldsymbol{S}}, x, |\dot{x}|)|\dot{x}|; \quad \boldsymbol{k} := \frac{\boldsymbol{d}_c^S}{|\boldsymbol{d}_c^S|}, \end{aligned} \tag{33}$$

where $|\boldsymbol{d}_c^S|$ and $\boldsymbol{k}$ are the magnitude and directing tensor of the $\boldsymbol{d}_c^S$, $|\boldsymbol{k}| = 1$. If we assume that $\boldsymbol{d}_c^S$ is proportional to $\dot{x}$ rather than to $|\dot{x}|$, it would violate the dissipation inequality $\bar{\boldsymbol{S}}{:}\boldsymbol{d}_c^S \geq 0$. This means that in the first approximation the deformation rate $\boldsymbol{d}_c^S$ is the same for insertion and extraction. In the second approximation, we can assume that H depends on $\dot{x}$ rather than on $|\dot{x}|$, but we will keep $|\dot{x}|$ for simplicity. Substituting Eq. (33) in Eq. (32) and allowing for $|\dot{x}| = \dot{x}sign(\dot{x})$, we obtain

$$\begin{aligned} &\mathcal{D}_c = \zeta J\bar{\boldsymbol{S}}{:}\boldsymbol{k}(\bar{\boldsymbol{S}}, x)H(\bar{\boldsymbol{S}}, x, |\dot{x}|)sign(\dot{x})\dot{x} = X_c\dot{x} \geq 0; \quad X_c := \zeta J\bar{\boldsymbol{S}}{:}\boldsymbol{k}(\bar{\boldsymbol{S}}, x)H(\bar{\boldsymbol{S}}, x, |\dot{x}|)sign(\dot{x}). \\ &\left(\frac{\mu}{\bar{V}_B} - \frac{\partial\psi}{\partial x} + J_e p_0 \frac{dJ_c}{dx} + (1-\zeta)J\bar{\boldsymbol{S}}{:}\boldsymbol{k}(\bar{\boldsymbol{S}}, x)H(\bar{\boldsymbol{S}}, x, |\dot{x}|)sign(\dot{x})\right)\dot{x} = 0. \end{aligned} \tag{34}$$

We also define for the *sign* function $sign(0) = 0$. The term in parenthesis is equal to zero, defining the chemical potential

$$\bar{\mu} = \frac{\mu}{\bar{V}_B} = \frac{\partial\psi}{\partial x} - J_e p_0 \frac{dJ_c}{dx} - (1-\zeta)J\bar{\boldsymbol{S}}{:}\boldsymbol{k}(\bar{\boldsymbol{S}}, x)H(\bar{\boldsymbol{S}}, x, |\dot{x}|)sign(\dot{x}). \tag{35}$$

2.1.2.2 Constitutive equation for the deviatoric compositional deformation rate

It is assumed that functions $\zeta(\bar{\boldsymbol{S}}, x)$ and $H(\bar{\boldsymbol{S}}, x, |\dot{x}|)$ should be determined from experiments or atomistic simulations, and our main task now is to find $\boldsymbol{k}$. Expression $\mathcal{D}_c = \zeta J\bar{\boldsymbol{S}}{:}\boldsymbol{d}_c^S \geq 0$ can make the impression that $\zeta J\boldsymbol{S}$ and $\boldsymbol{d}_c^S$ are generalized thermodynamic forces and fluxes and, for example Ziegler's extremum principles [41] can be applied. However, $\bar{\boldsymbol{S}}$ depends not only on $\boldsymbol{d}_c^S$ but also on $|\dot{x}|$, and actual thermodynamic force and flux are X_c and $\dot{x}$, respectively, with X_c depending not only on $\dot{x}$ but parametrically on $\bar{\boldsymbol{S}}$, $\boldsymbol{k}$, and $|\boldsymbol{d}_c^S|/|\dot{x}|$. Also, in the particular

case in which $\zeta = 0$, $X_c = 0$, the chemical potential μ depends parametrically on $\bar{\boldsymbol{S}}$, $\boldsymbol{k}$, $|\boldsymbol{d}_c^S|$, and $|\dot{x}|$. Thus, Ziegler's principles are not directly applicable.

To find an actual directing tensor $\boldsymbol{k}$ among all possible $\boldsymbol{k}^*$, we applied the *postulate of realizability* formulated in [28, 29] and utilized for the solution of various problems for finding extremum principles (see below). In Appendix, we first derived the equation for $\boldsymbol{k}$ from the consideration of the chemical potential, then from the the compositional dissipation rate, and demonstrated that the two results coincide. We obtained the collinearity of $\boldsymbol{k}$ and $\bar{\boldsymbol{S}}$ for both insertion and extraction:

$$\boldsymbol{k} = \frac{\bar{\boldsymbol{S}}}{|\bar{\boldsymbol{S}}|}. \tag{36}$$

Utilizing Eq. (33), we obtain for the deviatoric part of the compositional strain rate

$$\boldsymbol{d}_c^S = \frac{\bar{\boldsymbol{S}}}{|\bar{\boldsymbol{S}}|} H(\bar{\boldsymbol{S}}, x, |\dot{x}|)|\dot{x}|. \tag{37}$$

Then the compositional dissipation rate in Eq. (34) transforms to

$$\mathcal{D}_c = X_c \dot{x} \geq 0; \quad X_c := \zeta J |\bar{\boldsymbol{S}}| H(\bar{\boldsymbol{S}}, x, |\dot{x}|) sign(\dot{x}). \tag{38}$$

Remarks on the postulate of realizability. The postulate of realizability was applied in [28,29] to derive Ziegler's [41] principles of minimum (or maximum) dissipation rate and the corresponding potential relationship between generalized thermodynamic forces and fluxes for a nonlinear thermodynamic system (both time-dependent and time-independent) as well as their generalization. The postulate of realizability was utilized to describe phase transformations in elastic materials with the threshold-type interface dissipation at the microscale [42,43] and semicoherent interfaces [29,44]. It was also applied to find all unknown parameters (like position, shape, and orientation of a nucleus and parameters at the moving phase interface) for phase transformations in elastoplastic materials at the macroscale [7, 27–30, 45] and corresponding FEM solutions [44, 46, 47], for chemical reactions [32, 48], and for twinning and fracture [7, 27, 46]. These applications are not described by Ziegler's principles, because unknown parameters do not represent thermodynamic fluxes or forces. In these cases, the postulate of realizability resulted in the principle of the maximum of the net thermodynamic driving force (i.e., driving

force minus dissipative threshold), which for time-dependent systems was reformulated into the principle of minimum transformation time. In a kinetically stricter formulation, the principle of the minimum of transformation time was derived for sublimation, chemical decomposition, and melting inside elastoplastic materials [49]. Another class of applications is related to the description of a stable post-bifurcation behavior of elastoplastic materials without and with phase transformations [28, 29, 47], which includes formulation of the global phase transformation criterion. One of the nontrivial applications of this approach is finding equations for plastic spin for anisotropic elastoplastic materials [31].

Note that the postulate of realizability does not represent a new thermodynamics law. It is a rational tool for choosing some relationship among various possibilities, independent of the application field. The problem should be formulated in the following way. Let the relationship between some input matrix a and output matrix b (they can be tensors or tensor functions of any rank or set of scalars functions) satisfy one scalar equation $F(a, b) = 0$, which is not sufficient to determine relationship $b(a)$. Here F can be a function or functional of a and b. Then some a is fixed for which for all possible b^* (determined from specific problem formulation) the inequality $F(a, b^*) < 0$ is valid. This means that none of the actual b corresponds to the chosen a. Then we continuously change a and check for each fixed a when equality $F(a, b) = 0$ is met for some b for the first time, i.e., for all other b^* one has $F(a, b^*) < 0$. Thus, for the chosen input a, the process under consideration can in principle occur with the output b for which $F(a, b) = 0$. Then the postulate of realizability states: *as soon as some process can occur, it will occur at the first chance.* That means that the obtained b does correspond to the given a. Thus, for actual b one has $F(a, b) = 0$, for all other b^* one has $F(a, b^*) < 0$, i.e., actual b is determined from the extremum principle $F(a, b) = 0 > F(a, b^*)$.

While the postulate of realizability is independent of a specific system, its numerous applications to the dissipative systems give an impression that it picked up an essential property of dissipative systems. The statement "as soon as some process can occur, it will occur at the first chance" represents some plausible instability statement, which is inexplicitly assumed when instability is studied. That is why the postulate of realizability results under corresponding consideration in instability criteria [28, 29, 31, 47].

The final result depends on the information $F(a,b) = 0$ that is chosen to describe the system, which is the main hypothesis. Whether a specific choice of $F(a,b) = 0$ is correct or not should be decided by comparison with experiments. Eq. (36) is a result for which we did not prescribe any priory restrictions on the function $\boldsymbol{k}(\bar{\boldsymbol{S}})$. In a more general case, we could assume that a scalar function $M(\bar{\boldsymbol{S}}) := \bar{\boldsymbol{S}}{:}\boldsymbol{k}(\bar{\boldsymbol{S}})$ is known (similar to the dissipation function), and then the postulate of realizability would produce a more general result than Eq. (36).

Physical mechanisms behind anisotropic compositional expansion/contraction. When atoms of the component A are inserted in a nonhydrostatically stressed representative volume of A_xB (in particular, Li atoms are inserted in Li_xSi), the driving force for insertion depends on which position of the amorphous matrix they will reside. Different insertion positions result in different deviatoric compositional strain increments. The larger the product $\bar{\boldsymbol{S}}{:}\boldsymbol{d}_c^S$ is, the larger the driving force for insertion is, and the smaller the activation energy for a jump into the corresponding atomic position is. Also, insertion of A atoms may shift atoms of matrix A_xB, leading to additional $\boldsymbol{d}_c^S$. That is the why positioning of new inserting atoms tends to increase the deviatoric compositional strain increment in the direction of the deviatoric stress. The maximization is constrained, because for each $\bar{\boldsymbol{S}}$ there is a maximum possible magnitude $|\boldsymbol{d}_c^S|$ for the optimal placement of new atoms, which cannot be reached because of the stochastic character of the process and role of the entropy. Similarly, during extraction, A atoms from those positions will be extracted, which maximize $\bar{\boldsymbol{S}}{:}\boldsymbol{d}_c^S$ under similar constraint. In the current phenomenological approach this constraint is expressed through the function $H(\bar{\boldsymbol{S}}, x, \dot{x})$.

Note that the above model considers anisotropic expansion/contraction during change in x only. However, under fixed x deviatoric stresses can cause redistribution of the positions of A (and B) atoms, producing an additional change in shape $\boldsymbol{U}^S$, which is not described by $\boldsymbol{d}_c^S$. This is a completely different process than anisotropic expansion/contraction during change in x. For a crystalline material, a jump of interstitial atoms from one site to another under an action of stresses and its return back after stress release is a well-known mechanism of internal friction. For amorphous materials, such change in shape under an action of stresses at fixed x is one of the mechanisms of viscoplastic deformation which should be included in corresponding flow rule (see Section 4). Note that this mechanism requires higher activation

energy than anisotropic expansion/contraction during a change in x. Indeed, the driving force for insertion/extraction can be large even without deviatoric stresses, due to the gradient of the chemical potential. Then, potential barriers for insertion/extraction in this case will be overcome without deviatoric stresses; deviatoric stresses produce an additional contribution and guide in which position atoms reside or from which position they are extracted. For constant x, deviatoric stresses are the only driving force for redistribution of positions of A and B atoms, and such a redistribution requires breaking of atomic bonds. A separate internal variable should be introduced, and an evolution equation for it should be determined, which will be done elsewhere. We may assume that if the time scale after completing insertion is not too large, then this redistribution can be neglected. In the opposite case of a slow change in stresses at constant x, the time scale of such a rearrangement is much faster than the time scale of change in deviatoric stresses. Then, at each stress increment, a thermodynamic equilibrium state is reached, and we can consider that the internal variable is excluded using energy minimization. Then, $\boldsymbol{U}^S$ is a function of $\boldsymbol{S}$ and can be effectively included in elastic strain, leading to nonlinear elasticity. The nonlinear elasticity rule for large stresses was obtained in [20] for Li_xSi with the help of atomistic simulations. Some irregularities in the stress-strain curve in [20] indicate that atomic rearrangements may occur jump-wise and require kinetic description.

2.1.2.3 Constitutive equation for the chemical potential

Substituting Eq. (36) into expression (35) for μ, one finds

$$\frac{\mu}{\bar{V}_B} = \frac{\partial \psi}{\partial x} - J_e p_0 \frac{dJ_c}{dx} - (1-\zeta) J |\bar{\boldsymbol{S}}| H(\bar{\boldsymbol{S}}, x, |\dot{x}|) sign(\dot{x}). \tag{39}$$

As was discussed earlier, the reason for the appearance of the deviatoric part of the compositional deformation rate is the deviatoric stresses. For $\bar{\boldsymbol{S}} = \boldsymbol{0}$, one should have $\boldsymbol{d}_c^S = \boldsymbol{0}$–i.e., $H(\boldsymbol{0}, x, |\dot{x}|) = 0$. The key consequence of the last term in Eq. (39) is that the appearance of the deviatoric part of the compositional deformation rate always increases the magnitude of the driving force for the A transport for both insertion and extraction–i.e., it decreases $\mu(\mathcal{B})$ for

insertion reaction and increases $\mu(\mathcal{B})$ for the extraction reaction. This is logical because if $\bar{\boldsymbol{S}}$ represents internal stresses that appear due to volumetric change during insertion or extraction and suppresses these processes (reduces $|\mu_r - \mu(\mathcal{B})|$), then Eq. (37) describes the relaxation of internal stresses, which should increase $|\mu_r - \mu(\mathcal{B})|$. If $\bar{\boldsymbol{S}}$ represents prescribed external stresses, then they produce positive compositional work along the $\boldsymbol{d}_c^S$ that also increases $|\mu_r - \mu(\mathcal{B})|$.

This, however, leads to an unusual situation for small driving forces $|\Delta\mu|$, when the driving force is positive simultaneously for both insertion and extraction. Indeed, let us consider an A_xB sample under a hydrostatic condition that is in thermodynamic equilibrium with the reservoir–i.e., $\mu_r = \mu_{\dot{x}=0}$ with $\mu_{\dot{x}=0} := \mu(\mathcal{B}, \bar{\boldsymbol{S}} = 0, \dot{x} = 0)$. Let the shear modulus be independent of x (see below) and the last term in Eq. (39) be the only contribution from the deviatoric stress to the chemical potential. If we apply deviatoric stress $\bar{\boldsymbol{S}}$ to the sample, according to Eq. (39) the chemical potential of A_xB will be reduced for $\dot{x} > 0$ and increased for $\dot{x} < 0$ by the same value $(1-\zeta)J|\bar{\boldsymbol{S}}|H(\bar{\boldsymbol{S}}, x, |\dot{x}|)$–i.e., deviatoric stress produces the same driving force for insertion and extraction. Let us assume that under applied deviatoric stresses an A_xB sample is fluctuationally divided into two samples separated by an interface, and that in one of them insertion occurred and in the other extraction took place (Fig. 2.1). We neglect interface energy and elastic energy due to a jump in $\boldsymbol{U}_c$ across an interface. However, the chemical potential of a sample with $\dot{x} > 0$ is smaller than that for a sample with $\dot{x} < 0$–i.e., $\mu_{\dot{x}>0} < \mu_{\dot{x}<0}$–and the chemical potential of such a heterogeneous sample is larger than the potential $\mu_{\dot{x}>0}$ for the case in which the entire sample undergoes insertion (Fig. 2.1). Thus, it is more probable that the system evolution is governed by the minimization of the chemical potential. Consequently, we postulate (Fig. 2.2) that

$$\begin{aligned} &\dot{x} > 0 \ \text{ and } \ j = b\overline{V}_B^{-1} x(\mu_r - \mu_{\dot{x}>0})/\Delta y \ \text{ if } \ \mu_r > \mu_{\dot{x}>0}; \\ &\dot{x} < 0 \ \text{ and } \ j = b\overline{V}_B^{-1} x(\mu_r - \mu_{\dot{x}<0})/\Delta y \ \text{ if } \ \mu_r \leq \mu_{\dot{x}>0}. \end{aligned} \tag{40}$$

where Δy is the size of the order of magnitude of the size of a Li_xSi sample. Eq. (40) can be interpreted as one more consequence of the postulate of realizability: if the process leading to the minimization of the chemical potential (i.e., insertion) can occur, it will occur. Then, insertion will occur for $\mu_r > \mu_{\dot{x}>0}$, despite the fact that the opposite process (extraction) could

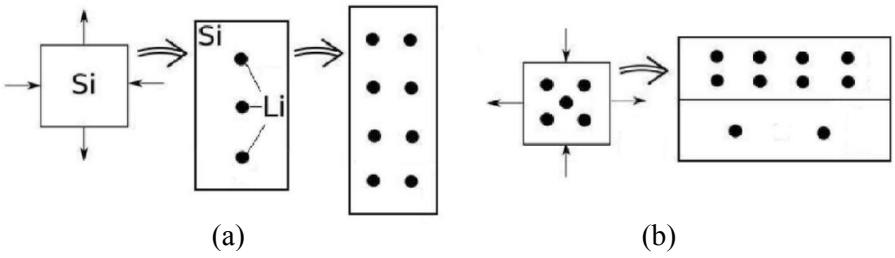

Figure 2.1 (a) Anisotropic compositional deformation of Li_xSi during lithiation under deviatoric stresses. (b) When deviatoric stress $\boldsymbol{S}$, applied to a sample, produces the same driving force for insertion and extraction, the Li_xSi sample may be fluctuationally divided into two samples separated by an interface, in one of which insertion occurs and in the other extraction takes place.

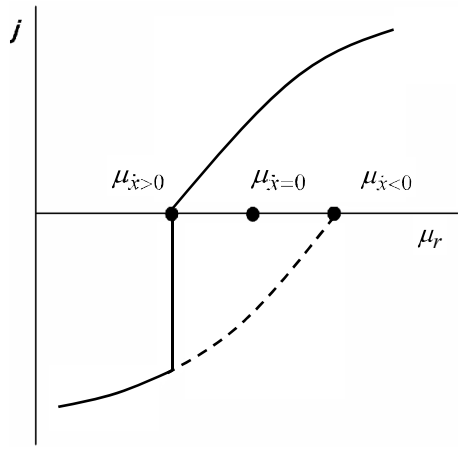

Figure 2.2 Magnitude of the Li flux vs. chemical potential of Li reservoir μ_r under deviatoric stresses (solid line, Eq. (40)).

be faster in the range $\mu_{\dot{x}>0} < \mu_r < \mu_{\dot{x}=0}$ because it leads to a lower chemical potential. It follows from Fig. 2.2 that for $\mu_r = \mu_{\dot{x}>0}$, that when the extraction is possible only, there is a jump in flux because $\mu_r - \mu_{\dot{x}<0}$ is finite. This jump and the corresponding jump in the chemical potential, $\mu_{\dot{x}<0} - \mu_{\dot{x}>0}$, can be used for experimental verification of our theory and for finding the parameter ζ that determines the contribution of the deviatoric stresses to the chemical potential and compositional dissipation rate.

The same conclusion is valid if the elastic moduli depend on x because the corresponding term in the chemical potential is independent of $\dot{x}$ and will promote one of the processes when deviatoric stress is applied. Also, the mobility coefficient may be different for insertion and extraction. Finally, we may consider a more general case with $H(\bar{\boldsymbol{S}}, x, \dot{x})$, depending on the direction of the process. This does not change the conclusion that deviatoric stress promotes insertion and extraction simultaneously but with different magnitudes.

2.1.3 Plastic Flow Rule

Similar to the consideration of compositional changes, let us transform the plastic part of the stress power in Eq. (17):

$$\boldsymbol{P}^t{\cdot}\boldsymbol{F}_e{\cdot}\boldsymbol{U}_c{:}\dot{\boldsymbol{F}}_p = J\boldsymbol{F}^{-1}{\cdot}\boldsymbol{\sigma}{\cdot}\boldsymbol{F}_e{\cdot}\boldsymbol{U}_c{:}\dot{\boldsymbol{F}}_p = J\boldsymbol{\sigma}{\cdot}\boldsymbol{F}_e{\cdot}\boldsymbol{U}_c{:}\dot{\boldsymbol{F}}_p{\cdot}\boldsymbol{F}^{-1} = J\boldsymbol{\sigma}{:}\boldsymbol{l}_p = J\boldsymbol{\sigma}{:}\boldsymbol{d}_p, \qquad (41)$$

where the relationship (22) between the Cauchy stress $\boldsymbol{\sigma}$ and $\boldsymbol{P}$, the definition of $\boldsymbol{l}_p$ (Eqs. (4) and (5)), and the symmetry of the Cauchy stress are taken into account. First, we neglect porosity and assume that the plastic flow is volume-preserving–i.e.,

$$\boldsymbol{I}{:}\boldsymbol{l}_p = \boldsymbol{F}_e{\cdot}\boldsymbol{U}_c{\cdot}\dot{\boldsymbol{F}}_p{:}\boldsymbol{F}_p^{-1}{\cdot}\boldsymbol{U}_c^{-1}{\cdot}\boldsymbol{F}_e^{-1} = \dot{\boldsymbol{F}}_p{:}\boldsymbol{F}_p^{-1} = \frac{\dot{det\boldsymbol{F}_p}}{det\boldsymbol{F}_p} = 0 \quad \text{and} \quad J_p := det\boldsymbol{F}_p = 1. \qquad (42)$$

Since $\boldsymbol{d}_p$ is a deviatoric tensor, $\boldsymbol{\sigma}{:}\boldsymbol{d}_p = \boldsymbol{S}{:}\boldsymbol{d}_p$. To get a unique definition of the plastic deformation gradient, we assume that the extended plastic spin is zero–i.e.

$$(\boldsymbol{l}_p)_a = (\,\boldsymbol{F}_e\cdot\boldsymbol{U}_c\cdot\dot{\boldsymbol{F}}_p\cdot\boldsymbol{F}_p^{-1}\cdot\boldsymbol{U}_c^{-1}\cdot\,\boldsymbol{F}_e^{-1}\,)_a \;=\; \boldsymbol{0}\,. \qquad (43)$$

This eliminates the freedom of an arbitrary rigid-body rotation in the Ω_p and allows us to satisfy in the simplest way the principle of material objectivity. Without compositional strain,

a constitutive equation for the plastic spin for anisotropic materials was derived in [31] with the help of the postulate of realizability. For isotropic material, this equation results in zero plastic spin (see also papers by [50] and [51]). A similar assumption was accepted in various works on large plastic strains without compositional strain [52,53] and for materials with phase transformations and transformation strains [54, 55]. This allows us to determine the rate of plastic deformation gradient $\dot{\boldsymbol{F}}_p$ through the rate of plastic deformation $\boldsymbol{d}_p$:

$$\boldsymbol{F}_e \cdot \boldsymbol{U}_c \cdot \dot{\boldsymbol{F}}_p \cdot \boldsymbol{F}_p^{-1} \cdot \boldsymbol{U}_c^{-1} \cdot \boldsymbol{F}_e^{-1} = \boldsymbol{d}_p \quad \rightarrow \quad \dot{\boldsymbol{F}}_p = \boldsymbol{F}_e^{-1} \cdot \boldsymbol{U}_c^{-1} \cdot \boldsymbol{d}_p \cdot \boldsymbol{F}. \tag{44}$$

Alternatively, we can assume that $\boldsymbol{F}_p$ is a rotation-free symmetric tensor. The plastic dissipation rate per unit undeformed volume in Eq. (17) can be transformed to

$$\mathcal{D}_p = \left(\boldsymbol{P}^t \cdot \boldsymbol{F}_e \cdot \boldsymbol{U}_c - \frac{\partial \psi}{\partial \boldsymbol{F}_p^t} \right) : \dot{\boldsymbol{F}}_p = \left(J\boldsymbol{S} - dev \left(\boldsymbol{F} \cdot \frac{\partial \psi}{\partial \boldsymbol{F}_p^t} \cdot \boldsymbol{F}_e^{-1} \cdot \boldsymbol{F}_c^{-1} \right)_s \right) : \boldsymbol{d}_p = \boldsymbol{S}_p : \boldsymbol{d}_p \geq 0. \tag{45}$$

Then, the yield condition in the $\boldsymbol{S}_p$ space and the viscoplastic flow rule can be accepted as

$$\begin{aligned} f(\boldsymbol{S}_p, \boldsymbol{F}_e, \boldsymbol{U}_c, \boldsymbol{F}_p, x) \leq 0 \quad &\rightarrow \quad \boldsymbol{d}_p = 0; \\ f(\boldsymbol{S}_p, \boldsymbol{F}_e, \boldsymbol{U}_c, \boldsymbol{F}_p, x) > 0 \quad &\rightarrow \quad \boldsymbol{d}_p = \boldsymbol{f}(\boldsymbol{S}_p, \boldsymbol{F}_e, \boldsymbol{U}_c, \boldsymbol{F}_p). \end{aligned} \tag{46}$$

While $\boldsymbol{F}_p$ describes strain hardening/softening and plastic strain-induced anisotropy, $\boldsymbol{U}_c$ characterizes both geometric changes (i.e., change in positions of atoms A and B) and changes in atomic bonding, which may affect viscoplastic properties independent of x. The effect of $\boldsymbol{F}_e$ is similar but significantly smaller, first because of smaller rearrangement in positions of atoms A and B, and second because of the relatively small magnitude of elastic strains in comparison with compositional strains. Even for initially isotropic amorphous materials, for which f and $\boldsymbol{f}$ are isotropic functions of their arguments, anisotropy in the yield condition and flow rule can be caused by $\boldsymbol{F}_e$, $\boldsymbol{U}_c$, and $\boldsymbol{F}_p$. Under rigid-body rotation $d\boldsymbol{r}^* = \boldsymbol{Q} \cdot d\boldsymbol{r}$ in the current configuration, where $\boldsymbol{Q}$ is the arbitrary proper orthogonal tensor, we have

$$\boldsymbol{S}_p^* = \boldsymbol{Q} \cdot \boldsymbol{S}_p \cdot \boldsymbol{Q}^t; \quad \boldsymbol{d}_p^* = \boldsymbol{Q} \cdot \boldsymbol{d}_p \cdot \boldsymbol{Q}^t; \quad \boldsymbol{F}_e^* = \boldsymbol{Q} \cdot \boldsymbol{F}_e, \tag{47}$$

while all other tensors are not altered. Then Eq. (46) transforms to

$$\begin{aligned} f(\boldsymbol{Q} \cdot \boldsymbol{S}_p \cdot \boldsymbol{Q}^t, \boldsymbol{Q} \cdot \boldsymbol{F}_e, \boldsymbol{U}_c, \boldsymbol{F}_p, x) \leq 0 \quad &\rightarrow \quad \boldsymbol{d}_p = 0; \\ f(\boldsymbol{Q} \cdot \boldsymbol{S}_p \cdot \boldsymbol{Q}^t, \boldsymbol{Q} \cdot \boldsymbol{F}_e, \boldsymbol{U}_c, \boldsymbol{F}_p, x) > 0 \quad &\rightarrow \quad \boldsymbol{Q} \cdot \boldsymbol{d}_p \cdot \boldsymbol{Q}^t = \boldsymbol{f}(\boldsymbol{Q} \cdot \boldsymbol{S}_p \cdot \boldsymbol{Q}^t, \boldsymbol{Q} \cdot \boldsymbol{F}_e, \boldsymbol{U}_c, \boldsymbol{F}_p), \end{aligned} \tag{48}$$

which should be valid for an arbitrary $\boldsymbol{Q}$. Choosing $\boldsymbol{Q} = \boldsymbol{R}_e^t$, we obtain the form of the constitutive equations that is independent of the rigid-body rotation:

$$\begin{aligned} f(\boldsymbol{R}_e^t{\cdot}\boldsymbol{S}_p{\cdot}\boldsymbol{R}_e, \boldsymbol{U}_e, \boldsymbol{U}_c, \boldsymbol{F}_p, x) \le 0 \quad &\rightarrow \quad \boldsymbol{d}_p = 0; \\ f(\boldsymbol{R}_e^t{\cdot}\boldsymbol{S}_p{\cdot}\boldsymbol{R}_e, \boldsymbol{U}_e, \boldsymbol{U}_c, \boldsymbol{F}_p, x) > 0 \quad &\rightarrow \quad \boldsymbol{d}_p = \boldsymbol{R}_e{\cdot}\boldsymbol{f}(\boldsymbol{R}_e^t{\cdot}\boldsymbol{S}_p{\cdot}\boldsymbol{R}_e, \boldsymbol{U}_e, \boldsymbol{U}_c, \boldsymbol{F}_p){\cdot}\boldsymbol{R}_e^t. \end{aligned} \tag{49}$$

Similar to the compositional power, the plastic dissipation rate can be decomposed in many ways into a product of dissipative stresses and the deformation rate. Our choice of $\boldsymbol{S}_p$ and $\boldsymbol{d}_p$ has the advantages that it is justified for the anisotropic elasticity rule and is not contradictory for the isotropic elasticity rule.

2.1.4 Specification of the Constitutive Equations

2.1.4.1 Compositional dissipation rate

Let us consider some specifications of Eq. (37). For isotropic (e.g., amorphous) materials, H depends on the second $|\bar{\boldsymbol{S}}|$ and the third $I_3(\bar{\boldsymbol{S}})$ invariants of the deviatoric stress tensor–i.e., $H = H(|\bar{\boldsymbol{S}}|, I_3(\bar{\boldsymbol{S}}), x, |\dot{x}|)$. If we assume, as in traditional models, that the chemical potential in Eq. (35) is a state function–i.e., it is independent of $|\dot{x}|$ (but still can depend on $sign(\dot{x})$)–then the function H is independent of $|\dot{x}|$. Expanding H into a Taylor series in $|\bar{\boldsymbol{S}}|$, we obtain a linear relationship between $\boldsymbol{d}_c^S$ and $|\dot{x}|$:

$$\boldsymbol{d}_c^S = \bar{\boldsymbol{S}}|\dot{x}| \left(a(I_3(\bar{\boldsymbol{S}}), x) + |\bar{\boldsymbol{S}}| a_1(I_3(\bar{\boldsymbol{S}}), x) + ... \right). \tag{50}$$

With regard to the concentration dependence, we believe that $\boldsymbol{d}_c^S$ should be scaled with the magnitude of the rate of volumetric compositional strain, $|\dot{J}_c| = \frac{dJ_c}{dx}|\dot{x}|$. If J_c is a linear function of x, this does not introduce the concentration dependence, but otherwise it does. We assume

$$\boldsymbol{d}_c^S = \bar{\boldsymbol{S}} \frac{dJ_c}{dx} |\dot{x}| \left(\Lambda(I_3(\bar{\boldsymbol{S}}), x) + |\bar{\boldsymbol{S}}| \Lambda_1(I_3(\bar{\boldsymbol{S}}), x) + ... \right). \tag{51}$$

The third invariant, $I_3(\bar{\boldsymbol{S}})$, characterizes the effect of the mode of the stress state (shear, tension, or compression) and in the first approximation can be omitted. When nonlinear dependence

on $|\bar{\boldsymbol{S}}|$ is neglected, ($\Lambda_1 = 0$), Eq. (51) simplifies to

$$\boldsymbol{d}_c^S = \Lambda(x)\bar{\boldsymbol{S}}\frac{dJ_c}{dx}|\dot{x}|; \qquad \Lambda > 0. \tag{52}$$

In the simplest case, Λ can be considered to be a constant. In general, all functions in the equation for $\boldsymbol{d}_c^S$ may also depend on temperature and pressure. In addition, according to DFT simulations [20], function J_c is slightly different for insertion and extraction, so we may use two different functions: J_c^+ for $\dot{x} > 0$ and J_c^- for $\dot{x} < 0$. Similarly, Λ can be different for insertion and extraction, and we may also use Λ^+ for $\dot{x} > 0$ and Λ^- for $\dot{x} < 0$. With Eq. (52), Eq. (39) for the chemical potential transforms to

$$\frac{\mu}{\bar{V}_B} = \frac{\partial\psi}{\partial x} - J_e p_0 \frac{dJ_c}{dx} - \Lambda(1-\zeta)J\bar{\boldsymbol{S}}{:}\bar{\boldsymbol{S}}\frac{dJ_c}{dx}sign(\dot{x}). \tag{53}$$

As the next approximation we can assume that $\bar{\boldsymbol{S}} = \boldsymbol{S}$ in all previous equations.

2.1.4.2 Elasticity rule

In all atomistic simulations, elastic moduli are calculated by considering elastic perturbation, taking unloaded configuration Ω_c as the reference one [38, 39]. This automatically assumes independence of the elasticity rule of $\boldsymbol{F}_p$ and $\boldsymbol{U}_c$–i.e., it should not include any information about the reference configurations Ω_0 and Ω_p. In addition, let us transform elasticity rule Eq. $(16)_1$ to the form consistent with such a definition. Let us introduce a Lagrangian elastic strain $\boldsymbol{E}_e = 0.5(\boldsymbol{F}_e^t{\cdot}\boldsymbol{F}_e - \boldsymbol{I})$. Using relation (22) between the stresses $\boldsymbol{\sigma}$ and $\boldsymbol{P}$ and relation $\dfrac{\partial\psi}{\partial\boldsymbol{F}_e} = \boldsymbol{F}_e{\cdot}\dfrac{\partial\psi}{\partial\boldsymbol{E}_e}$, we transform Eq. $(16)_1$ to the form

$$J\boldsymbol{F}_c{\cdot}\boldsymbol{F}_p{\cdot}\boldsymbol{F}^{-1}{\cdot}\boldsymbol{\sigma} = J\boldsymbol{F}_e^{-1}{\cdot}\boldsymbol{\sigma} = \frac{\partial\psi}{\partial\boldsymbol{E}_e}{\cdot}\boldsymbol{F}_e^t; \qquad \rightarrow \tag{54}$$

$$\boldsymbol{\sigma} = J^{-1}\boldsymbol{F}_e{\cdot}\frac{\partial\psi}{\partial\boldsymbol{E}_e}{\cdot}\boldsymbol{F}_e^t; \qquad \rightarrow \quad \hat{\boldsymbol{\sigma}} := J_e\boldsymbol{F}_e^{-1}{\cdot}\boldsymbol{\sigma}{\cdot}\boldsymbol{F}_e^{t-1} = J_c^{-1}\frac{\partial\psi}{\partial\boldsymbol{E}_e}. \tag{55}$$

Both the left- and right-hand sides of Eq. $(55)_2$ are defined in the unloaded configuration Ω_c and do not contain any information about configurations Ω_0 and Ω_p. If we accept the simplest expression for the free energy per unit volume of the unloaded configuration Ω_c,

$$J_c^{-1}\psi = J_c^{-1}\psi_m(\theta, x) + 0.5\boldsymbol{E}_e{:}\boldsymbol{C}(x){:}\boldsymbol{E}_e, \tag{56}$$

where $\psi_m(\theta, x)$ is the concentrational part of the free energy and $\boldsymbol{C}$ is the fourth-rank tensor of (isotropic) elastic moduli, then Eq. (55) results in

$$\hat{\boldsymbol{\sigma}} = \boldsymbol{C}(x){:}\boldsymbol{E}_e; \qquad \boldsymbol{\sigma} = J_e^{-1}\boldsymbol{F}_e{\cdot}\boldsymbol{C}(x){:}\boldsymbol{E}_e{\cdot}\boldsymbol{F}_e^t. \tag{57}$$

Note that the same expression for the elastic energy was accepted in [5] but in the reference configuration (i.e., $J^{-1}\psi = J^{-1}\psi_m(\theta, x) + 0.5\boldsymbol{E}_e{:}\boldsymbol{C}(x){:}\boldsymbol{E}_e$), which led to the equation $\boldsymbol{\sigma} = J^{-1}\boldsymbol{F}_e{\cdot}\boldsymbol{C}{:}\boldsymbol{E}_e{\cdot}\boldsymbol{F}_e^t$ that explicitly depends on the reference configurations Ω_0. While J_e is approximately equal to 1 for small elastic strain, $J = J_eJ_c$ exceeds 4 because of large compositional volume change. This introduces strong nonphysical dependence of the elasticity rule on compositional volume change and corresponding nonphysical contribution to the chemical potential. Such a contradiction was realized in [5] and was treated in a simplified way by accepting that the Young's modulus grows with x (while it decreases with x in atomistic simulations [39]).

2.1.4.3 Chemical free energy

Energy of the stress-free A_yB_{1-y} or A_xB system per unit reference volume is

$$\psi_m(\theta, x) = \overline{V}_B^{-1}\left(x\mu_0^A(\theta) + \mu_0^B(\theta) + \psi_m^{exe}(x, \theta) + R\theta(x\ln y + \ln(1-y))\right), \quad y = \frac{x}{1+x}, \tag{58}$$

where R is the universal gas constant, y is the molar fraction of A, μ_0^A and μ_0^B are the standard chemical potentials of A and B, ψ_m^{exc} is the molar excess energy per mole of B, and the last term represents mixing entropy per mole of B. The excess energy per mole is defined in [56] as

$$\psi_m^{exe}(x, \theta) = x_{max}\widehat{c}(1-\widehat{c})\left(A_0\widehat{c} + B_0(1-\widehat{c})\right), \quad \widehat{c} = \frac{x}{x_{max}}, \tag{59}$$

where x_{max} is the maximum solubility of Li in Si. Substituting Eqs. (56)-(58) in Eq. (53), we obtain more explicit expression for the chemical potential:

$$\frac{\mu}{\bar{V}_B} = \frac{1}{\bar{V}_B}\left(\mu_0^A(\theta) + R\theta\ln y - 3\left(A_0 - B_0\right)\widehat{c}^{\,2} + 2\left(A_0 - 2B_0\right)\widehat{c} + B_0\right) + \tag{60}$$
$$0.5J_e\boldsymbol{E}_e{:}\frac{d\boldsymbol{C}(x)}{dx}{:}\boldsymbol{E}_e + 0.5\frac{dJ_c}{dx}\boldsymbol{E}_e{:}\boldsymbol{C}(x){:}\boldsymbol{E}_e - J_ep_0\frac{dJ_c}{dx} - \Lambda(1-\zeta)J\bar{\boldsymbol{S}}{:}\bar{\boldsymbol{S}}\frac{dJ_c}{dx}sign(\dot{x}).$$

Note that constitutive equations for plasticity can be found–e.g., in [5, 19], and [6].

2.1.5 Relationships for Alternative Kinematic Decomposition

Let us assume that we have determined experimentally the constitutive equations for two separate cases: (1) when plasticity is absent, and (2) when compositional expansion is absent. Then, we would like to obtain the simplest constitutive equations for simultaneous occurrence of plastic flow and compositional expansion under the assumption that these two processes occur independently of each other. Several definitions of mutual independence of processes can be found in [37]. If we can derive such equations, then the mutual interaction of these processes can be included in the next approximation. However, the main problem is whether one is able to derive the simplest equations. Analyzing all of the above equations obtained for compositional expansion, we do not see any traces of plastic strain. Thus, equations for compositional expansion are independent of plastic strain. At the same time, the definition of the plastic part of the deformation rate $\boldsymbol{d}_p$ (Eq. (5)) and, consequently, the corresponding constitutive Eqs. (49) explicitly contain $\boldsymbol{F}_c$. The reason for such a dependence is the multiplicative decomposition Eq. (1), in which $\boldsymbol{F}_p$ is the last multiplier. If one changes the sequence in Eq. (1) from $\boldsymbol{F}_c{\cdot}\boldsymbol{F}_p$ to $\boldsymbol{F}_p{\cdot}\boldsymbol{F}_c$, then the plastic part of the deformation rate and consequently the flow rule will be independent of $\boldsymbol{F}_c$, but the compositional part of the deformation rate will include $\boldsymbol{F}_p$. Here, we consider an alternative kinematics and the corresponding derivation of the constitutive equations, which do not have such a drawback.

We start with the following multiplicative decomposition of the deformation gradient

$$\boldsymbol{F} = \boldsymbol{F}_e{\cdot}\boldsymbol{U}_i \tag{61}$$

into elastic and inelastic parts, with $\boldsymbol{U}_i = \boldsymbol{U}_i^t$ considered to be rotation-free. Inelastic deformation gradient $\boldsymbol{U}_i$ transforms the reference configuration Ω_0 into the intermediate, stress-free configuration Ω_i, which is used as the reference one for the elasticity rule. Then,

$$\dot{\boldsymbol{F}} = \dot{\boldsymbol{F}}_e{\cdot}\boldsymbol{U}_i + \boldsymbol{F}_e{\cdot}\dot{\boldsymbol{U}}_i; \quad \boldsymbol{F}^{-1} = \boldsymbol{U}_i^{-1}{\cdot}\boldsymbol{F}_e^{-1}, \tag{62}$$

and we derive the additive decomposition of the velocity gradient $\boldsymbol{l}$ and deformation rate $\boldsymbol{d}$

$$\boldsymbol{l} = \dot{\boldsymbol{F}}_e{\cdot}\boldsymbol{F}_e^{-1} + \boldsymbol{F}_e{\cdot}\dot{\boldsymbol{U}}_i{\cdot}\boldsymbol{U}_i^{-1}{\cdot}\boldsymbol{F}_e^{-1} = \boldsymbol{l}_e + \boldsymbol{l}_i, \tag{63}$$

$$\boldsymbol{d} = \left(\dot{\boldsymbol{F}}_e{\cdot}\boldsymbol{F}_e^{-1}\right)_s + \left(\boldsymbol{F}_e{\cdot}\dot{\boldsymbol{U}}_i{\cdot}\boldsymbol{U}_i^{-1}{\cdot}\boldsymbol{F}_e^{-1}\right)_s = \boldsymbol{d}_e + \boldsymbol{d}_i \tag{64}$$

into elastic and inelastic contributions. As the main kinematic hypothesis, we accept an additive decomposition of the inelastic deformation rate into compositional and plastic parts:

$$\boldsymbol{d}_i = \left(\boldsymbol{F}_e{\cdot}\dot{\boldsymbol{U}}_i{\cdot}\boldsymbol{U}_i^{-1}{\cdot}\boldsymbol{F}_e^{-1}\right)_s = \boldsymbol{d}_c + \bar{\boldsymbol{d}}_p; \quad \boldsymbol{d}_c := \left(\boldsymbol{F}_e{\cdot}\dot{\boldsymbol{U}}_c{\cdot}\boldsymbol{U}_c^{-1}{\cdot}\boldsymbol{F}_e^{-1}\right)_s; \quad \bar{\boldsymbol{d}}_p := \left(\boldsymbol{F}_e{\cdot}\dot{\boldsymbol{U}}_p{\cdot}\boldsymbol{U}_p^{-1}{\cdot}\boldsymbol{F}_e^{-1}\right)_s. \tag{65}$$

The important point of Eq. (65) is that compositional and plastic deformation gradients are assumed to be rotation free– i.e., $\boldsymbol{U}_c = \boldsymbol{U}_c^t$ and $\boldsymbol{U}_p = \boldsymbol{U}_p^t$. This allows us to connect each of the contributions to the deformation rate with the corresponding deformation gradients by invertible relations similar to those in Eqs. (24) and (25):

$$\boldsymbol{d}_i = \boldsymbol{A}_i{:}\dot{\boldsymbol{U}}_i, \qquad \dot{\boldsymbol{U}}_i = \boldsymbol{A}_i^{-1}{:}\boldsymbol{d}_i; \quad \boldsymbol{d}_c = \boldsymbol{A}_c{:}\dot{\boldsymbol{U}}_c, \qquad \dot{\boldsymbol{U}}_c = \boldsymbol{A}_c^{-1}{:}\boldsymbol{d}_c; \quad \bar{\boldsymbol{d}}_p = \boldsymbol{A}_p{:}\dot{\boldsymbol{U}}_p, \qquad \dot{\boldsymbol{U}}_p = \boldsymbol{A}_p^{-1}{:}\bar{\boldsymbol{d}}_p \tag{66}$$

with corresponding fourth-rank tensors $\boldsymbol{A}_i$, $\boldsymbol{A}_c$, and $\boldsymbol{A}_p$. The equation for $\boldsymbol{d}_c$ did not change in comparison with Eq. (5), and all of the constitutive equations for compositional strains remain the same. The equation for $\boldsymbol{d}_p$ does not contain $\boldsymbol{F}_c$ now, which will allow us to formulate the flow rule independent of $\boldsymbol{F}_c$.

Our initial point of the thermodynamic treatment will be Eq. (14), in which we omit terms with $\boldsymbol{\nabla}\theta$ and $\boldsymbol{\nabla}\mu$ (assuming that all processes are thermodynamically uncoupled and using inequalities (18)) and express stress power as $\boldsymbol{P}^t{:}\dot{\boldsymbol{F}} = J\boldsymbol{\sigma}{:}\boldsymbol{d}$:

$$\mathcal{D} \;=\; J\boldsymbol{\sigma}{:}\boldsymbol{d} - \dot{\psi} - s\,\dot{\theta} + \bar{V}_B^{-1}\mu\,\dot{x} \geq 0. \tag{67}$$

We assume that $\psi = \psi(\boldsymbol{F}_e, \boldsymbol{U}_c, \boldsymbol{U}_p, \theta, x)$, and substituting ψ, Eq. (65), and Eq. (66) in Eq. (67), we obtain

$$\mathcal{D} = J\boldsymbol{\sigma}{:}\left(\dot{\boldsymbol{F}}_e{\cdot}\boldsymbol{F}_e^{-1}\right)_s - \frac{\partial\psi}{\partial\boldsymbol{E}_e}{:}\dot{\boldsymbol{E}}_e + \left(J\boldsymbol{\sigma} - \frac{\partial\psi}{\partial\boldsymbol{U}_c}{:}\boldsymbol{A}_c^{-1}\right){:}\boldsymbol{d}_c + \left(J\boldsymbol{\sigma} - \frac{\partial\psi}{\partial\boldsymbol{U}_p}{:}\boldsymbol{A}_p^{-1}\right){:}\bar{\boldsymbol{d}}_p$$
$$- \left(s - \frac{\partial\psi}{\partial\theta}\right)\dot{\theta} + \left(\frac{\mu}{\bar{V}_B} - \frac{\partial\psi}{\partial x}\right)\dot{x} \geq 0\,. \tag{68}$$

We can transform $\boldsymbol{\sigma}{:}\dot{\boldsymbol{F}}_e{\cdot}\boldsymbol{F}_e^{-1} = \boldsymbol{F}_e^{-1}{\cdot}\boldsymbol{\sigma}{\cdot}\boldsymbol{F}_e^{-1t}{:}\boldsymbol{F}_e^t{\cdot}\dot{\boldsymbol{F}}_e = \boldsymbol{F}_e^{-1}{\cdot}\boldsymbol{\sigma}{\cdot}\boldsymbol{F}_e^{-1t}{:}\dot{\boldsymbol{E}}_e$. Then, the traditional assumption that the dissipation rate is independent of $\dot{\boldsymbol{E}}_e$ and $\dot{\theta}$ leads to the elasticity rule (55)

and the expression for entropy (16), as well as to the residual dissipation inequality:

$$\mathcal{D} = \left(\frac{\mu}{\bar{V}_B} - \frac{\partial\psi}{\partial x}\right)\dot{x} + \boldsymbol{X}_c{:}\boldsymbol{d}_c + \boldsymbol{X}_p{:}\bar{\boldsymbol{d}}_p \geq 0;$$
$$\boldsymbol{X}_c := J\boldsymbol{\sigma} - \frac{\partial\psi}{\partial\boldsymbol{U}_c}{:}\boldsymbol{A}_c^{-1}; \quad \boldsymbol{X}_p := J\boldsymbol{\sigma} - \frac{\partial\psi}{\partial\boldsymbol{U}_p}{:}\boldsymbol{A}_p^{-1}. \tag{69}$$

We assume that plastic flow and compositional expansion are thermodynamically uncoupled and that inequality (69) splits into two stronger inequalities:

$$\left(\frac{\mu}{\bar{V}_B} - \frac{\partial\psi}{\partial x}\right)\dot{x} + \boldsymbol{X}_c{:}\boldsymbol{d}_c \geq 0; \quad \boldsymbol{X}_p{:}\bar{\boldsymbol{d}}_p \geq 0. \tag{70}$$

Equation $(70)_1$ coincides with Eq. (26), which means that all equations for compositional strain remain the same as for multiplicative decomposition. Since, for plastically incompressible material, $\bar{\boldsymbol{d}}_p$ is a deviator, for the plastic dissipation rate we have

$$\mathcal{D}_p = dev(\boldsymbol{X}_p){:}\bar{\boldsymbol{d}}_p \geq 0; \quad dev(\boldsymbol{X}_p) := J\boldsymbol{S} - dev\left(\frac{\partial\psi}{\partial\boldsymbol{U}_p}{:}\boldsymbol{A}_p^{-1}\right). \tag{71}$$

Then, the yield condition in the $dev(\boldsymbol{X}_p)$ space and the viscoplastic flow rule are

$$f(dev(\boldsymbol{X}_p), \boldsymbol{F}_e, \boldsymbol{U}_c, \boldsymbol{U}_p, x) \leq 0 \quad \rightarrow \quad \bar{\boldsymbol{d}}_p = 0;$$
$$f(dev(\boldsymbol{X}_p), \boldsymbol{F}_e, \boldsymbol{U}_c, \boldsymbol{U}_p, x) \geq 0 \quad \rightarrow \quad \bar{\boldsymbol{d}}_p = \boldsymbol{f}(dev(\boldsymbol{X}_p), \boldsymbol{F}_e, \boldsymbol{U}_c, \boldsymbol{U}_p). \tag{72}$$

Application of the principle of objectivity results in

$$f(\boldsymbol{R}_e^t{\cdot}dev(\boldsymbol{X}_p){\cdot}\boldsymbol{R}_e, \boldsymbol{U}_e, \boldsymbol{U}_c, \boldsymbol{U}_p, x) \leq 0 \quad \rightarrow \quad \bar{\boldsymbol{d}}_p = 0; \tag{73}$$
$$f(\boldsymbol{R}_e^t{\cdot}dev(\boldsymbol{X}_p){\cdot}\boldsymbol{R}_e, \boldsymbol{U}_e, \boldsymbol{U}_c, \boldsymbol{U}_p, x) \geq 0 \quad \rightarrow \quad \bar{\boldsymbol{d}}_p = \boldsymbol{R}_e{\cdot}\boldsymbol{f}(\boldsymbol{R}_e^t{\cdot}dev(\boldsymbol{X}_p){\cdot}\boldsymbol{R}_e, \boldsymbol{U}_e, \boldsymbol{U}_c, \boldsymbol{U}_p) \cdot \boldsymbol{R}_e^t.$$

If $\boldsymbol{U}_c$ is excluded from the arguments in Eq. (73), the flow rule is independent of compositional expansion, since the definition of $\bar{\boldsymbol{d}}_p$ does not include $\boldsymbol{U}_c$. This is an advantage of the additive decomposition Eq. (65) in comparison with multiplicative decomposition.

Note that if $\boldsymbol{U}_c$ and $\boldsymbol{U}_p$ are not arguments of the functions $\boldsymbol{d}_c^S$, f, and $\boldsymbol{f}$, they should not even be introduced, and Eq. (65) simplifies to

$$\boldsymbol{d}_i = \left(\boldsymbol{F}_e{\cdot}\dot{\boldsymbol{U}}_i{\cdot}\boldsymbol{U}_i^{-1}{\cdot}\boldsymbol{F}_e^{-1}\right)_s = \boldsymbol{d}_c + \bar{\boldsymbol{d}}_p. \tag{74}$$

2.1.6 Verification and Application of the Developed Model

In this section, the lithiation-delithiation processes for different structures (thin film, spherical solid, and hollow nanoparticle) are studied by coupled diffusion and mechanical formulation with neglected plasticity.

2.1.6.1 The total system of equations in the undeformed reference configuration

1. Kinematics:

$$\boldsymbol{F} = \boldsymbol{F}_e \cdot \boldsymbol{U}_c; \quad \boldsymbol{E}_e = \frac{1}{2}\left(\boldsymbol{F}_e^t \cdot \boldsymbol{F}_e - \boldsymbol{I}\right); \quad \boldsymbol{U}_c = J_c^{1/3}\boldsymbol{U}_c^S. \tag{75}$$

2. Compositional and elastic parts of the Jacobian:

$$J = J_e J_c; \quad J_e = det(\boldsymbol{F}_e); \quad J_c = 1 + \varepsilon_0 \qquad with \qquad \varepsilon_0 = 3\eta_c x, \tag{76}$$

where η_c and ε_0 are linear coefficients of compositional expansion and volumetric strain.

3. The kinetic equation for the deviatoric compositional deformation rate:

$$\boldsymbol{d}_c^S = dev(\boldsymbol{d}_c) = \left(\boldsymbol{F}_e \cdot \boldsymbol{U}_c^S \cdot \dot{\boldsymbol{U}}_c^{S-1} \cdot \boldsymbol{F}_e^{-1}\right)_s = \Lambda(x)\boldsymbol{S}\frac{dJ_c}{dx}|\dot{x}|; \qquad \Lambda > 0. \tag{77}$$

4. Relationships between stresses:

$$\boldsymbol{\sigma} = J^{-1}\boldsymbol{P} \cdot \boldsymbol{F}^t = p_0\boldsymbol{I} + \boldsymbol{S}. \tag{78}$$

5. The isotropic elasticity rule:

$$\boldsymbol{\sigma} = J_e^{-1}\boldsymbol{F}_e \cdot \boldsymbol{C}(x) : \boldsymbol{E}_e \cdot \boldsymbol{F}_e^t; \qquad \boldsymbol{C} = K\boldsymbol{II} + 2G\boldsymbol{D} = \frac{E}{3(1-2\nu)}\boldsymbol{II} + \frac{E}{(1+\nu)}\boldsymbol{D}, \tag{79}$$

where K, G, and E are the bulk, shear, and Young's moduli; ν is the Poisson's ratio; $\boldsymbol{II} = \{\delta_{ij}\delta_{kl}\}$, $\boldsymbol{D} = \frac{1}{2}\{\delta_{ik}\delta_{jl} + \delta_{il}\delta_{jk} - \frac{2}{3}\delta_{ij}\delta_{kl}\}$ are the volumetric and deviatoric parts of the fourth-rank unit tensor, and δ_{il} are the Kronecker delta.

6. Diffusion flux:

$$\boldsymbol{j} = -\frac{D\overline{V}_{Si}^{-1}x}{R\theta}\boldsymbol{\nabla}\mu, \quad D = D_0(\theta)exp\left(\frac{\alpha\overline{V}_{Si}p_0}{R\theta}\right). \tag{80}$$

7. Chemical potential:

$$\frac{\mu}{\bar{V}_B} = \frac{1}{\bar{V}_B}\left(\mu_0^A(\theta) + R\theta \ln y - 3\left(A_0 - B_0\right)\widehat{c}^2 + 2\left(A_0 - 2B_0\right)\widehat{c} + B_0\right) + \tag{81}$$

$$0.5 J_c \boldsymbol{E}_e{:}\frac{d\boldsymbol{C}(x)}{dx}{:}\boldsymbol{E}_e + 0.5\frac{dJ_c}{dx}\boldsymbol{E}_e{:}\boldsymbol{C}(x){:}\boldsymbol{E}_e - J_e p_0 \frac{dJ_c}{dx} - \Lambda(1-\zeta) J \boldsymbol{S}{:}\boldsymbol{S}\frac{dJ_c}{dx} sign(\dot{x});$$

$$\widehat{c} = \frac{x}{x_{max}}; \quad y = \frac{x}{1+x}. \tag{82}$$

8. Diffusion equation:

$$\dot{x} \;=\; div\left(\frac{D}{R\theta} x \boldsymbol{\nabla}\mu\right). \tag{83}$$

9. Equilibrium equation:

$$\boldsymbol{\nabla}\cdot\boldsymbol{P} = 0. \tag{84}$$

The boundary conditions for the diffusion equation are accepted in the linearized form of the Butler-Volmer equation [57]:

$$\begin{aligned} Lithiation \quad &: \quad \boldsymbol{n}_0{\cdot}\boldsymbol{j} = j_0(1 - x/x_{max}) J \boldsymbol{n}_0{\cdot}\boldsymbol{F}^{-1t}{\cdot}\boldsymbol{n}_0 \\ Delithiation \quad &: \quad \boldsymbol{n}_0{\cdot}\boldsymbol{j} = -j_0(x/x_{max}) J \boldsymbol{n}_0{\cdot}\boldsymbol{F}^{-1t}{\cdot}\boldsymbol{n}_0, \end{aligned} \tag{85}$$

where j_0 represents the charging rate per unit actual (deformed) area. The charging rate is the required time for charging the battery from an empty state to a fully charged state, and it is designated by C/n, where n has the time unit. For example, a charger rated $C/8$ would charge the battery to full capacity in 8 hrs. We used two charging rates, $C/8$ for thin film and $C/0.55$ for solid and hollow nanoparticles, which correspond to $j_0 = 1.4\times10^{-5}$ and 1.03×10^{-5} mol/m^{2}s, respectively. The tensor $J\boldsymbol{F}^{-1t}$ transforms flux from the actual to the reference configuration.

All constants are collected in Table. 2.1. Finite-element code COMSOL Multiphysics (v. 3.5, COMSOL, Inc.) has been utilized to solve the above system of equations. The solution was performed in the reference configuration, then components of true Cauchy stress tensor were calculated. The results are presented in the reference geometry.

In all of the problems below, rotations and shear stresses are absent; the solution can be found in terms of principal stresses and total, elastic, and compositional strains, and all principal axes coincide. Decomposition of the deformation rate in Eq. (5) reduces to

$$\boldsymbol{d} = \dot{\boldsymbol{U}}{\cdot}\boldsymbol{U}^{-1} = \dot{\boldsymbol{U}}_e{\cdot}\boldsymbol{U}_e^{-1} + \dot{\boldsymbol{U}}_c{\cdot}\boldsymbol{U}_c^{-1} = \boldsymbol{d}_e + \boldsymbol{d}_c; \quad \boldsymbol{d} = \ln\dot{\boldsymbol{U}}; \quad \boldsymbol{d}_e = \ln\dot{\boldsymbol{U}}_e; \quad \boldsymbol{d}_c = \ln\dot{\boldsymbol{U}}_c \tag{86}$$

because tensors $\boldsymbol{F}_e$ and $\boldsymbol{F}_e^{-1}$ eliminate each other. Equation (86) results in additive decomposition of the logarithmic strains:

$$\boldsymbol{\varepsilon}^L = \ln \boldsymbol{U} = \ln \boldsymbol{U}_e + \ln \boldsymbol{U}_c = \boldsymbol{\varepsilon}_e^L + \boldsymbol{\varepsilon}_c^L. \tag{87}$$

Table 2.1 Material properties

T	300 K	
x_{max}	3	
D_0	1×10^{-6} m^2/s	[23]
A_0	-29.55 $\times10^3$ J/mol	[56]
B_0	-38.6 $\times10^3$ J/mol	[56]
$\overline{V}_{Si}$	1.2052 $\times10^{-5}$ m^3/mol	[6]
α	0.27	[56]
η_c	0.2356	[6]
E_0	90.13 GPa	[58]
ν	0.28	[6]
η_E	-0.5576	[58]
Λ	0.47 GPa^{-1}	

2.1.6.2 Thin film at rigid substrate: Homogeneous state

To verify our model against experiments and DFT simulations, the problem on the biaxial stress generation and relaxation in the Si film-like anode during lithiation-delithiation on the rigid substrate is modeled using a formulation similar to that in [5] and [20]. The schematic of the problem and the boundary conditions are shown in Fig. 2.3. Diffusion is considered to be fast enough so that x and consequently all fields are homogeneous. Thus, diffusion and equilibrium Eqs. (83) and (84) are omitted. The concentration of Li, x, increases for lithiation and decreases for delithiation as the loading parameter.

The boundary conditions result in the following constraint conditions: $F_1 = F_2 = 1$ for in-plane principal components of the deformation gradient (due to attachment to a rigid substrate) and stress-free condition $\sigma_3 = 0$ for out-of-plane principal stress.

Three different functions are considered for variation of elastic moduli with composition x (constant, linear, and exponential) to study the sensitivity of the simulation to the elastic moduli. The exponential function $E/(1-\nu) = 127.1exp(-0.5576x)$ was fitted to describe

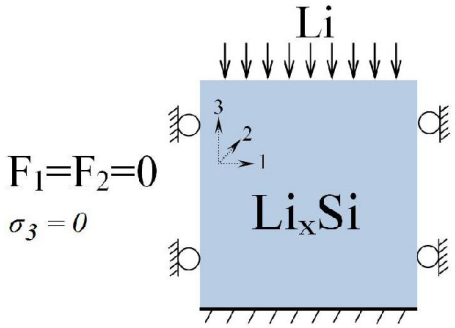

Figure 2.3 Schematics of thin film and boundary conditions. The film is constrained at the lateral sides. The Li concentration is homogeneous throughout the film.

experimental data and atomistic simulations in [59] and [39]. The linear function was taken from [6], $E = E_0(1+\eta_E x)$, with E_0 and η_E for the Young's modulus of $a-Si$ and the variation rate of Young's modulus with concentration (Table 2.1). The results show that the biaxial stress during lithiation is less sensitive to the variation in Young's modulus than the stress for the delithiation process.

Constant $\Lambda = 0.47$ GPa^{-1} (Table 2.1) in the kinetic equation for the deviatoric part of the compositional deformation rate is found from the best fit of biaxial stress $\sigma = \sigma_1 = \sigma_2$ at $x = 2$ to experiment and atomistic simulations in [20]. Our results for evolution of $\sigma(x)$ in Fig. 2.4 demonstrate very good qualitative and quantitative agreements with both DFT calculations and experiments from [20] for both lithiation and delithiation. If it is necessary, comparison could be made even better by including the nonlinear relationship $J_c(x)$ as in [36] and by considering $\Lambda = \Lambda(x)$ and fitting to experiment and/or DFT simulations, as well as by using different $\Lambda(x)$ for insertion and extraction. However, the most important result is that comparison with experiment and DFT simulations is good enough with just a single fitted parameter Λ, which provides proof of conceptual correctness of the idea of anisotropic compositional strain instead of plasticity. In contrast, for the viscoplastic relaxation model [5], two material parameters and the yield strength as a function of x are fitted to experiments; however, agreement with experiment for $\sigma(x)$ is not as good as here. The obtained Λ is used below for all other problems. Since in our model there is no threshold for the stress relaxation

and it occurs both for lithiation-delithiation, a simple suggestion for reducing stresses would be an oscillatory change in x with a small magnitude–e.g., $x = a + acos(\tilde{t})$; here $\tilde{t} = t/100$ s is the dimensionless time and 100 s is a typical diffusion time for lithium through a 100-nm silicon film [20]. In Fig. 2.5a, oscillations started after complete discharge in order to release stresses. Such a significant reduction in stresses is in qualitative agreement with experiments [33]. In contrast, simulation of cyclic lithiation-delithiation in [5] results in almost constant stresses. In Fig. 2.5b, the goal is to keep tensile stresses below 0.8 GPa during delithiation by superposition of multiple oscillatory change in x, $x = x_0 + 0.01cos(\tilde{t})$. Therefore, we can control the stress level to enhance the battery life.

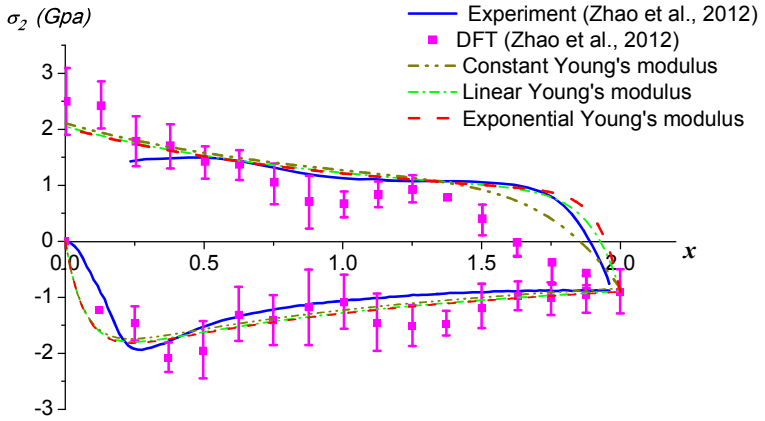

Figure 2.4 Simulated biaxial stress $\sigma(x)$ during lithiation-delithiation of a thin-film on a rigid substrate based on the current theory in comparison with experimental results and atomistic simulations from [20]. Very good correspondence is observed with just single-material parameter Λ fitted to reproduce experiment and DFT simulations at $x = 2$.

Remark. Note that the constitutive equations are written for thermodynamic variables averaged over some representative volume and characteristic time. That is why thermal fluctuations are excluded from them. Thus, one cannot say that thermal fluctuations, which are always present, may lead to oscillation in concentration and stress relaxation with time without any external action. However, in experiments, there are always fluctuations in the boundary conditions which may lead to a spontaneous oscillation of concentration and almost complete stress relaxation. In experiments [33], there are stress oscillations superposed on the reducing

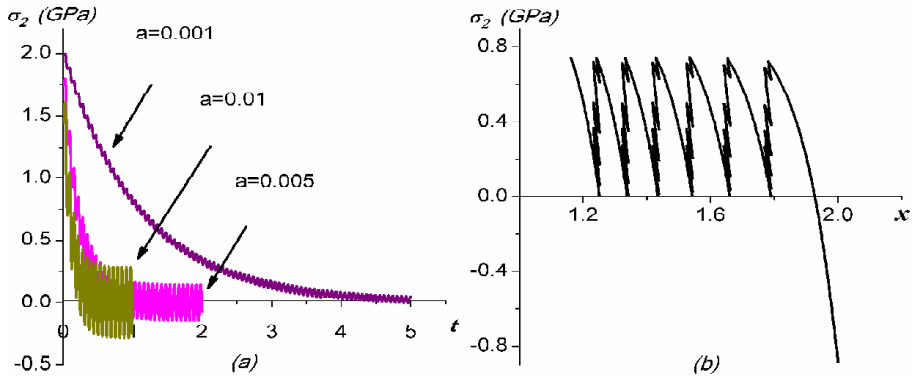

Figure 2.5 (a) Reduction in biaxial stress with time after near completion of delithiation ($x = a$ in Fig. 2.4) under oscillatory change in x. (b) Keeping tensile stresses below 0.8 GPa during delithiation by superposition of multiple oscillatory change in x, $x = x_0 + 0.01cos(\tilde{t})$ when stress reaches 0.8 GPa until it reduces to zero.

in time stress value during a pause between lithiation/delithiation cycles, i.e., at presumably constant x. One of the possible interpretations is that this is due to spontaneous oscillation of concentration. Rate of stress relaxation reduces with a reduction in stress level, similar to our predictions. However, there are no data to confirm that stress may reduce to zero rather than to some finite value. If the latter would be the case, our model can be simply modified to take this into account. Let us assume that the free energy ψ has a simplest additional term $\psi_s = 0.5aJ\boldsymbol{U}_c^S{:}\boldsymbol{U}_c^S$. Then for coinciding principle axes of all tensors, according to Eq. (30) $\bar{\boldsymbol{S}} = \boldsymbol{S} - dev\left(\frac{\partial \psi}{\partial \boldsymbol{U}_c^S} \cdot \boldsymbol{U}_c^S\right) = \boldsymbol{S} - a\, dev\left(\boldsymbol{U}_c^S \cdot \boldsymbol{U}_c^S\right)$. In this case, oscillation of concentration according to Eq. (52) will relax stresses until $\bar{\boldsymbol{S}} = 0$, i.e., $\boldsymbol{S} = a\, dev\left(\boldsymbol{U}_c^S \cdot \boldsymbol{U}_c^S\right)$. Thus, the obtained result encourages the experimental determination of the minimal stress which can be obtained due to a multiple oscillatory change in x, which will lead to a more precise model.

2.1.6.3 Thin film at rigid substrate: Coupling to diffusion

To elucidate the effect of diffusion and heterogeneities, the entire system of Eqs. (75)-(84) is considered for the same geometry and problem formulation as in Section 7.1. The initial width of Si film is $h_0 = 250\ nm$, and diffusion and heterogeneities of x and all parameters are

allowed along axis 3 only. The boundary conditions for diffusion Eq. (86) reduce to

$$\begin{aligned} Lithiation: \quad & j(h_0,t) = j_0(1 - x/x_{max}); \\ Delithiation: \quad & j(h_0,t) = -j_0(x/x_{max}) \end{aligned} \tag{88}$$

because the area does not change, and $J\boldsymbol{n}_0 \cdot \boldsymbol{F}^{-1t} \cdot \boldsymbol{n}_0 = 1$. The boundary condition for principal stress is $\sigma_3(h_0,t) = 0$. The schematic of thin film and boundary conditions are shown in

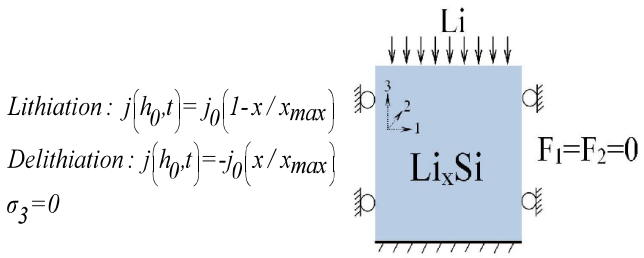

Figure 2.6 Schematics of thin film and boundary conditions. The Li concentration is obtained by solving the diffusion equation.

Fig. 2.6. The variation of average lateral stress σ vs. averaged Li concentration is presented and compared with the homogeneous solution in Fig. 2.7. The slight difference in lateral stress for the initial stage of lithiation between the homogeneous and heterogeneous solutions is related to the heterogenous distribution of Li concentration at the beginning of diffusion. The time evolution of distribution of Li concentration x and lateral stress σ are shown in Fig. 2.8. At the initial stage (100 s), the large concentration gradient at the surface causes large and very heterogeneous compressive stresses. For $t = 1000$ s, while concentration is still heterogeneous, stresses are becoming more homogeneous due to increased compositional strain and deviatoric stress relaxation–i.e., they slightly reduce near the surface and significantly increase away from the surface. During further time evolution, concentration and stresses become more homogeneous. For delithiation, heterogeneity in concentration and stresses are barely visible. Around $t = 400$ s, stress changes sign from compressive to tensile and then grows. The concentration asymmetry between lithiation and delithiation (concentration at the initial time steps for delithiation is more homogeneous than for lithiation) is associated with a sub-regular solution [56]. Figure 2.9 exhibits the concentration field for ideal and sub-regular

solution models for lithiation-delithiation.

To study the effect of the parameter ζ–which is partitioning the part of the compositional stress power that dissipates and the part that contributes to the chemical potential–on the concentration distribution, we increase the charging rate and initial thickness to $C/0.55$ and 500 nm, respectively. Figure 2.10 shows that decreasing ζ from 1 (no effect of deviatoric stress on μ) to 0 (maximum effect) increases the concentration of Li away from the external surface for the intermediate stages of lithiation, and concentration becomes more homogeneous. For $t = 500$ s, the concentration of Li at $y = 0$ doubles when ζ drops from 1 to 0. Thus, the new term in the expression for the chemical potential exhibits an essential contribution to the diffusion process for high deviatoric stress and compositional strain.

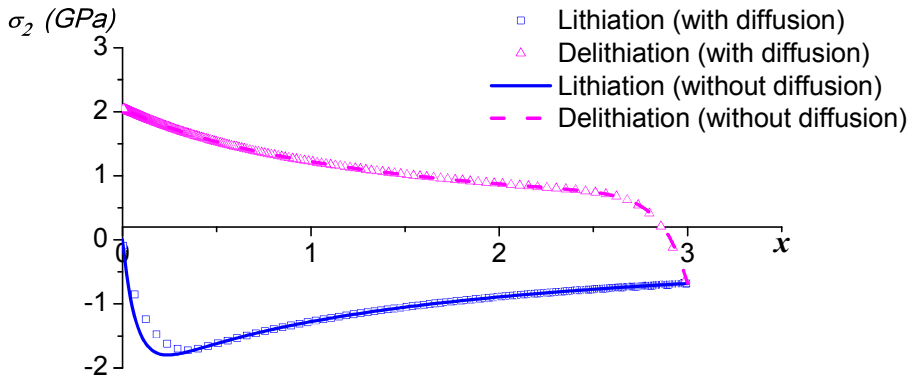

Figure 2.7 Variation of average lateral stress σ vs. averaged Li concentration during lithiation and delithiation of a thin film on a rigid substrate for heterogeneous problem involving diffusion.

2.1.6.4 Solid spherical nanoparticle

One of the most common shapes of nanoanodes is a spherical nanoparticle. Stress generation under a small-deformation assumption, with spherical compositional strain and without plasticity for solid and hollow spherical nanoparticles, can be found in [60] and [61]. The important difference in comparison with the thin film on a rigid substrate is that for homogeneous Li concentration in a spherical particle internal stresses are zero. Here, we apply our model with anisotropic transformation strain. An amorphous spherical particle with initial radius of

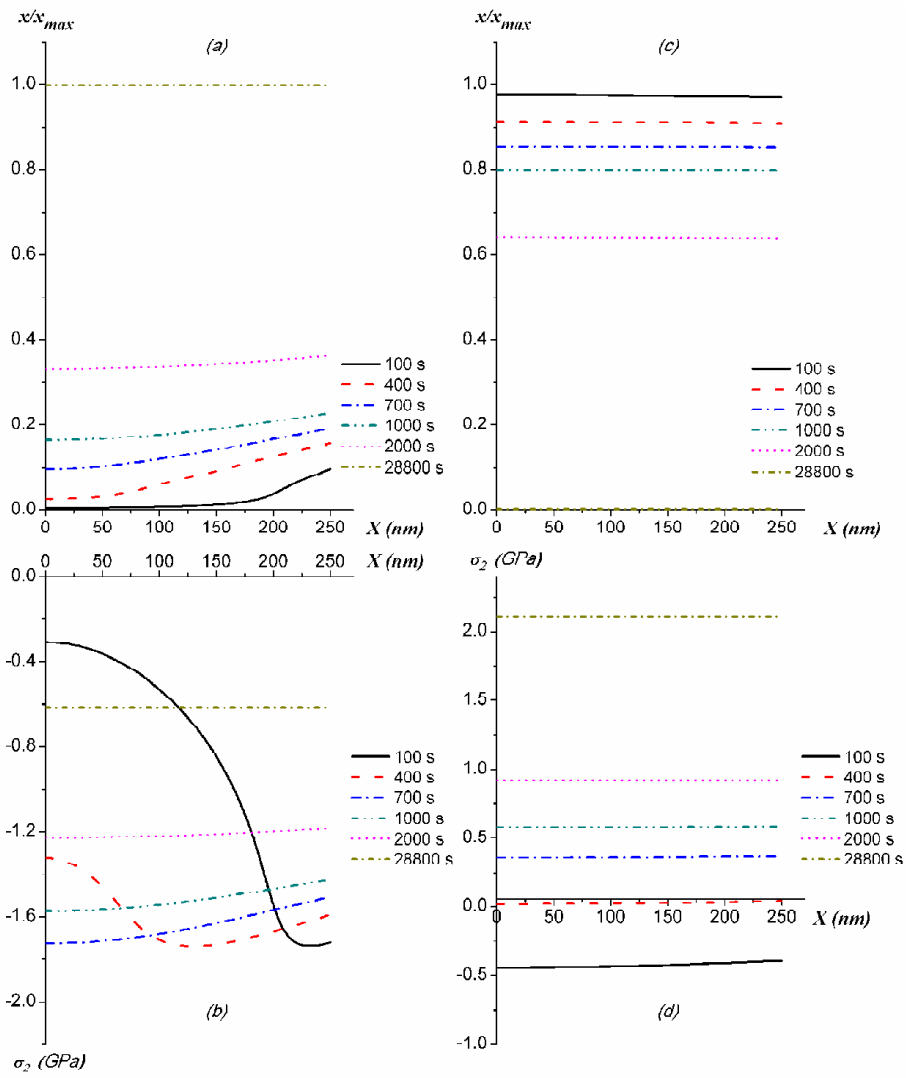

Figure 2.8 Time evolution of distribution of Li concentration x (a and c) and lateral stress σ (b and d) for lithiation (a and b) and delithiation (c and d) of a thin film on a rigid substrate.

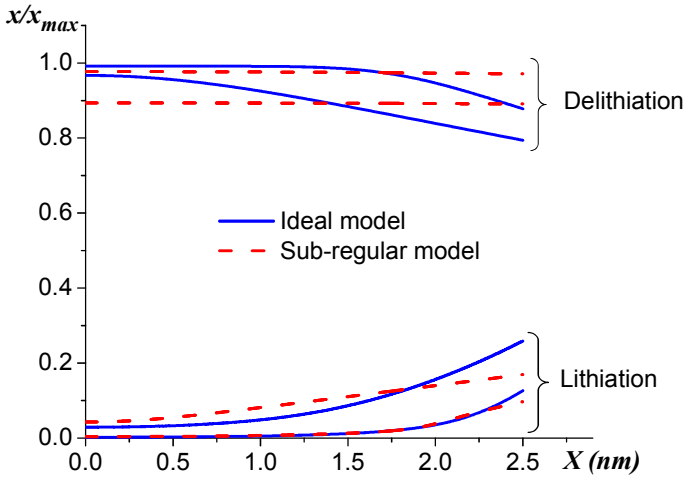

Figure 2.9 Comparison of time evolution of Li concentration x for initial time steps with and without excess energy for lithiation/delithiation of a thin film on a rigid substrate.

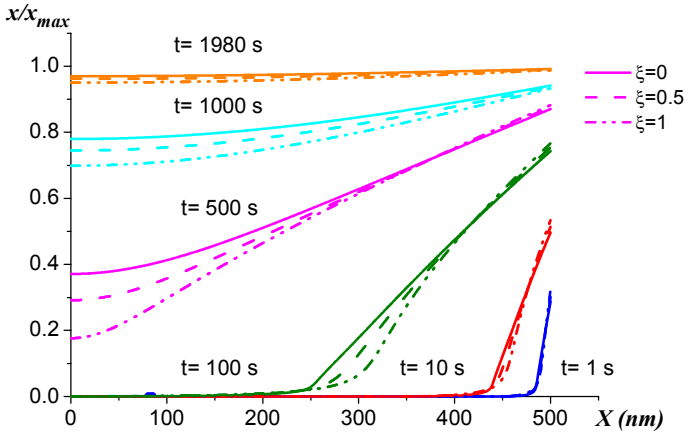

Figure 2.10 Effect of the parameter ζ, which is partitioning the part of the compositional stress power that dissipates and the part that contributes to the chemical potential on the Li concentration distribution in a thin film on a rigid substrate for the charging rate $C/0.55$ and $h_0 = 500$ nm.

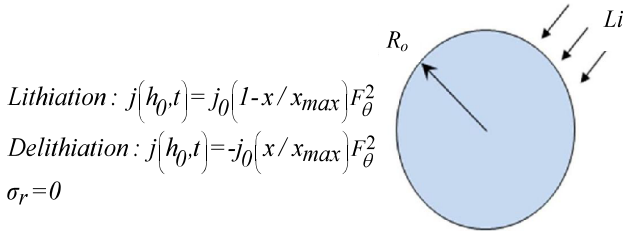

Figure 2.11 Schematics of solid nanoparticle and boundary conditions. The surface is traction free.

$R_0 = 200$ nm is considered here using a spherically symmetric formulation. The outer surface is traction free: $\sigma_r(R_0, t) = 0$. Boundary conditions are depicted in Fig. 2.11. The deformation gradient is

$$\boldsymbol{F} =< F_r, F_\theta, F_\phi >=< 1 + \frac{\partial u}{\partial r}, 1 + \frac{u}{r}, 1 + \frac{u}{r} >, \tag{89}$$

where u is the radial displacement and r is the radius of a particle in the reference configuration. The boundary conditions for diffusion Eq. (86) reduce to

$$\begin{aligned} Lithiation &: \quad j(h_0, t) = j_0(1 - x/x_{max})F_\theta^2 \\ Delithiation &: \quad j(h_0, t) = -j_0(x/x_{max})F_\theta^2, \end{aligned} \tag{90}$$

where $J\boldsymbol{n}_0 \cdot \boldsymbol{F}^{-1t} \cdot \boldsymbol{n}_0 = F_\theta^2$ is the ratio of the deformed to undeformed areas. The charging rate is $C/0.55$. The stress and concentration evolution are shown in Fig. 2.12. Generally, heterogeneity of concentration is relatively low and magnitude of stresses in comparison with the film on a rigid substrate is an order of the magnitude lower for lithiation and two orders of magnitude lower for delithiation. Radial stress is initially tensile for lithiation and compressive for delithiation, and the magnitude first grows then reduces with time and becomes compressive, ending with a small compressive residual stress ~ -3 MPa for homogeneous concentration. Hoop stress is compressive near the surface and tensile in the central region at the beginning of lithiation, and it has the opposite sign for delithiation. The variation of hoop stress with time is similar to that with radial stress (compressive stress first increases then becomes tensile and tends to zero). This is also visible from the evolution of the hoop stress during lithiation and delithiation at the center and surface of a nanoparticle (Fig. 2.13), where the maximum of the magnitude

is reached at the very beginning of each process. Similar behavior was observed with regard to plasticity by [6]. The positive hoop stress at the external surface increases the probability of crack appearance at the outer surface of NPs, which was observed in experiments by [14]. However, the traditional isotropic compositional strain excluding plasticity cannot predict the crack growth from the external surface [61]. This small tensile hoop stress suggests that the critical radius of the amorphous solid NP is large, which is in agreement with experimental studies [25].

2.1.6.5 Hollow nanoparticle

Similar problems are solved for hollow spherical nanoparticles with different initial external and internal radii–$R_o = 208$, 252, 327 nm, $R_i = 100$, 200, 300 nm–with the same volume as a 200 nm solid nanoparticle. In addition to the boundary conditions for the outer surface, the internal surface is traction-free and has zero diffusion flux (Fig. 2.14). The evolutions of Li concentration and stresses are shown in Fig. 2.15 for a $C/0.55$ charging rate. The evolution of the hoop stress during lithiation and delithiation at the inner and outer surfaces of a nanoparticle is demonstrated in Fig. 2.16. In comparison with a solid nanoparticle, radial stress is reduced, and its maximum is shifted to the interior of the particle. Hoop stress is initially tensile at the inner surface and compressive at the outer surface, but it becomes gradually tensile at the external surface and then goes to zero during lithiation. Figure 2.16 shows the variation of hoop stress at the outer surface for different hollow NPs with and without relaxation. Generally speaking, the stress level in hollow NPs is smaller than for NPs with the same volume, and it decreases by increasing the internal radius because the thickness of hollow NPs is reduced, and the Li concentration becomes more homogeneous. Additionally, the relaxation does not affect the stress level of large hollow NPs due to the small induced stresses.

2.2 Concluding remarks

This paper presents, several conceptual developments in the thermodynamics and kinetics of compositional expansion/contraction, the corresponding stress generation and relaxation, and

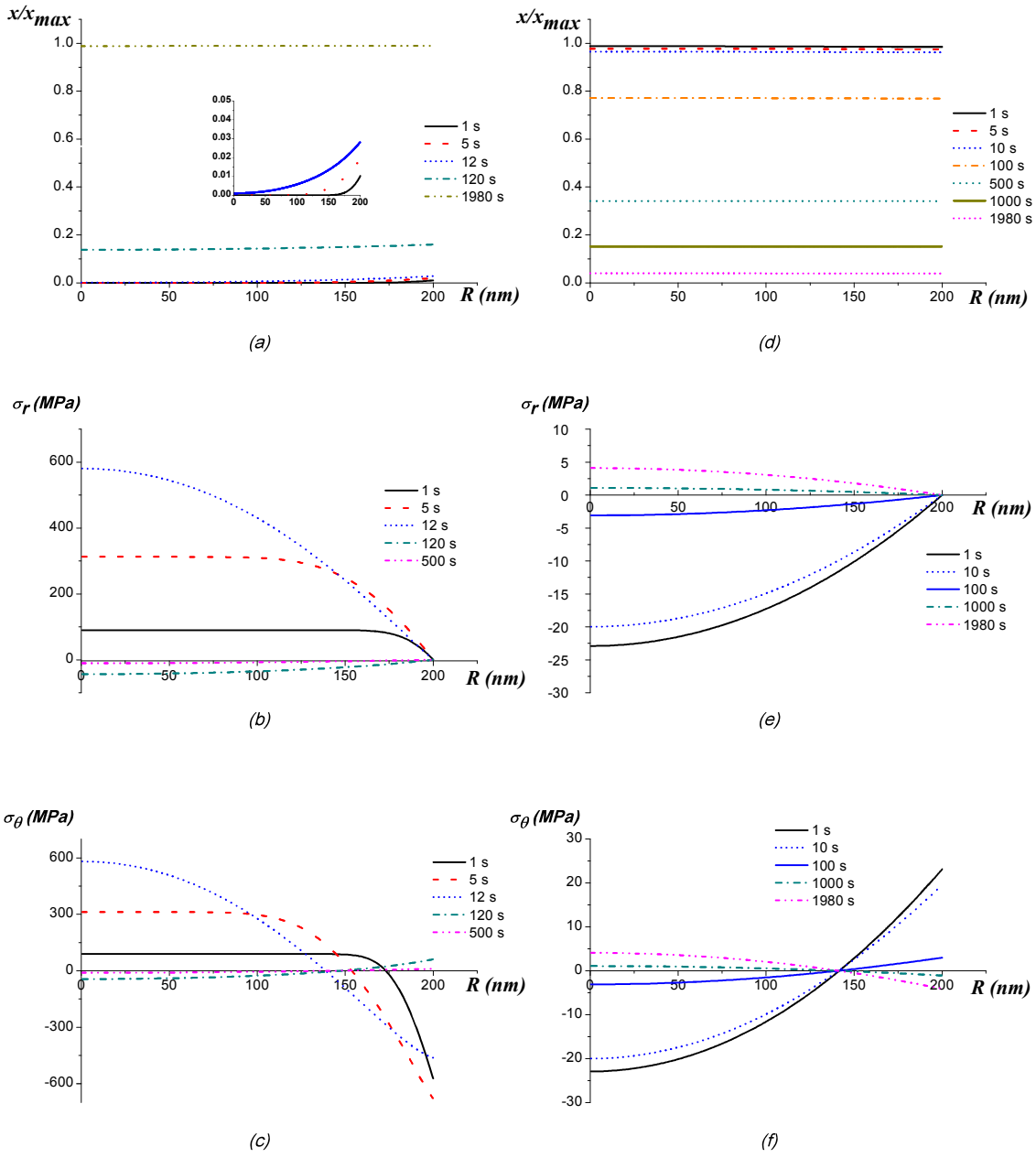

Figure 2.12 Concentration (a and d), radial (b and e), and hoop (c and f) stress evolution for lithiation (a-c) and delithiation (d-f) of a solid spherical nanoparticle.

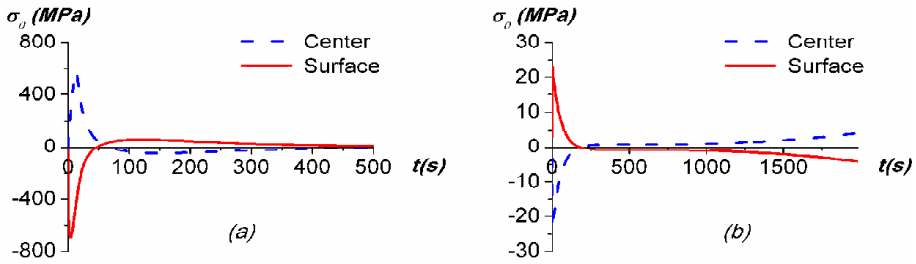

Figure 2.13 Hoop stress for the surface and the center of a solid nanoparticle during lithiation (a) and delithiation (b).

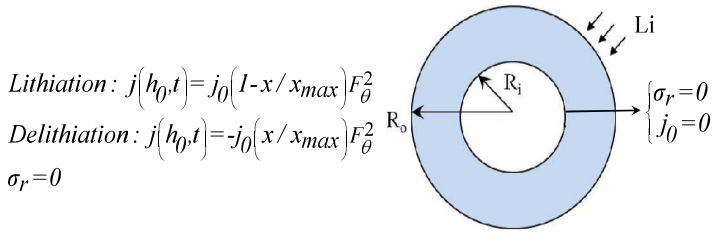

Figure 2.14 Schematic of a hollow nanoparticle and its boundary conditions. All surfaces are traction free.

the stress-induced diffusion and corresponding chemical potential. The developed theory is fully geometrically nonlinear, and it is applied to an important problem of lithiation/delithiation of a nanoscale amorphous Si anode in an Li-ion battery. The main idea is that, despite the material isotropy of amorphous material, deviatoric stresses cause anisotropic (tensorial) compositional expansion/contraction during exertion/extraction of the guest atoms. This leads to an additional contribution of the power of the deviatoric stresses and the deviatoric part of the compositional deformation rate to the dissipative inequality. Usually, the dissipation rate is considered to be independent of the rate of concentration change, which leads to the definition of the chemical potential. Since with the presence of the power of the deviatoric compositional deformation rate this is not necessarily the case, the dissipation rate due to compositional expansion/contraction is introduced as a portion of the power of the deviatoric compositional deformation rate. In this case, the remaining portion of the deviatoric compositional deformation rate is dissipation-free and produces a contribution to the definition of the chemical potential. Adapting and applying a previously formulated postulate of realizability, a simple

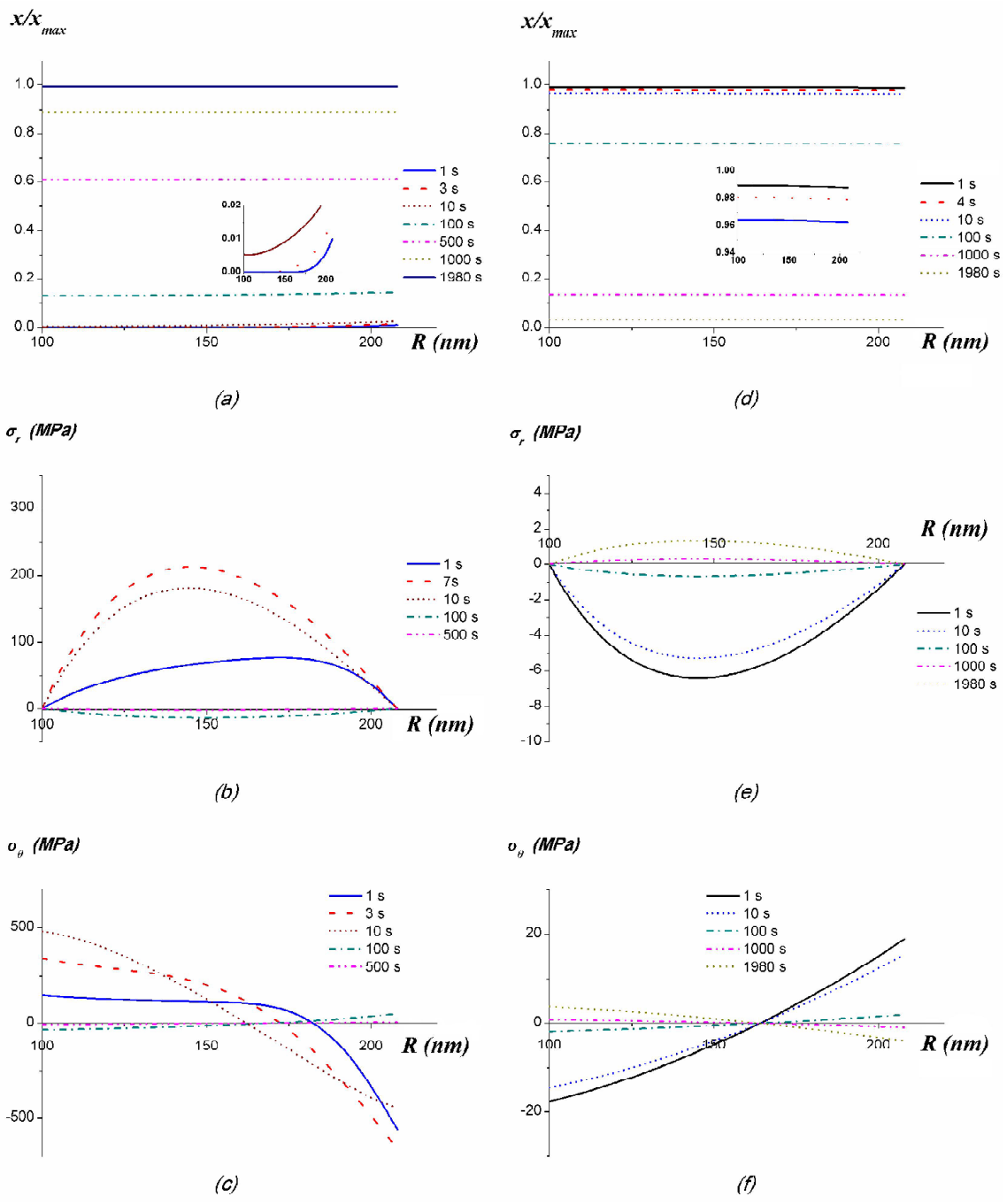

Figure 2.15 Concentration (a and d), radial (b and e), and hoop (c and f) stress evolution for lithiation (a-c) and delithiation (d-f) of a hollow spherical nanoparticle.

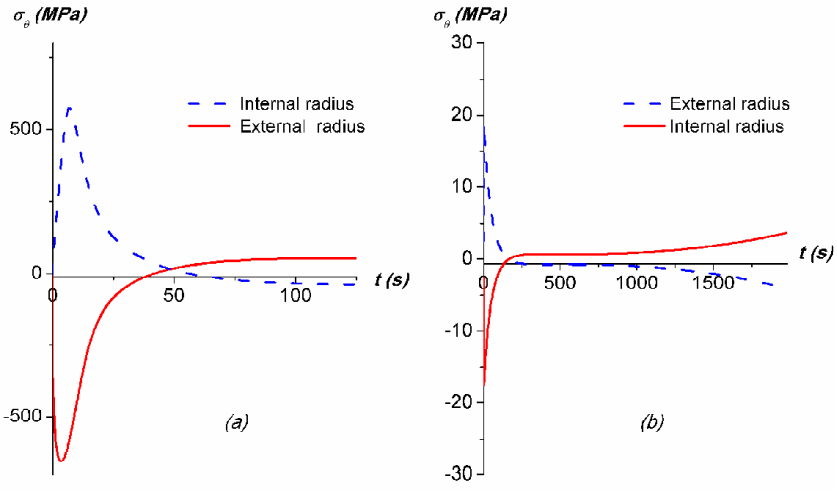

Figure 2.16 Hoop stress for the outer surface and the inner surface of a hollow nanoparticle during lithiation (a) and delithiation (b).

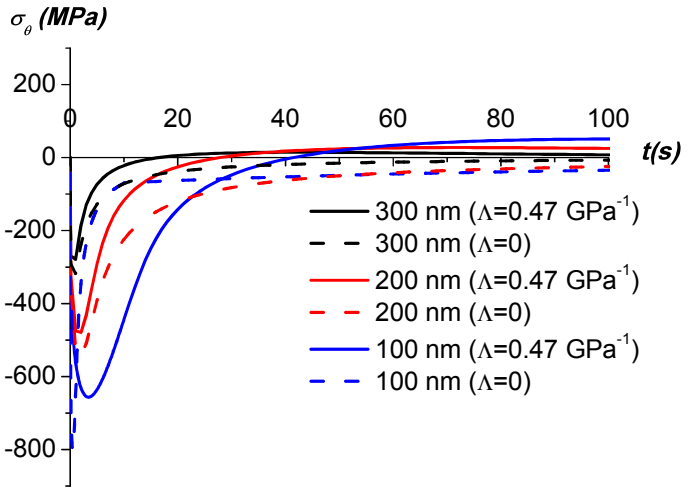

Figure 2.17 Hoop stress for the outer surface of different hollow nanoparticles during lithiation with and without relaxation.

kinetic equation for the deviatoric part of the compositional deformation rate was derived. The postulate of realizability was applied to two different problems, namely (1) to defining the contribution of deviatoric stresses $\boldsymbol{S}$ to the chemical potential, and to (2) determination of the compositional dissipation rate. Both results coincide and lead to coincidence of the direction tensors of the deviatoric part of the compositional deformation $\boldsymbol{d}_c^S$ rate and stress $\boldsymbol{S}$. With a series of simplifications, the simplest kinetic relationship between $\boldsymbol{d}_c^S$ and $\boldsymbol{S}$ contains just one constant, which was determined for lithiation of Si by fitting one of the points of the stress-lithium concentration x curve obtained experimentally or by first-principle simulations. After this, a quantitative correspondence between the predicted evolution of the biaxial stresses $\sigma(x)$ during lithiation-delithiation of Li_xSi on a rigid substrate for $0 \leq x \leq 2$ and those obtained experimentally and by atomistic simulations [20] was obtained. For comparison, a model in [5] based on viscoplastic flow requires two material parameters and the yield strength as a function of x to be fitted to experiments, but agreement with the same experiment for $\sigma(x)$ is not as good as that presented in the current paper. One of the important points is that elastic energy is defined in the unloaded (rather than reference) configuration, in which the elasticity rule is determined experimentally or in atomistic simulations. Otherwise, a large error in the elasticity rule will be introduced because of large volumetric compositional strain. This also leads to an extra term in the chemical potential.

An additional contribution to the chemical potential due to deviatoric stresses leads to an increase in the driving force for both compositional expansion and contraction and to some new phenomena. To chose which process (extraction or insertion) will occur at small driving forces, we assumed that the actual process minimizes the chemical potential. This leads to the jump in a flux, which can be used to check our prediction. The lack of the threshold for the stress relaxation (in contrast to plasticity in [5] and [6] or reactive flow in [20] and [19]) allowed us to suggest a simple method for reduction in internal stresses by cyclic change in Li concentration with a small amplitude. Our simulations are in qualitative agreement with available experiments [33]. The coupled problem formulation for diffusion, insertion/extraction, and mechanics is applied to lithiation and delithiation of thin film on a rigid substrate, solid, and hollow spherical nanoparticles. The effect of various parameters, including the contribution of

the deviatoric stress on the diffusion, stress relaxation, and geometric constraints, is elucidated.

Plastic flow is included in the current general theory, and different kinematic decompositions are considered. It is shown that an additive decomposition of compositional and plastic deformation rates has an advantage in comparison with multiplicative decomposition of the deformation gradient. Namely, each of these two processes can be described independently of each other, which is impossible with multiplicative decomposition.

The accuracy of the determination of stresses and their relaxation is important for evaluation of the fracture of anodes; see [10–13], and [14]. A similar approach can be developed for crystalline Si. In this case, initial anisotropy, chemical reaction, and multiple phase transformations should be taken into account. Indeed, during lithiation of the crystalline Si various compounds, such as $LiSi$, $Li_{12}Si_7$, $Li_{13}Si_4$, $Li_{15}Si_4$, $Li_{22}Si_5$, and pure Li, have different crystalline lattices [39]. Thus, initially lithiation is an insertion and compositional expansion, when Li atoms represent interstitials in the fcc lattice of Si. When x reaches unity, a chemical reaction occurs with formation of a tetragonal lattice. Thus, the concentration of interstitial Li jumps to zero, and the thermodynamic treatment should be built on a solid state-reaction rather than on compositional expansion. Further increase in x takes place as an insertion, until $x = 12/7$, when the next reaction occurs, leading to an orthorhombic lattice. We cannot exclude the fact that similar reactions do not occur in the amorphous Si–i.e., that the process occurs as sequential insertion and reaction–which requires more general thermodynamic description. Note that the above reactions in the crystalline Si occur if amorphization is suppressed. Usually, amorphization occurs at $x = 0.2$ [62–65] and is modeled as a reaction at the sharp interface [66]. Both for the lithiation reaction and amorphization, the anisotropic, stress-induced deviatoric compositional deformation rate can be introduced in a way similar to what we have done here.

Bibliography

[1] Larche, F., Cahn, J.W., 1973. A linear theory of thermochemical equilibrium of solids under stress. Acta Metall. 21, 1051-63.

[2] Larche, F., Cahn, J.W., 1978. Non-linear theory of thermochemical equilibrium of solids under stress. Acta Metall. 26, 53-60.

[3] Grinfeld, M.A., 1991. Thermodynamic Methods in the Theory of Heterogeneous Systems, Longman, Sussex.

[4] Wu, C.H., 2001. The role of Eshelby stress in composition-generated and stress-assisted diffusion. J. Mech. Phys. Solids 49, 1771-1794.

[5] Bower, A.F., Guduru, P.R., Sethuraman, V.A., 2011. A finite strain model of stress, diffusion, plastic flow, and electrochemical reactions in a lithiumion half cell. J. Mech. Phys. Solids 59, 804-828.

[6] Cui, Z., Gao, Z., Qu, J., 2012. A finite deformation stress-dependent chemical potential and its applications to lithium ion batteries. J. Mech. Phys. Solids 60, 1280-1295.

[7] Levitas, V.I., 2000b. Structural changes without stable intermediate state in inelastic material. Part II. Applications to displacive and diffusional-displacive phase transformations, strain-induced chemical reactions and ductile fracture. Int. J. Plasticity 16 (7-8), 851-892.

[8] Sethuraman, V.A., Hardwick, L.J., Srinivasan, V., Kostecki, R., 2010b. Surface structural disordering in graphite upon lithium intercalation/deintercalation. J. Power Sources 195, 3655-3660.

[9] Tarascon, J.M., Armand, M., 2001. Issues and challenges facing rechargeable lithium batteries. Nature 414, 359-367.

[10] Bhandakkar, T.K., Gao, H.J., 2010. Cohesive modeling of crack nucleation under diffusion induced stresses in a thin strip: Implications on the critical size for flaw tolerant battery electrodes. Int. J. Solids Struct. 47, 1424-34.

[11] Bhandakkar, T.K., Gao, H.J., 2011. Cohesive modelling of crack nucleation in a cylindrical electrode under axisymmetric diffusion induced stresses. J. Mech. Phys. Solids 48, 23042309.

[12] Haftbaradaran, H. and Gao, H.J., 2012. Ratcheting of silicon island electrodes on substrate due to cyclic intercalation. Appl. Phys. Lett. 100, 121907.

[13] Hu, Y.H., Zhao, X.H., Suo, Z., 2010. Averting cracks caused by insertion reaction in lithium-ion batteries. J. Mater. Res. 25, 1007-1010.

[14] McDowell, M.T., Ryu, L., Lee, S.W., Wang, C., Nix, W.D., Cui, Y. 2012. Studying the Kinetics of Crystalline Silicon Nanoparticle Lithiation with In Situ Transmission Electron Microscopy. Adv. Mater. 24, 6034-6041.

[15] Arico, A.S., Bruce, P., Scrosati, B., Tarascon, J.M., Schalkwijk, W.V., 2005. Nanostructured materials for advanced energy conversion and storage devices. Nat. Mater. 4, 366-377.

[16] Chan, C.K., Peng, H., Liu, G., McIlwrath, K., Zhang, X.F., Huggins, R.A., Cui, Y., 2008. High-performance lithium battery anodes using silicon nanowires. Nat. Nanotechnol. 3, 31-35.

[17] Liu, X.H., Wang, J.W., Huang, S., Fan,F., Huang, X., Liu, Y., Krylyuk, S., Yoo, J., Dayeh, S.A., Davydov, A.V., Mao, S.X., Picraux, S.T., S., Zhang, Li, J., Zhu, T., Huang, J.Y., 2012. In situ atomic-scale imaging of electrochemical lithiation in silicon. Nat. Nanotechnol. 7, 749-756.

[18] Wu, H., Chan, G., Choi, J.W., Ryu, I., Yao, Y., McDowell, M.T., Lee, S.W., Jackson, A., Yang, Y., Hu, L., Cui, Y., 2012. Stable cycling of double-walled silicon nanotube battery anodes through solid electrolyte interphase control. Nat. Nanotechnol. 7, 310-315.

[19] Zhao, K., Pharr, M., Cai, S., Vlassak, J.J., Suo, Z., 2011a. Large plastic deformation in high-capacity lithium ion batteries caused by charge and discharge. J. Am. Ceram. Soc. 94, S226-S235.

[20] Zhao, K., Tritsaris, G.A., Pharr, M., Wang, W.L., Okeke, O., Suo, Z., Vlassak, J.J., Kaxiras, E., 2012. Reactive flow in silicon electrodes assisted by the insertion of lithium. Nano Lett. 12, 4397-4403.

[21] Brassart, L., Suo, Z., 2012b. Reactive flow in solids. J. Mech. Phys. Solids 61, 61-77.

[22] Brassart, L., Suo, Z., 2012a. Reactive flow in large-deformation electrodes of lithium-ion batteries. Int. Appl. Mech. 4(3), 1-16.

[23] Liu, X.H., Zheng, H., Zhong, L., Huang, S., Karki, K., Zhang, L.Q., Liu, Y., Kushima, A., Liang, W.T., Wang, J.W., Cho, J.H., Epstein, E., Dayeh, S.A., Picraux, S.T., Zhu, T., Li, J., Sullivan, J.P., Cumings, J., Wang, C., Mao, S.X., Ye, Z.Z., Zhang, S., Huang, J.Y., 2011. Anisotropic Swelling and Fracture of Silicon Nanowires during Lithiation. Nano Lett. 11, 3312-3318.

[24] Yang, H., Huang, S., Huang; X., Fan, F., Liang, W., Liu, X.H., Chen, L.Q., Huang, J.Y., Li, J., Zhu, T., Zhang, S., 2012. Orientation-Dependent Interfacial Mobility Governs the Anisotropic Swelling in Lithiated Silicon Nanowires. Nano Lett. 12, 1953-1958.

[25] McDowell, M.T., Lee, S.W., Harris, J.T., Korgel, B.A., Wang, C., Nix, W.D., Cui, Y. 2013. In Situ TEM of Two-Phase Lithiation of Amorphous Silicon Nanospheres. Nano Lett. 13, 758-764.

[26] Wang, J.W., He, Y., F., Feifei, Liu, X.H., Xia, S., Liu, Y., Harris, C.T., Li, H., Huang, J.Y., Mao, S.X., Zhu, T., 2013. Two-Phase Electrochemical Lithiation in Amorphous Silicon. Nano Lett. 13, 709715.

[27] Levitas, V.I., 2000a. Structural Changes without Stable Intermediate State in Inelastic Material. Part I. General Thermomechanical and Kinetic Approaches. Int. J. Plasticity 16 (7-8), 805-849.

[28] Levitas, V.I., 1995a. The Postulate of Realizability: Formulation and Applications to Post-Bifurcation Behaviour and Phase Transitions in Elastoplastic Materials. Part I. Int. J. Eng. Sci. 33, 921-945.

[29] Levitas, V.I., 1995b. The Postulate of Realizability: Formulation and Applications to Post-Bifurcation Behaviour and Phase Transitions in Elastoplastic Materials. Part II. Int. J. Eng. Sci. 33, 947-971.

[30] Levitas, V.I., 1998a. Thermomechanical theory of martensitic phase transformations in inelastic materials. Int. J. Solids and Struct. 35, 889-940.

[31] Levitas V.I., 1998b. A New Look at the Problem of Plastic Spin Based on Stability Analysis. J. Mech. Phys. Solids, 46(3), 557-590.

[32] Levitas, V.I., Nesterenko, V.F., Meyers, M.A., 1998b. Strain-Induced Structural Changes and Chemical Reactions. I. Thermomechanical and Kinetic Models. Acta Materialia 46, 5929-5945.

[33] Sethuraman, V., Srinivasan, A.F., Bower, Guduru, P.R., 2010c. In situ measurements of stress-potential coupling in lithiated silicon. J. Electrochem. Soc. 157, A1253-A1261.

[34] Levitas, V.I., Samani, K., 2011a. Size and mechanics effects in surface-induced melting of nanoparticles. Nat. Commun. 2, 284.

[35] Levitas, V.I., Samani, K., 2011b. Coherent solid/liquid interface with stress relaxation in a phase-field approach to the melting/solidification transition. Phys. Rev. B. 84, 140103(R).

[36] Levitas, V.I., Attariani, H., 2013. Anisotropic Compositional Expansion and Chemical Potential for Amorphous Lithiated Silicon under Stress Tensor. Sci. Rep. 3, 1615.

[37] Levitas, V.I., 1996. Large Deformation of Materials with Complex Rheological Properties at Normal and High Pressure, Nova Science Publishers, New York.

[38] Moon, J., Cho, K., Cho, M., 2012. Ab-initio Study of Silicon and Tin as a Negative Electrode Materials for Lithium-ion Batteries. Int. J. Precis. Eng. Man. 113(7), 1191-1197.

[39] Shenoy, V.B., Johari, P., Qi, Y., 2010. Elastic softening of amorphous and crystalline Li-Si phases with increasing Li concentration: A first-principles study. J. Power Sources 195, 6825-6830.

[40] Lurie, A.I., 1990. Nonlinear Theory of Elasticity, North-Holland.

[41] Ziegler, H. 1983. An Introduction to Thermomechanics, North-Holland, Amsterdam.

[42] Levitas, V.I. and Ozsoy, I. B., 2009b. Micromechanical modeling of stress-induced phase transformations. Part 2. Computational algorithms and examples. Int. J. Plasticity, 2009, 25, 546-583.

[43] Levitas, V.I. and Ozsoy, I. B., 2009a. Micromechanical modeling of stress-induced phase transformations. Part 1. Thermodynamics and kinetics of coupled interface propagation and reorientation. Int. J. Plasticity, 25, 239-280.

[44] Levitas, V.I., Idesman, A.V., Stein, E., 1998a. Finite Element Simulation of Martensitic Phase Transitions in Elastoplastic Materials. Int. J. Solids and Structures, 35, 855-887.

[45] Levitas, V.I., 2002. Critical Thought Experiment to Choose the Driving Force for Interface Propagation in Inelastic Materials. Int. J. Plasticity, 18, 1499-1525.

[46] Idesman, A.V., Levitas, V.I., Stein, E., 2000. Structural Changes in Elastoplastic Materials: a Unified Finite Element Approach for Phase Transformation, Twinning and Fracture. Int. J. Plasticity, 16, 893-949.

[47] Levitas, V.I., Idesman, A.V., Olson, G.B., 1998. Continuum modeling of strain-induced martensitic transformation at shear-band intersections. Acta Materialia 47, 219-233.

[48] Levitas, V.I., Nesterenko, V.F., Meyers, M.A., 1998c. Strain-Induced Structural Changes and Chemical Reactions. II. Modeling of Reactions in Shear Band. Acta Materialia 46, 5947-5963.

[49] Levitas, V.I., 2012. Sublimation, chemical decomposition, and melting inside an elasto-plastic material: General continuum thermodynamic and kinetic theory. Int. J. Plasticity, 34, 41-60.

[50] Mandel, J., 1973. Equations constitutives et directeurs dans les milieux plastiques et visco-plastiques. Int. J. Solids and Struct. 9, 725-740.

[51] Dafalias, Y.F., 1984. The plastic spin concept and a simple illustration of its role in finite plastic transformations. Mech. Mater. 3, 223–233.

[52] Cuitino, A., Ortiz, M., 1992. A material-independent method for extending stress update algorithms from small-strain plasticity to finite with multiplicative kinematics. Eng. Comput. 9, 437-451.

[53] Weber, G., Anand, L., 1990. Finite deformation constitutive equations and a time integration procedure for isotropic hyperelastic-viscoplastic solids, Comput. Methods Appl. Mech. Eng. 79, 173-202.

[54] Idesman, A.V., Levitas, V.I., Stein, E., 1999. Elastoplastic Materials with Martensitic Phase Transition and Twinning at Finite Strains: Numerical Solution with the Finite Element Method. Comp. Meth. in Appl. Mech. and Eng. 173, 71-98.

[55] Levitas, V.I., Idesman, A.V., Olson, G.B., Stein, E., 2002. Numerical Modeling of Martensite Growth in Elastoplastic Material. Phil. Mag. A. 82(3), 429-462.

[56] Haftbaradaran, H., Song, J., Curtin, W.A., Gao, H.J., 2011. Continuum and atomistic models of strongly coupled diffusion, stress, and solute concentration. J. Power Sources 196, 361-370.

[57] Chen, C.H., Ding, N., Xu, J., Yao, Y.X., Wegner, G., Fang, X., Lieberwirth, I., 2009. Determination of the diffusion coefficient of lithium ions in nano-Si. Solid State Ionics 180 (23), 222-225.

[58] Rhodes, K., Dudney, N., Lara-Curzio, E., Daniel, C., 2010. Understanding the degradation of silicon electrodes for lithium-ion batteries using acoustic emission. J. Electrochem. Soc. 157 (12), A1354-A1360.

[59] Sethuraman, V.A., Chon, M.J., Shimshak, M., Van Winkle, N., Guduru, P.R., 2010a. In situ measurement of biaxial modulus of Si anode for Li-ion batteries. Electrochem. Commun. 12, 1614-1617.

[60] Golmon, S., Maute, K., Lee, S.H., Dunn, M.D., 2010. Stress generation in silicon particles during lithium insertion. Appl. Phys. Lett. 97, 033111.

[61] Yao, Y., McDowell, M.T., Ryu, I., Wu, H., Liu, N., Hu, L., Nix, W.D., Cui, Y., 2011. Interconnected Silicon Hollow Nanospheres for Lithium-Ion Battery Anodes with Long Cycle Life. Nano lett. 11, 2949-2954.

[62] Limthongkul, P., Jang, Y.I., Dudney, N.J., Chiang, Y.M., 2003. Electrochemically-driven solid-state amorphization in lithium-metal anodes. J. Power Sources 119, 604609.

[63] Wan, W.H., Zhang, Q.F., Cui, Y., Wang, E.G., 2010. First principles study of lithium insertion in bulk silicon. J. Phys. Condens. Matter 22 (41), 415501.

[64] Zhang, Q.F., Zhang, W.X., Wan, W.H., Cui, Y., Wang, E.G., 2010. Lithium insertion in silicon nanowires: an ab initio study. Nano Lett. 10 (9), 3243-3249.

[65] Zhao, K.J., Wang, W.L., Gregoire, J., Pharr, M., Suo, Z., Vlassak, J.J., Kaxiras, E., 2011b. Lithium-assisted plastic deformation of silicon electrodes in lithium-ion batteries: a rst-principles theoretical study. Nano Lett. 11 (7), 2962-2967.

[66] Cui, Z., Gao, F., Qu, J., 2013. Interface-reaction controlled diffusion in binary solids with applications to lithiation of silicon in lithium-ion batteries. J. Mech. Phys. Solids 61, 293-310.

CHAPTER 3. MECHANOCHEMICAL CONTINUUM MODELING OF NANOVOID NUCLEATION AND GROWTH IN REACTING NANOPARTICLES

Modified from a paper published in the Journal of Physical Chemistry C

Valery I. Levitas[1] and Hamed Attariani [2]

ABSTRACT

Hollow nanoparticles (NPs) are produced by void nucleation and growth during chemical reactions. However, there is no proper understanding of nucleation and growth mechanisms and their predictive modeling. Models based on the Kirkendall effect predict the process time, which is larger by orders of magnitude than in the experiment. This is why some works propose that a large tensile pressure in the core causes void nucleation. Here, a continuum-mechanics approach for nucleation and growth of a nanovoid in reacting NPs based on the Kirkendall effect is developed. In contrast to previous approaches, void nucleation and the effects of stresses are treated explicitly. The void nucleation condition vs. pressure, temperature, sizes of a vacancy, core material, and the initial reaction product layer is determined and a strong multifaceted effect of mechanics is revealed. Thus, with mechanics, a cluster consisting of four vacancies represents the supercritical nucleus. Surprisingly, the core is under compression (which eliminates fracture hypothesis), and compressive pressure and reduced temperature promote void nucleation by decreasing equilibrium concentration of vacancies at the void surface. However, they suppress void growth by reducing diffusion coefficients. Our model quantitatively describes

[1]Iowa State University, Departments of Aerospace Engineering, Mechanical Engineering, and Material Science and Engineering, Ames, Iowa 50011, U.S.A.
[2]Iowa State University, Department of Aerospace Engineering, Ames, Iowa 50011, U.S.A.

the experimental results for oxidation of copper NPs. A thermomechanical loading program is suggested to accelerate and control void nucleation and growth.

3.1 Introduction

Hollow NPs have diverse functionality due to their specific optical, electrical, magnetic, and other properties. They have low density, high specific surface area, and the ability to encompass another material in their internal volume. These characteristics make them an outstanding candidate in biomedical applications (drug delivery, disease diagnosis, and cancer therapy), lightweight filters, composites, catalysts, waste treatment, insulators, and photoelectric devices. [1, 2] The hollow in nanoparticles can be used to control their energetic behavior during combustion. [3] Understanding the mechanisms and parameters, that affect the hollow formation is a key issue for researchers. After the first synthesis of hollow nanoparticles [4] based on the Kirkendall effect, experimental studies have been done on void formation in Cu, Al, Fe, Zn, Co, and Cd NPs. [5–11] In, [4–9] the bare NP was exposed to the air to cause oxidation; hollow sulfides were formed in [10, 11]. Since diffusion of core material to oxide shell is faster than diffusion of oxide into metal core (the Kirkendall effect [12]), vacancy flux to the core leads to oversaturated vacancy state and nanovoid nucleation. While atomistic studies for model binary metals reproduce nucleation and growth of void, [13, 14] due to known limitation on size and time scales void nucleation was obtained near melting temperature only, while in experiments it occurs near room temperature. With the continuum approach, diffusional growth of nanovoid in a binary alloy without reaction was studied for cylinder [15] and a spherical particle. [16, 17] In all continuum approaches, nucleation of void was not considered, and mechanics was neglected. Because calculated growth time was larger by several orders of magnitude than in experiments, [17] the ability to explain void formation by the Kirkendall effect was doubted. It is proposed in [17] that tensile pressure in the core is developed due to misfit strain between metal and oxide and that causes void nucleation. In, [18] nucleation of the nanovoid caused by tensile stresses due to misfit strain was considered without diffusion. However, Refs. [17, 18] neglect surface tension and stresses, that in fact produce large compressive pressure in a core (see below). Void nucleation in elatoplastic material under ten-

sile stresses due to sublimation, sublimation via virtual melting, and fracture are considered in. [19–21] In phase-field approaches, [22,23] void nucleation occurs via spinodal decomposition for a very large concentration of vacancies or due to cavitation; [24] the results [19–24] are not applicable for our case. Thus, the mechanism of void nucleation and growth is currently not clear. In the paper, we developed a simple continuum approach for nucleation and growth of nanoviod in reacted NP that includes consideration of coupled core material reaction, diffusion of vacancies, diffusion of core material in reaction product shell, stress generation, and moving void and external surfaces. While equations are formulated for the general 3-D case, to obtain a simple and tractable solution, we consider a spherically symmetric problem. It is assumed that an q-vacancy cluster is formed at the center of a particle, which is considered as a void embryo. Concentration of vacancies at the void is equal to the thermodynamic equilibrium value n_{eq}, which depends on temperature, local pressure, surface energy, and void radius. The void will grow (i.e., it represents a supercritical nucleus), when the concentration of vacancies in the core $n_v > n_{eq}$, that provides vacancies fluxes toward the void. Thus, the void nucleation condition vs. external pressure p_e, temperature θ, and the radii of vacancy r_v, core material R_c, and reaction product shell R_s is determined. It is found that the core is under significant compressive pressure due to surface tension, which according to general wisdom, should suppress void nucleation and growth. However, a nontrivial point of our results is that *compressive pressure promotes void nucleation* by essentially decreasing n_{eq} at the void surface. Thus, with mechanics, a cluster consisting of $q = 4$ vacancies represents a supercritical nucleus. Similarly, *temperature decrease promotes nucleation*. However, both pressure increase and temperature decrease suppress void growth by reducing diffusion coefficients. Our model described well experimental results [5] for oxidation of Cu NPs of four sizes at three temperatures. Parametric study determined conditions for promoting void formation in particles of different sizes by controlling pressure, temperature, and internal stresses.

3.1.1 Governing equations

Since we apply our model to metal oxidation, we will henceforth call core a metal and shell an oxide. While often multiple voids nucleate near the core/shell interface, [8,25] we placed the

void at the center, similar to all previous works. Three different stages will be considered: (1) before void nucleation, (2) with all three regions, and (3) after the metal core has disappeared (Fig. 3.1). According to experiments, [5] it is assumed that oxide and oxygen do not diffuse into metal and that $R_c = const$. Also, oxidation reaction $xM + 0.5yO_2 \Rightarrow M_xO_y$ occurs at the external surface only. Below, subscripts $i = 1$ and $i = 2$ are referred to metallic atoms in

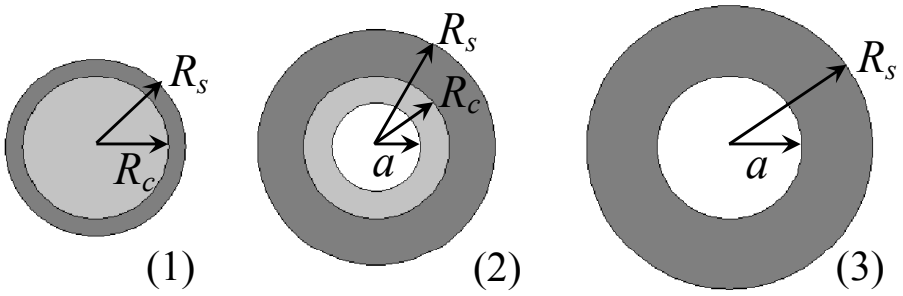

Figure 3.1 Particle geometry: (1) before void nucleation, (2) with all three regions, (3) after metal core disappeared.

the core and shell, respectively. Subscript s means symmetrization of a tensor; $\cdot$ and : mean contraction and double contraction of tensors or vectors, which are designated by bold-face letters; ∇ and $\boldsymbol{\nabla}^2$ are the gradient and Laplacian operators; $\boldsymbol{I}$ is the unit second-rank tensor.

Two diffusion equations are needed to model the diffusion of atoms in the shell and core. Furthermore, the void and outer surface of the NPs grow due to the vacancy annihilation and chemical reaction, respectively. The growth velocities of these surfaces are obtained by the conservation of mass. In this section, the coupled mechanical and diffusion equations as well as equations for growth velocities are derived. While there is significant change in shape due to mass transport, strains are considered to be *small*, which is confirmed by calculations. For simplicity, the temperature is assumed to be constant during the modeling. Due to smallness of the strains, there is no need to distinguish between undeformed (reference) and deformed (actual) volumes. The interstitial and substitutional diffusion equations can be found, e.g., in. [26–28] We added explicit pressure dependency of the diffusion coefficients and actual vacancy concentration dependence of the self-diffusion coefficient to the classic equations.

3.1.1.1 Diffusion in the core

The description of self-diffusion of atoms in a core requires consideration of two components, vacancy and metallic atoms.

Flux. In the framework of linear thermodynamics, one can derive the proportionality relation between the diffusive flux **j** and its conjugative driving force, gradient of chemical potential: [29–31]

$$\boldsymbol{j}_1 = -c_1 b_1 \boldsymbol{\nabla}\bar{\mu}; \quad \bar{\mu} = \mu_1 - \mu_v = \left.\frac{\partial\psi}{\partial c_1}\right|_{\boldsymbol{\varepsilon},\theta} - \left.\frac{\partial\psi}{\partial c_v}\right|_{\boldsymbol{\varepsilon},\theta}, \tag{1}$$

where μ_1 and μ_v are the chemical potentials of metallic atoms and vacancies, ψ is the free energy per unit volume, c_1 and c_v are the molar concentrations (i.e. number of moles per unit volume) of metallic atoms and vacancies, and b_1 is the atomic mobility. Derivatives in Eq. (1) are evaluated at fixed strain tensor $\boldsymbol{\varepsilon}$ and temperature θ. While it is convenient to perform some derivations using c_1 and c_v, the final results are more tractable in terms of n_1 and n_v, the molar fractions (i.e. number of moles of a specie per total number of moles) of the metallic atoms and vacancies in the core. They are related by $n_1 = c_1/c$; $n_v = c_v/c$; $c = c_1 + c_v$; $n_v = 1 - n_1$. [29] By definition, the molar volume of a metal with vacancies is $\overline{V} = 1/c$. [29] Due to small concentration of vacancies and corresponding small change in volume due to vacancies, the molar volume of metal $\overline{V}_m \simeq \overline{V}$; due to small elastic and thermal strains we assume that these molar volumes are constant. Thus, $n_1 = \overline{V}_m c_1$ and $n_v = \overline{V}_m c_v$. Therefore, Eq. (1) can be rewritten

$$\boldsymbol{j}_1 = -\frac{n_1 b_1}{\overline{V}_m}\boldsymbol{\nabla}\bar{\mu} = \boldsymbol{J}_1/\overline{V}_m; \quad \boldsymbol{J}_1 = n_1 b_1 \boldsymbol{\nabla}\bar{\mu} \tag{2}$$

in terms of the flux $\boldsymbol{J}_1$ and the molar fraction. Such a definition of the flux can be found, for example, in. [26] The free energy per unit volume for a stressed ideal solution is [32]

$$\begin{aligned} \psi(c_1,\theta,\boldsymbol{\varepsilon}) &= \psi^{mech}(\boldsymbol{\varepsilon}) + \psi^{d}(c_1,\theta); \\ \psi^{d}(c_1,\theta) &= c_1\mu_1^0 + c_v\mu_v^0 + R\theta\left[c_1 ln\frac{c_1}{c_1+c_v} + c_v ln\frac{c_v}{c_1+c_v}\right]; \\ \psi^{mech} &= 0.5\boldsymbol{\varepsilon}_e : \boldsymbol{E} : \boldsymbol{\varepsilon}_e, \end{aligned} \tag{3}$$

where R is the gas constant, μ_1^0 and μ_v^0 are the standard chemical potentials of metallic atoms and vacancies, $\boldsymbol{E}$ is the elastic moduli tensor, ψ^d and ψ^{mech} are the free energies of an ideal solution and strain energy per unit volume, and $\boldsymbol{\varepsilon}_e$ is the elastic strain tensor. The total strain tensor is decomposed to the diffusional $\boldsymbol{\varepsilon}_d$, thermal $\boldsymbol{\varepsilon}_\theta$ and elastic parts

$$\boldsymbol{\varepsilon} = \boldsymbol{\varepsilon}_e + \boldsymbol{\varepsilon}_d + \boldsymbol{\varepsilon}_\theta; \quad \boldsymbol{\varepsilon}_d = \omega_v^{'}\left(c_v - c_{v0}^{eq}\right)\boldsymbol{I}/3; \quad \boldsymbol{\varepsilon}_\theta = \alpha_1 \Delta\theta \boldsymbol{I}, \tag{4}$$

where α_1 is the linear thermal expansion coefficient of a core; $\Delta\theta = \theta - \theta_r, \theta_r = 300\,K$ is the room temperature; $\omega_v^{'}$ is the volumetric diffusion expansion coefficient of vacancies in the metal; c_{v0}^{eq} is the equilibrium molar concentration of vacancies at the initial pressure and simulation temperature. According to the definition of the chemical potential Eq. (1),

$$\bar{\mu} = \left.\frac{\partial \psi}{\partial c_1}\right|_{\boldsymbol{\varepsilon}} - \left.\frac{\partial \psi}{\partial c_v}\right|_{\boldsymbol{\varepsilon}} = \left[\frac{\partial \psi^d}{\partial c_1} + \left.\frac{\partial \psi^{mech}}{\partial c_1}\right|_{\boldsymbol{\varepsilon}}\right] - \left[\frac{\partial \psi^d}{\partial c_v} + \left.\frac{\partial \psi^{mech}}{\partial c_v}\right|_{\boldsymbol{\varepsilon}}\right]. \tag{5}$$

After substitution of Eq. (3) in Eq. (5), the chemical potential can be written as

$$\bar{\mu} = \left[\frac{\partial \psi^d}{\partial c_1}\right] - \left[\frac{\partial \psi^d}{\partial c_v} + \left.\frac{\partial \psi^{mech}}{\partial \boldsymbol{\varepsilon}_e}\right|_{\boldsymbol{\varepsilon}} : \frac{\partial \boldsymbol{\varepsilon}_e}{\partial \boldsymbol{\varepsilon}_d} : \frac{\partial \boldsymbol{\varepsilon}_d}{\partial c_v}\right] = \mu_1^0 - \mu_v^0 + R\theta \ln \frac{n_1}{n_v} - \omega_v^{'} p. \tag{6}$$

We took into account that $\boldsymbol{\sigma} = \frac{\partial \psi^{mech}}{\partial \boldsymbol{\varepsilon}_e}$ is the stress tensor, $\frac{\partial \boldsymbol{\varepsilon}_e}{\partial \boldsymbol{\varepsilon}_d}$ is the negative forth-rank unit tensor, $\left.\frac{\partial \psi^{mech}}{\partial \boldsymbol{\varepsilon}_e}\right|_{\boldsymbol{\varepsilon}} : \frac{\partial \boldsymbol{\varepsilon}_e}{\partial \boldsymbol{\varepsilon}_d} : \frac{\partial \boldsymbol{\varepsilon}_d}{\partial c_v} = -\boldsymbol{\sigma} : \boldsymbol{I}\omega_v^{'}/3 = p\omega_v^{'}$, where $p = -\boldsymbol{\sigma} : \boldsymbol{I}/3$ is the pressure.
The diffusional strain can be rewritten as $\boldsymbol{\varepsilon}_d = \omega_v(1 - n_1 - n_{v0}^{eq})\boldsymbol{I}/3$ with the volumetric expansion coefficient $\omega_v = \omega_v^{'}/\overline{V}_m$, $n_v = \overline{V}_m c_v = (1 - n_1)$, n_{v0}^{eq} for the equilibrium molar fraction of vacancies at the initial pressure and simulation temperature.Then, the chemical potential is [26]

$$\mu = \mu_1^0 - \mu_v^0 + R\theta \ln \frac{n_1}{1 - n_1} - \overline{V}_m \omega_v p. \tag{7}$$

Substituting Eq. (7) in Eq. (2), we obtain

$$\boldsymbol{J}_1 = -b_1 n_1 \boldsymbol{\nabla} \bar{\mu} = -b_1 n_1 \left[\frac{R\theta \boldsymbol{\nabla} n_1}{n_1 n_v} - \omega_v \overline{V}_m \boldsymbol{\nabla} p\right]. \tag{8}$$

Next, we elaborate on the equation for the atomic mobility for the substitutional diffusion in the non-equilibrium state

$$b_1(\theta, p, n_v) = \frac{D_1}{R\theta} = \frac{D_v n_v}{R\theta} = \frac{1}{R\theta}\frac{D_1^{eq} n_v}{n_{eq}}. \tag{9}$$

Here $D_1^{eq} = D_1^0 \exp(-\frac{E_1^a + p\Delta V_1}{R\theta}) = D_v n_{eq}$ is the self-diffusion coefficient at the equilibrium concentration of vacancies n_{eq}, D_1^0, E_1^a, ΔV_1 are the pre-exponent factor, activation energy, and activation volume of diffusion in the core, respectively, and D_v is the diffusion coefficient of vacancies. Therefore, the mobility depends on pressure, temperature, and vacancy concentration. After substitution of Eq. (9) into Eq. (8), the flux is rewritten as

$$\boldsymbol{J}_1 = \frac{D_1^{eq}}{n_{eq}} \left[-\boldsymbol{\nabla} n_1 + \frac{n_1(1-n_1)\omega_v \overline{V}_m}{R\theta} \boldsymbol{\nabla} p \right]. \tag{10}$$

Equilibrium concentration of vacancy. The equilibrium concentration of vacancies is [33]

$$n_{eq} = \exp\left(-\frac{G_v^f}{R\theta}\right) = \exp\left(-\frac{H_v^f - \theta S_v^f}{R\theta}\right), \tag{11}$$

where H_v^f, S_v^f, and G_v^f are the enthalpy, entropy, and Gibbs energy of vacancy formation. At the interface with a curvature $1/r$, the Gibbs energy is changed by

$$\Delta G^{cur} = \frac{2\gamma V_f}{r}, \tag{12}$$

where γ is the surface energy, $V_f = (1-f)\Omega_1$ is the formation volume of a vacancy, Ω_1 is the atomic volume of metal, and f is the vacancy relaxation factor. Taking into account Eq. (12) and $H_v^f = E_v^f + pV_f$, where E_v^f is the formation energy of vacancy, the equilibrium concentration of vacancies can be written as

$$n_{eq} = \exp\left(-\frac{E_v^f - \theta S_v^f}{R\theta}\right) \exp\left(-\frac{pV_f}{R\theta}\right) \exp\left(\frac{2\gamma V_f}{rR\theta}\right). \tag{13}$$

For the bulk, the effect of surface energy (curvature) and the last exponent in Eq. (13) disappears:

$$n_{eq} = \exp\left(-\frac{E_v^f - \theta S_v^f}{R\theta}\right) \exp\left(-\frac{pV_f}{R\theta}\right). \tag{14}$$

Mass balance. The mass balance equation for diffusing species is $\dot{n}_1 + \overline{V}\boldsymbol{\nabla} \cdot \boldsymbol{j}_1 = 0$ [32, 34] and with $\overline{V} \simeq \overline{V}_m$ and Eq. (2), we obtain [26]

$$\dot{n}_1 + \boldsymbol{\nabla} \cdot \boldsymbol{J}_1 = 0. \tag{15}$$

Substituting Eq. (10) in Eq. (15), the diffusion equation is obtained

$$\begin{aligned} \dot{n}_1 = \nabla\left(\frac{D_1^{eq}}{n_{eq}}\right)\nabla n_1 + \frac{D_1^{eq}}{n_{eq}}\nabla^2 n_1 - \frac{(1-n_1)n_1\omega_v\overline{V}_m}{R\theta}\nabla\left(\frac{D_1^{eq}}{n_{eq}}\right)\nabla p \\ - \frac{D_1^{eq}(1-2n_1)\omega_v\overline{V}_m\nabla n_1\nabla p}{n_{eq}R\theta} - \frac{D_1^{eq}n_1(1-n_1)\omega_v\overline{V}_m\nabla^2 p}{n_{eq}R\theta}. \end{aligned} \tag{16}$$

Since $\nabla\frac{D_1^{eq}}{n_{eq}} = -\frac{D_1^{eq}\Delta\overline{V}}{R\theta n_{eq}}\nabla p$, with $\Delta\overline{V} = \Delta V_1 - V_f$, the diffusion equation can be rewritten as

$$\begin{aligned}\dot{n}_1 &= \frac{D_1^{eq}}{n_{eq}}\left[\nabla^2 n_1 + \frac{(1-n_1)n_1\omega_v\overline{V}_m\Delta\overline{V}(\nabla p)^2}{(R\theta)^2}\right. \\ &\left. - \frac{[(1-2n_1)\omega\overline{V}_m + \Delta\overline{V}]\nabla n_1\nabla p}{R\theta} - \frac{n_1(1-n_1)\overline{V}_m\omega_v\nabla^2 p}{R\theta}\right].\end{aligned} \tag{17}$$

3.1.1.2 Diffusion in the shell

In the shell, the metallic atoms are diffusing species and oxide atoms act as a matrix. For interstitial diffusion, the flux is defined in the same way as in Eq. (2)

$$\boldsymbol{J}_2 = -n_2 b_2 \boldsymbol{\nabla}\mu_2 \ ; \ \ \mu_2 = \left.\frac{\partial\psi}{\partial c_2}\right|_{\boldsymbol{\varepsilon},\theta}, \tag{18}$$

where the subscript 2 is for metal atoms in the shell. The atomic mobility is

$$b_2(\theta,p) = \frac{D_2}{R\theta}; \quad D_2 = D_2^0\exp\left(-\frac{E_2^a + p\Delta V_2}{R\theta}\right). \tag{19}$$

The free energy per unit volume for a stressed ideal solution is similar to Eq. (3):

$$\begin{aligned}\psi(c_2,\theta,\boldsymbol{\varepsilon}) &= \psi^{mech}(\boldsymbol{\varepsilon}) + \psi^d(c_2,\theta); \\ \psi^d(c_2,\theta) &= c_2\mu_2^0 + c_h\mu_h^0 + R\theta\left[c_2 ln\frac{c_2}{c_2+c_h} + c_h ln\frac{c_h}{c_2+c_h}\right]; \\ \psi^{mech} &= 0.5\boldsymbol{\varepsilon}_e : \boldsymbol{E} : \boldsymbol{\varepsilon}_e,\end{aligned} \tag{20}$$

where μ_2^0 and μ_h^0 are standard chemical potentials of diffusing and matrix atoms and c_2 and c_h are the molar concentrations of diffusing and matrix atoms. The chemical potential can be calculated similarly to the substitutional diffusion: [26, 28]

$$\mu_2 = \mu_2^0 + R\theta\ln n_2 + \omega_2\overline{V}_s p, \tag{21}$$

where $\overline{V}_s$ is the molar volume of a matrix (oxide).

Flux. Combining Eqs. (18), (19), and (21), the flux of diffusing atoms in the shell can be expressed as

$$\boldsymbol{J}_2 = -D_2\left[\boldsymbol{\nabla}n_2 + \frac{n_2\omega_2\overline{V}_s\boldsymbol{\nabla}p}{R\theta}\right]. \tag{22}$$

Mass balance. The mass balance equation for metal atoms in a shell is

$$\dot{n}_2 + \boldsymbol{\nabla}\cdot\boldsymbol{J}_2 = 0. \tag{23}$$

Substituting Eq. (22) in Eq. (23), we obtain the diffusion equation:

$$\dot{n}_2 = D_2 \left[\nabla^2 n_2 + \frac{1}{R\theta}(\omega_2 \overline{V}_s - \Delta V_2)\nabla n_2 \nabla p + \frac{\omega_2 \overline{V}_s n_2 \nabla^2 p}{R\theta} - \frac{\omega_2 \Delta V_2 \overline{V}_s n_2 (\nabla p)^2}{(R\theta)^2} \right]. \tag{24}$$

3.1.1.3 Mass balance for the outer surface

When the metal atoms reach the outer surface and react with the oxygen, it is assumed that the reaction rate is infinite, i.e., all metallic atoms that reach the outer surface react with oxygen instantaneously and form the oxide layer on the outer surface. If metallic atoms will deposit on the external surface without reaction, then the outer boundary velocity $v = J_2$. For a general oxidation reaction, $xM + 0.5yO_2 \Rightarrow M_xO_y$, instead of the volume of x moles of metal, $x\overline{V}_m$, one obtains volume of one mole of oxide, $\overline{V}_s$. Thus,

$$\boldsymbol{v} = \frac{\boldsymbol{J_2}\overline{V}_s}{x\overline{V}_m}. \tag{25}$$

2.4. Mass balance for the void interface

The velocity of void interface is

$$\dot{\boldsymbol{a}} = \left(\boldsymbol{J}_v^+ - \boldsymbol{J}_v^- \right) / \left(n_v^+ - n_v^- \right), \tag{26}$$

where superscript $-$ denotes a core and $+$ indicates a void. The vacancy concentration in the void region $n_v^+ = 1$ and near the void surface $n_v^- = n_{eq}$ according to boundary conditions; additionally, $J_v^+ = 0$. In the core, the metallic atoms exchange their positions with vacancies. Therefore, the flux of vacancies is equal to the negative flux of metallic atoms:

$$\boldsymbol{J}_v^- = -\boldsymbol{J_1} = -\frac{D_1^{eq}}{n_{eq}} \left[-\boldsymbol{\nabla} n_1 + \frac{(1-n_1) n_1 \omega_v \overline{V}_m}{R\theta} \boldsymbol{\nabla} p \right]. \tag{27}$$

Also, the unit normal vector on the void surface in negative. Substituting Eq. (27) in Eq. (26), one obtains the velocity of the void growth

$$\dot{a} = -\frac{D_1^{eq}}{n_{eq}(1-n_{eq})} \left[-\nabla n_1 + \frac{(1-n_1) n_1 \omega_v \overline{V}_m}{R\theta} \nabla p \right]. \tag{28}$$

3.1.2 Complete coupled system of equations

Below we will collect only those equations that are used in numerical simulations.

Diffusion of metallic atoms in the core:

$$\dot{n}_1 = \frac{D_1^{eq}}{n_{eq}}\left[\nabla^2 n_1 + \frac{(1-n_1)n_1\omega_v\overline{V}_m\Delta\overline{V}(\nabla p)^2}{(R\theta)^2} - \frac{[(1-2n_1)\omega\overline{V}_m + \Delta\overline{V}]\nabla n_1\nabla p}{R\theta} - \frac{n_1(1-n_1)\overline{V}_m\omega_v\nabla^2 p}{R\theta}\right]. \tag{29}$$

Diffusion of metallic atoms in the shell:

$$\dot{n}_2 = D_2\left[\nabla^2 n_2 + \frac{1}{R\theta}(\omega_2\overline{V}_s - \Delta V_2)\nabla n_2\nabla p + \frac{\omega_2\overline{V}_s n_2\nabla^2 p}{R\theta} - \frac{\omega_2\Delta V_2\overline{V}_s n_2(\nabla p)^2}{(R\theta)^2}\right]; \tag{30}$$

$$D_i = D_0^i\exp\left(-\left(E_i^a + \Delta V_i p\right)/R\theta\right), \quad i = 1, 2.$$

Equilibrium concentration of vacancies in a bulk:

$$n_{eq} = \exp\left(-\frac{E_v^f - \theta S_v^f}{R\theta}\right)\exp\left(-\frac{pV_f}{R\theta}\right). \tag{31}$$

Strain-displacement relationship and strain decomposition:

$$\boldsymbol{\varepsilon} = (\boldsymbol{\nabla u})_s, \ \boldsymbol{\varepsilon} = \boldsymbol{\varepsilon}_e + \boldsymbol{\varepsilon}_\theta + \boldsymbol{\varepsilon}_d, \ \boldsymbol{\varepsilon}_\theta = \alpha_i\Delta\theta\boldsymbol{I}, \ \boldsymbol{\varepsilon}_d^1 = \omega_v(1 - n_1 - n_{v0}^{eq})\boldsymbol{I}/3, \ \boldsymbol{\varepsilon}_d^2 = \omega_2 n_2\boldsymbol{I}/3. \tag{32}$$

Hooke's law, pressure, and equilibrium equation:

$$\boldsymbol{\sigma} = \boldsymbol{E} : \boldsymbol{\varepsilon}_e; \qquad p = -\boldsymbol{\sigma} : \boldsymbol{I}/3; \qquad \boldsymbol{\nabla}\cdot\boldsymbol{\sigma} = 0. \tag{33}$$

The coupled system of Eqs. (29)-(33) is solved numerically for the three different stages in our problem: (1) before void nucleation, (2) with all three regions, and (3) after the metal core has disappeared (Fig. 3.1). The following boundary conditions are applied in each stage:

1) Before void nucleation

$$\begin{aligned} &at \quad r = 0: \quad J_1 = 0; \quad u = 0; \\ &at \quad r = R_c = const: \quad u_1 = u_2; \quad \sigma_r^1 - \sigma_r^2 = -2\gamma_{cs}/R_c; \quad J_1 = J_2; \quad n_2 \le n_{\max}; \\ &at \quad r = R_s: \quad \sigma_r^2 = -2\gamma_s/R_s + p_e; \quad n_2 = 0; \quad \dot{R}_s = -J_2\bar{V}_s/x\bar{V}_m. \end{aligned} \tag{34}$$

2) With all three regions

$$
\begin{aligned}
at \quad r &= a: \quad 1-n_1 = n_v = n_{eq} = \exp\left(-\frac{E_v^f - \theta S_v^f}{R\theta}\right)\exp\left(-\frac{p(a)V_f}{R\theta}\right)\exp\left(\frac{2\gamma V_f}{rR\theta}\right); \\
\sigma_r &= -2\gamma_a/a; \quad \dot{a} = -J_1/(1-n_{eq}); \qquad (35) \\
at \quad r &= R_c = const: \quad u_1 = u_2; \quad \sigma_r^1 - \sigma_r^2 = -2\gamma_{cs}/R_c; \quad J_1 = J_2; \quad n_2 \le n_{\max}; \\
at \quad r &= R_s: \quad \sigma_r^2 = -2\gamma_s/R_s + p_e; \quad n_2 = 0; \quad \dot{R}_s = -J_2\bar{V}_s/x\bar{V}_m.
\end{aligned}
$$

3) After metal core disappeared

$$
\begin{aligned}
at \quad r &= R_c = const: \quad J_1 = 0; \quad \sigma_r = -2\gamma_a/a; \qquad (36) \\
at \quad r &= R_s: \quad \sigma_r^2 = -2\gamma_s/R_s + p_e; \quad n_2 = 0; \quad \dot{R}_s = -J_2\bar{V}_s/x\bar{V}_m.
\end{aligned}
$$

For all cases, the fluxed are:

$$
\boldsymbol{J_1} = \frac{D_1^{eq}}{n_{eq}}\left[-\boldsymbol{\nabla} n_1 + \frac{(1-n_1)n_1\omega_v\overline{V}_m}{R\theta}\boldsymbol{\nabla} p\right]; \quad \boldsymbol{J}_2 = -D_2\left[\boldsymbol{\nabla} n_2 + \frac{n_2\omega_2\overline{V}_s\boldsymbol{\nabla} p}{R\theta}\right]. \qquad (37)
$$

Here, n_{max} is maximum solubility of metal in oxide. Eqs. (34)-(36) contain continuity of displacements and fluxes of metal atoms, as well as jump conditions for radial stresses σ_r. Condition $n_2 = 0$ at $r = R_s$ is the consequence of the assumption on infinite reaction rate. Indeed, as soon as metal atoms appear at the external surface, they are consumed by reaction. Condition (35) for the vacancy concentration n_v means that at the void surface it is always equal to n_{eq}, similar to. [15] In addition to the dependence of n_{eq} on temperature and surface, we took into account the effect of pressure p, which, as was shown, is very important.

Initial conditions

As an initial state, we consider a core-shell system without a void at a chosen temperature θ, that produces initial stresses $\boldsymbol{\sigma}^{in}$ (in particular, pressure p^{in}) due to different thermal expansion coefficients of the core and shell. In addition:

$$
\begin{aligned}
Core \quad &: \quad 1-n_1 = n_v = n_{v0}^{eq} = e^{-\frac{E_v^f - s_v^f\theta}{R\theta}} e^{-\frac{V_f p_1^{in}}{R\theta}}. \qquad (38) \\
Shell \quad &: \quad n_2 = 0.
\end{aligned}
$$

Note that p_1^{in} can be calculated analytically using Eq. (40). For example, $p_1^{in} = 0.716\,GPa$ for a $R_c = 9.05nm$ at 373 K. The solution from the previous stage is used as the initial condition

for the next stage.

4. Materials Parameters

We use in the calculations the following material parameters for Cu/Cu_2O nanoparticles: radii of vacancy, $r_v = 0.199\,nm$; atomic volume of Cu, $\Omega_1 = 1.18 \times 10^{-29}\,m^3/atom$ and vacancy relaxation factor, $f = 0.3$, i.e. $V_f = 0.7\Omega_1\,m^3/atom$; [35] Cu elastic shear $G_1 = 22.5\,GPa$ and bulk $K_1 = 143.33\,GPa$ moduli; [36] Cu_2O elastic shear $G_2 = 8\,GPa$ and bulk $K_2 = 111.33\,GPa$ moduli; [37] Cu linear thermal expansion coefficient, $\alpha_1 = 1.72 \times 10^{-5}\,1/^{\circ}C$; [38] Cu_2O linear thermal expansion coefficient, $\alpha_2 = 1.05 \times 10^{-6}\,1/^{\circ}C$; [39] Cu molar volume, $\overline{V}_m = 7.1 \times 10^{-6}\,m^3/mole$; Cu_2O molar volume, $\overline{V}_s = 23.31 \times 10^{-6}\,m^3/mole$; [5] volumetric diffusion expansion coefficient of vacancy in Cu, $\omega_v = -0.3$; [35] volumetric diffusion expansion coefficient of Cu in Cu_2O, $\omega_2 = 0.256$; [40] pre-exponent factor for self-diffusion coefficient of Cu, $D_0^1 = 7.8 \times 10^{-5}\ m^2/s$; activation energy for Cu self-diffusion coefficient, $E_1^a = 211.3\,KJ/mol$; [41] surface energy of Cu, $\gamma_a = 1.79\,J/m^2$ [42] (due to the lack of experimental data, we assumed that the surface energy of core/shell interface, γ_{cs}, and Cu_2O surface, γ_s, are equal to the Cu surface energy γ_a), activation volume of self-diffusion coefficient, $\Delta V_1 = 0.6\Omega_1\,m^3/atom$ [30] (due to lack of data, we assumed that the $\Delta V_2 = \Delta V_1$); energy of vacancy formation of Cu, $E_v^f = 103.24\,KJ/mole$; and entropy of vacancy formation of Cu, $s_v^f = 1.46 \times 10^{-5}\,R$. [43]

The diffusion coefficient of Cu in Cu_2O at the nanoscale, D_2, and maximum solubility of Cu in Cu_2O could not be found in the literature. At the macro scale, D_2 is of the order of $10^{-24}\,m^2/s$ [44] at $\theta = 373\,K$; however, it is expected to be much larger at the nanoscale. To justify this, we analyze available data for diffusion of Al in aluminum oxide. Thus, for bulk material the diffusion coefficient of Al in α-alumina at 800-950 ^0C is $D = 10^{-18} cm^2/s$. [45] Data collected in [7] show the same order of magnitude but for 1200 ^0C. In molecular dynamics simulations, the diffusivity of aluminum [46] has an extremely high order of magnitude of $10^{-4} cm^2/s$ at 400 K. In, [47] the diffusion coefficient of Al in various types of alumina (amorphous and crystalline) has been determined for particle radii from 2.8 to 4 nm and oxide shell from 1 to 2 nm using molecular dynamics. For 1000 K, the value of $D \simeq 4 \cdot 10^{-5} cm^2/s$ has been obtained. In [48] $D \simeq 4 \cdot 10^{-9} cm^2/s$ at 873 K was obtained to fit oxidation time

of a nanoparticle to experimental value of 1 s. Independent of significant scatter, the drastic increase in diffusion coefficient for nanoscale particles and shell is clearly visible.

Thus, these parameters, D_2 and $n_{\max}$, will be found by fitting experiments. First, we found $D_2(373\,K) = 10^{-18}\,m^2/s$ and $n_{max} = 0.009$, which give the good consistency with the experiment data on the oxide thickness $\delta = R_s - R_c$ vs. time t for the particle with $R_c = 9.05\,nm$ at $\theta = 373\,K$. Second, keeping n_{max}, the diffusion coefficient D_2 of Cu in Cu_2O was varied to fit experimental data for a particle with $R_c = 4.26\,nm$ at $\theta = 323\,K$. With these two fitted diffusion coefficients, one can extract $D_1^0 = 4.017 \times 10^{-12}\,m^2/s$ and $E_2^a = 47.156\,KJ/mol$.

3.1.3 Void Nucleation Criterion

At the moving void surface of the radius a, we put that the vacancy concentration n_v is always equal to its equilibrium value n_{eq}, similar to. [15] In addition to the dependence of n_{eq} on the temperature θ and surface energy γ in, [15] we took into account the effect of pressure $p(a)$ at the void surface Eq. (35), which, as will be shown below, is very important. We will define supercritical void as the void that can grow; i.e., when n_{eq} at its surface is smaller than n in the surrounding. Then vacancy flux will be directed toward the void and cause its growth. The radius of the void, which represents the q-vacancy cluster, is determined by $a = r_v q^{1/3}$. This approximation shows good correspondence with data in [35] for stable 3- and 4-vacancy clusters in Cu. Plots of equilibrium concentration of vacancy n_{eq} (Eq. (35)) at the surface of the void consisting of q vacancies vs. temperature for several values of q and pressures are shown in Fig. 3.2. The smaller value n_{eq} has the larger probability of void nucleation, because it is easier to reach and exceed this value in the surrounding of a void. The main *counterintuitive conclusion* coming from Fig. 3.2 is that compressive pressure promotes supercritical void nucleation. Indeed, general wisdom is that pressure suppresses void formation. However, in our case, pressure, reducing n_{eq} at the void surface, promotes transport of vacancies toward the void, causing void growth. Note that the promoting effect of pressure on void nucleation, based on a completely different consideration, was found in. [49] It follows from Eq. (35) that at $\theta = 323\,K$ and $p = 0.716$ GPa (which corresponds, e.g., to free particle with $R_c = 9.05\,nm$ and $R_s = 11.55\,nm$), allowing for pressure reduces n_{eq} by a factor of 3.8. Also, temperature

suppresses supercritical void nucleation.

Below, we connect the external pressure p_e and pressure at the void surface, assuming homogeneous distribution of n_1 and n_2. First, elastic solution for hollow sphere [50] results in the following pressure distribution in the core:

$$p(r) \quad = \quad (-2\gamma_1 W^3/a - \sigma_r^1(R_c))/(1-W^3), \quad W = a/R_c, \tag{39}$$

where σ_r^1 is the radial stresses in core. For nucleation $W \ll 1$ and one obtains $p(a) = -\sigma_r^1(R_c)$, which is independent of surface tension at the void surface. Thus, a very small void, while changing all stresses, does not change pressure in a core and keeps the pressure in a core homogeneous. To connect external pressure p_e with pressure in a core, we can use the equation for a solid core/shell system. [3]

$$p = \frac{12(m^3-1)\Delta\varepsilon^{in} G_2 K_1 K_2}{H} + \frac{2K_1(4G_2+3m^3K_2)\gamma_1}{R_s H} + \frac{(2\gamma_2 + p_e R_s m)m^2 K_1(4G_2+3K_2)}{R_s H}, \tag{40}$$

where $m = R_s/R_c$,

$$\Delta\varepsilon^{in} = (\alpha_2-\alpha_1)\Delta\theta + \frac{1}{3}[\omega_2 n_2 - \omega_1(n_v - n_{eq})], \quad H = 3K_1K_2m^3 + 4G_2(K_1 + (m^3-1)K_2), \tag{41}$$

K_i and G_i are the bulk and shear elastic constants. Eq. (40) allows one to predict the effect of various particle parameters, external pressure, and temperature on pressure in core for small void size (in particular, during nucleation), and consequently, on the nucleation condition. Thus, external pressure essentially increases p, but this increase reduces with m; n_1 and n_2 decrease p, and this decrease grows with m; also, temperature rise slightly increases pressure, and this rise grows with m. Increase in particle size reduces pressure contribution due to surface tension, which is the only pressure source for $p_e = 0$.

Here certain criteria are explained thus eventually leading to a foregone conclusion.

3.1.4 Numerical Method

The finite element-method code COMSOL Multiphysics was utilized to iteratively solve the coupled system of equations (29)-(33) for each time step. Displacement and concentration fields have been considered as primary variables. Solutions of equations of elasticity theory for

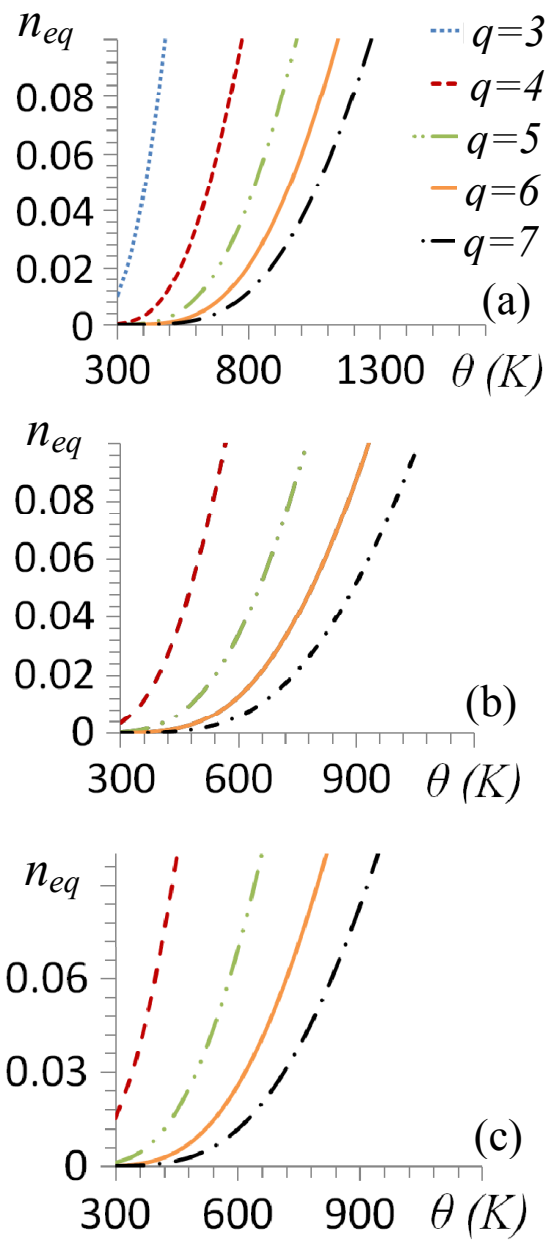

Figure 3.2 Equilibrium concentration of vacancies (Eq.(35)) at the surface of void consisting of q vacancies vs. temperature for different external pressures at the void surface: (a) $p(a)$ =2 GPa, (b) $p(a)$ =0.716 GPa, and (c) $p(a) = 0$.

given n_1 and n_2 distributions have been obtained using the Structural Mechanics module of COMSOL at each time step. After finding nodal displacements, strains and stresses (including pressure) can be found using Eqs. (32) and (33). The pressure field was used for solutions of diffusion Eqs. (29)-(31) for the same time step in the main module of COMSOL Multiphysics. After obtaining increments of a and R_s by integrating Eq. (35), the geometry was updated using the Arbitrary Lagrangian-Eulerian (ALE) technique. Quintic Lagrangian elements are used for both the mechanical and diffusion equations. The total number of integration points was 1290, and the time step varied from $0.001\,s$ to $0.15\,s$ in different stages.

Note that all of the main types of pressure distributions for each of the three stages were compared with the developed analytical solution and that the results are in very good correspondence. Our analytical solution generalizes this in [51] for the case with the prescribed heterogeneous n_1 and n_2 distributions, which was taken from numerical simulations.

3.1.5 Void and Oxide Growth

3.1.5.1 Oxide growth

We simulated the oxidation and hollow formation and growth for three temperatures (323, 343, and 373 K) and four NP core radii (4.26 nm, 9.05 nm, 11.5 nm, and 15.9 nm) with initial shell thickness of 2.5 nm. [5] For $R_c = 9.05\,nm$ at $\theta = 373\,K$, when n_v at the center reaches $n_{eq} = 0.0154$, a 4-vacancy nanovoid is introduced at the center of NP. Comparison of the results of numerical simulation for the oxide layer thickness h_s vs. time for Cu particles of four different sizes with experiments in Fig. 3.3 shows very good consistency; one has to keep in mind significant scatter in particle sizes and shell thicknesses in experiments. Note that the final oxide thickness is determined by the mass balance, which is satisfied in our simulations. Thus, discrepancy with experiment in final oxide thickness is related to an error of presentation of experimental results.

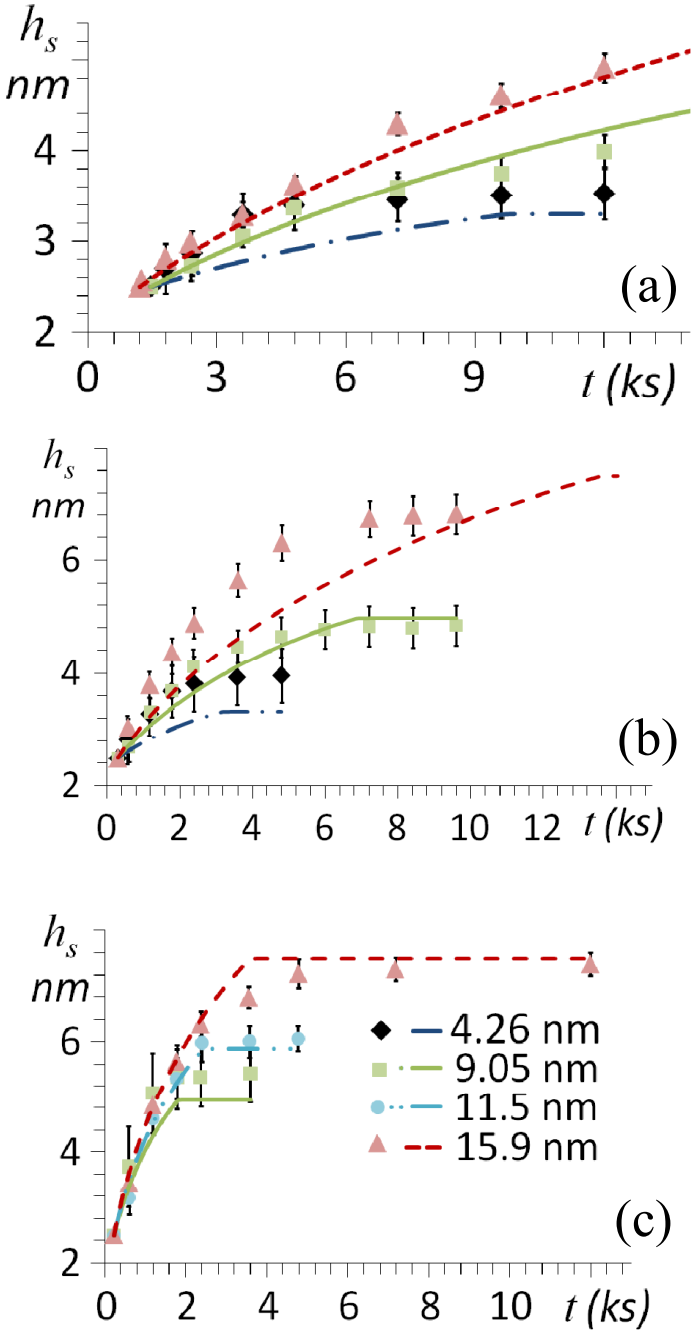

Figure 3.3 Oxide layer thickness vs. time for Cu NP of four different core radii: lines are results of simulations, and symbols are experiments from (4); (a) $\theta = 323\,K$, (b) $\theta = 343\,K$, and (c) $\theta = 373\,K$.

3.1.5.2 Pressure and vacancy distribution for solid core/shell structure

Distributions of concentration of vacancies in a solid core and Cu atoms in a shell are presented in Fig. 3.4 for $R_c = 9.05\,nm$ at $\theta = 373\,K$. Since Cu atoms diffuse to the shell and react with oxygen, vacancies are generated at the core/shell interface and diffuse to the core center. Both distributions increase in time until 16.5 s, and n_v at the center reaches $n_{eq} = 0.0154$ which is determined by Eq. (35).

The pressure distribution in core is slightly heterogeneous due to heterogeneous vacancy distribution and reduces from 0.71 to 0.68 GPa during 16.5 s due to increasing n_v. The pressure distribution in the shell is also slightly heterogeneous, and its maximum increases from 0.325 to 0.345 GPa due to increasing n_2.

Pressure and vacancy distribution for void growth stage. After n_v at the center reaches $n_{eq} = 0.0154$, a 4-vacancy nanovoid is introduced at the center of NP. The results are presented in Fig. 3.5. With increasing time, vacancies are absorbed by the growing void, and the core becomes smaller until all Cu atoms diffuse to the growing shell. Initially, the sharp reduction in n_v causes fast void growth, which decelerates with time (Fig. 3.6). Initial fast growth is caused by the strong reduction in equilibrium concentration of vacancies at the void surface with increasing void radius and by the small initial void size. The pressure is becoming more homogeneous in the core with increasing time and increases from the initial 0.716 GPa to 1.9 GPa at 1 ks. Note that pressure increases with growing a/R_c and decreases with growing R_s/R_c, but the former is larger than later. Such a pressure increase decreases the self-diffusion coefficient of Cu by a factor of 5. Also, pressure increases in the shell from the range 0.324-0.347 GPa to 0.461-0.484 GPa. Note that the pressure gradient term in diffusion equations promotes diffusion of Cu in the shell, but suppresses diffusion of vacancies. The resultant effect is promoting; when the pressure gradient term is neglected, time for formation of the maximum-size hole increases by 71 s.

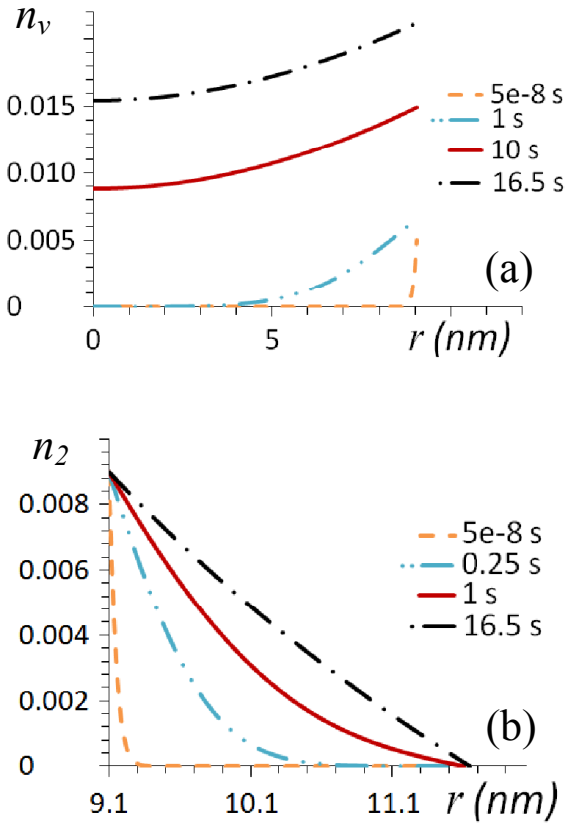

Figure 3.4 Evolution of distribution of vacancy concentration in a core and Cu atoms in a shell for $R_c = 9.05\,nm$ at $\theta = 373\,K$.

3.1.5.3 Hollow oxide

When the metal core disappears, the remnant Cu atoms in a shell diffuse to the outer surface and react with oxygen, until complete disappearance of Cu atoms. This process takes about 100 s with deceleration in time. Pressure reduces at the void surface from 0.515 to 0.499 GPa, increases at the external surface from 0.495 to 0.499 GPa, and finally becomes homogeneous. The final pressure is caused by surface tension.

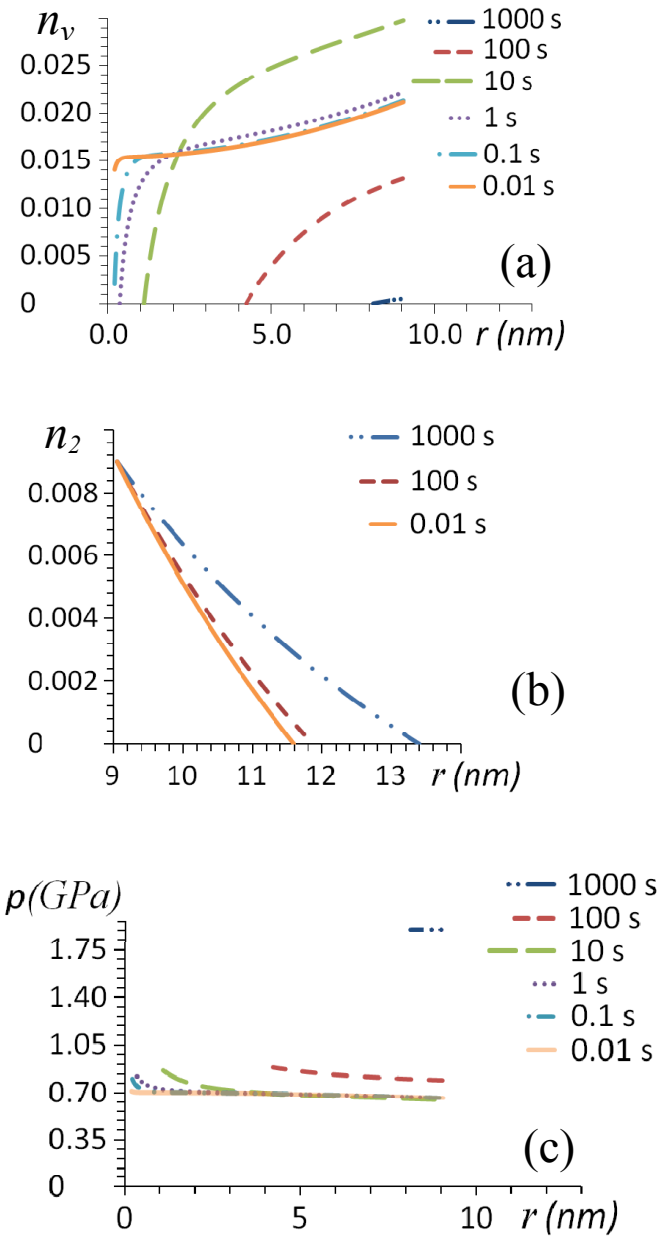

Figure 3.5 Evolution of distribution of vacancy concentration in a core (a) and Cu atoms in a shell (b), as well as pressure in a core (c) for $R_c = 9.05\,nm$ at $\theta = 373\,K$ during the nanovoid growth.

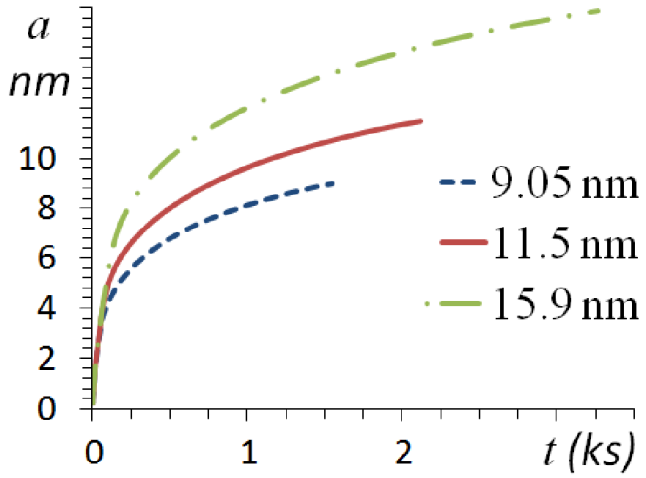

Figure 3.6 Variation of void radius vs. time for three particle sizes at $\theta = 373\,K$.

3.1.6 Comparison with existing approaches

There are several main differences between our approach and results and those in, [17, 18] which allowed us to obtain good comparison with experiments and to elucidate the void nucleation and growth mechanisms.

(1) In the general case, one has to include misfit volumetric strain due to chemical reaction, as. [17,18] In, [17,18] because of misfit strain and neglected compressive stresses due to surface tension, huge tensile stresses in a core (and compressive stresses in a shell) appeared, which led to the idea that they can cause void nucleation due to fracture. However, because in our problem the reaction occurs at the surface (rather than in bulk) and interface between metal and oxide is incoherent, internal stresses due to chemical reaction are negligible. For example, Al oxide shell is amorphous below some thickness (4 nm), and thus interface is incoherent and does not generate internal stresses. Even for crystalline shell, for Al particles with $R_c = 20$ to 40 nm and shell growing during chemical reaction to $m = 1.76$, lattice spacing in Al did not differ from that in bulk sample; [52] i.e., internal stresses are negligible. That is why we excluded misfit strain but included surface tension, which resulted in compressive pressure both in core and shell and in elimination of the fracture hypothesis.

(2) The suggested void nucleation criterion shows that, surprisingly, compressive pressure

promotes void nucleation.

(3) We took into account that the self-diffusion coefficient is proportional to the actual (rather than equilibrium) concentration of vacancies, which increased it at the initial stage by twelve orders of magnitude. We also took into account that the diffusion coefficient of metal in oxide at the nanoscale is much larger than in bulk material.

3.1.7 Concluding Remarks

A continuum mechanochemical approach for nucleation and growth of nanovoid in reacting NP is developed that treats explicitly void nucleation and the effects of stresses. A counterintuitive effect of pressure on nucleation is found. Experimental results for Cu NPs are described. Based on obtained results, the following regimes can be used to accelerate void formation and make it possible in micron-scale particles. Initially, high temperature at zero pressure should be applied to accelerate diffusion and reach the desired level of n_v. Then, temperature should be reduced, and pressure may be applied to reduce n_{eq} and cause void nucleation. After the void reaches the size corresponding to low-enough n_{eq}, pressure should be removed and temperature increased to accelerate diffusion. Accordingly, to suppress void nucleation by the above mechanism, one has to increase temperature and tensile pressure, and to suppress void growth, one has to reduce temperature and apply compressive pressure. A similar continuum framework can be used for modeling the nanotube fabrication based on the Kirkendall effect. [53] Note that it is understood that application of continuum methods to such small nuclei can be questioned. However, continuum concepts are successfully applied even to single vacancy (see [54] and the concept of the center of dilatation) and are routinely used in nucleation theory for a critical nucleus consisting of a few atoms (see examples in [19]).

Bibliography

[1] Hosokawa, M.; Nogi, K.; Naito, M.; Yokoyama, T. Nanoparticle technology handbook; Elsevier, 2007; p 100.

[2] Shpak, A. P.; Gorbyk, P. P. Nanomaterials and Supramolecular Structures: Physics, Chemistry, and Applications; Springer, 2009; p 207.

[3] Levitas, V. I.; Asay, B. W.; Son, S. F.; Pantoya, M. *J. Appl. Phys.* **2007**, 101, 083524.

[4] Yin, Y.; Rioux, R. M.; Erdonmez, C. K.; Hughes, S.; Somorjai, G. A.; Alivisatos, A. P. *Science* **2004**, 304, 711-714.

[5] Tokozakura, D.; Nakamura, R.; Nakajima, H.; Lee, J. G.; Mori, H. *J. Mater. Res.* **2007**, 22, 2930-2935.

[6] Hung, L. I; Tsung, C. K; Huang, W.; Yang, P. *Adv. Mater.* **2010**, 22, 1910-1914.

[7] Nakamura, R.; Tokozakura, D.; Nakajima, H.; Lee, J. G.; Mori, H. *J. Appl. Phys.* **2007**, 101, 074303.

[8] Wang, C. M.; Baer, D. R.; Thomas, L. E.; Amonette, J. E.; Antony, J.; Qiang, Y.; Duscher, G. *J. Appl. Phys.* **2005**, 98, 094308.

[9] Cabot, A.; Puntes, V. F.; Shevchenko, E.; Yin, Y.; Balcells, L.; Marcus, A. M.; Hughes, M.; Alivisatos, A. P. *J. Am. Chem. Soc.* **2007**, 129, 10358-10360.

[10] Yin, Y.; Erdonmez, C. K; Cabot, A.; Hughes, M.; Alivisatos, A. P. *Adv. Funct. Mater.* **2006**, 16, 1389-1399.

[11] Cabot, A.; Ibanez, M.; Guardia, P.; Alivisatos, A. P. *J. Am. Chem. Soc.* **2009**, 131, 11326-11328.

[12] Smigelskas, A. D; Kirkendall, E. O. *Trans. Am. Inst. Min. Metall. Eng.* **1947**, 171, 130-142.

[13] Evteev, A. V.; Levchenko, E. V.; Belova, I. V.; Murch, G. E. *J. Nano Res.* **2009**, 7, 11-17.

[14] Gusak, A. M; Zaporozhets, T. V. *Phys. Condens. Matter.* **2009**, 21, 415303.

[15] Yu, H. C.; Yeon, D. H.; Li, X. F.; Thornton, K. *Acta Mater.* **2009**, 57, 5348-5360.

[16] Gusak, A. M.; Tu, K. N. *Acta Mater.* **2009**, 57, 3367-3373.

[17] Svoboda, J.; Fischer, F. D.; Vollath, D. *Acta Mater.* **2009**, 57, 1912-1919.

[18] Zhdanov, V. P.; Kasemo, *B. Nano Lett.* **2009**, 9(5), 2172-2176.

[19] Levitas, V. I.; Altukhova, N. *Phys. Rev. Let.* **2008**, 101(14), 145703.

[20] Levitas, V. I.; Altukhova, N. *Phys. Rev. B* **2009**, 79(21), 212101.

[21] Levitas, V. I.; Altukhova, N. *Acta Mater.* **2011**, 59(18), 7051.

[22] Rokkam, S.; El-Azab, A.; Millett, P.; Wolf, D. *Modelling Simul. Mater. Sci. Eng.* **2009**, 17, 064002.

[23] Yu, H. C.; Lu, W. *Acta Mater.* **2005**, 53(6), 1799-1807.

[24] Levitas, V.I.; Idesman, A.V; Palakala, A. *J. Applied Physics* **2011**, 110(3), 033531.

[25] Railsback, J. G.; Johnston-Peck, A. C.; Wang, J. W.; Tracy, J. B. *ACS NANO.* **2010**, 4(4), 1913-1920.

[26] Larche, F. C; Cahn, J. W. *Acta Mater.* **1982**, 30, 1835-1845.

[27] Yang, F. *Mater. Sci. Eng. A* **2005**, 409, 153-159.

[28] Li, J. C. M. *Metall. Trans. A*, **1978**, 9A, 1353-1380.

[29] Balluffi, R. W.; Allen, S. M.; Carter, W. C.;Kemper, R. A. Kinetics of material; John Wiley, Hoboken, New Jersey, 2nd edition, 2005; p 24.

[30] Bakker, H.; Mehrer, H. Diffusion in solid metals and alloys; Springer, 1990; p 607.

[31] Svoboda, J.; Fischer, F. D.; Fratzl, P.; Kroupa, A. *Acta Mater.* **2002**, 50, 1369-1381.

[32] Larche, F. C.; Chan, J. W. *Acta Mater.* **1985**, 3, 331-357.

[33] Porter, D. A.; Eastirling, K. E. Phase transformation in metals and alloys; 2nd edition, Chapman and hall, London, 1992, p 45.

[34] Fischer, F. D.; Svoboda, J. *Scri Mater.* **2007**, 58, 93-95.

[35] Nemirovich-Danchenko, L. Y.; Lipnitski, A. G.; Kulkova, S. E. *Phys. Sol Stat.* **2007**, 49(6), 1079-1085.

[36] Ledbetter, H. M. *Phys. Stat. Sol.* **1981**, 66, 477-484.

[37] Ruiz, E.; Alvarez, S.; Alemany, P.; Evarestov, R. *Phys. Rev. B* **1997**, 56, 7189-7196.

[38] Nix, F. C.; MacNair, D. *Phys. Rev.* **1941**, 60, 597-605.

[39] Uno, R.; Okada, T. *J. Phys. Soc. Jpn.* **1950**, 5, 23-25.

[40] Zhang, X.; Shyy, W.; Sastry, A. M. *J. Elec. Soc.* **2007**, 154(10), A910.

[41] Rothman, S. J.; Peterson, N. L. *Phy. Stat. Sol. B* **1969**, 35, 305-312.

[42] Mishin, Y.; Mehl, M. J.; Papaconstantopoulos, D. A.; Voter, A. F.; Kress, J. D. *Phys. Rev.* **2001**, 63, 224106.

[43] Andersson, D. A; Simak, S. I. *Phy. Rev. B* **2004**, 70, 115108.

[44] Peterson, N. L.; Wiley, C. L. *J. Phys. Chem. Sol.* **1984**, 45(3), 281-294.

[45] Bergsmark, E.; Simensen, C. J.; Kofstad, P. *Mater. Sci. Eng. A* **1989**, 120, 91-95.

[46] Campbell, T. J.; Kalia, R. K.; Nakano, A.; Vashishta, P.; Ogata, S.; Rodgers, S. *Phys. Rev. Lett.* **1999**, 82, 4866-4869.

[47] Henz, B. J.; Hawa, T.; Zachariah, M. R. *J. Appl. Phys.* **2010**, 107, 024901.

[48] Rai, A.; Park, K.; Zhou, L.; Zachariah, M. R. *Combust. Theor. Model.* **2006**, 10(5), 843-859.

[49] Zhanga, X.; Lu, G. *Phys. Rev. B* **2008**, 77, 174102.

[50] Lai, W. M.; Rubin, D.; Krempl, E. Introduction to Continuum Mechanics; Pergamon Press Ltd, 1993; p 291.

[51] Fischer, F. D.; Svoboda, J. *Int J. Solid Structure.* **2010**, 47(20), 2799-2805.

[52] Mei, Q. S.; Wang, S. C.; Cong, H. T.; Jin, Z. H.; Lu, K. *Acta Mater.* **2005**, 53, 1059-1066.

[53] Fan, H. J.; Knez, M.; Scholz, R.; Nielsch, K.; Pippel, E.; Hesse, D.; Zacharias, M.; Gosels, D. *Nat. Mater.* **2006**, 5, 626-631.

[54] Li, S.; Sellers, M. S.; Basaran, C.; Schultz, A. J.; Kofke, D. A. *Int. J. Mol. Sci.* **2009**, 10, 2798-2808.

CHAPTER 4. GENERAL CONCLUSIONS

Li-ion batteries: In Chapter 2 several conceptual advancements in diffusion and stress relaxation based on a thermodynamically consistent approach were introduced. This nonlinear approach was applied to analyze stress generation during lithiation/delithiation in a nanoscale amorphous Si anode. Generally the amorphous Si is considered as an isotropic material however, the compositional expansion/contraction strain can be anisotropic that the source of this anisotropy is deviatoric stresses. Based on this concept, a new dissipative term added to dissipation inequality and an additional term appears in the chemical potential. It was shown that the effect of deviatoric stresses on chemical potential increases the driving force for both processes, i.e., lithiation/delithiation. Applying a postulate of realizability, a linear kinetic equation for stress relaxation was also derived. This formula connects the deviatoric part of compositional stress to deviatoric compositional deformation rate through a constant (stress relaxation parameter). This new stress relaxation mechanism has two advantages compared to a viscoplastic model. First, one can employ this model to relax the stress even below the yield stress. Second, only a single scalar parameter is needed to reproduce the induced stresses in experimental studies; however, the viscoplastic model requires two material parameters as well as the yield strength as a function of Li concentration. Based on this theoretical framework, we proposed to relax the internal stresses by cyclic lithiation/delithiation with small magnitude. Additionally, the stress evolution was modeled for different nanostructures (thin film, solid, and hollow nanoparticle) during lithiation-delithiation. The calculated stress level shows that amorphous hollow nanopaticles are good candidates for anodes. Finally, the results were compared with known experimental and atomistic simulation data.

Hollow formation: Chapter 3 develops a coupled continuum mechanics approach based on the Kirkendall effect to model nucleation and growth of a nanovoid in reacting NPs. This model

includes the effect of stress on void nucleation and diffusion. The results show that the core is under compression due to surface stress. This eliminates a fracture hypothesis and promotes void nucleation by decreasing equilibrium concentration of vacancies at the void surface. The model was checked by the available experiments. The effect of pressure on void nucleation suggests using a thermo-mechanical method to control the hollow formation. One can control the synthesis process by controlling the pressure and temperature in different stages of oxidation to accelerate/decelerate the formation of hollow nanoparticles.

APPENDIX A. DERIVATION OF THE CONSTITUTIVE EQUATION FOR $\boldsymbol{k}$ USING THE POSTULATE OF REALIZABILITY

We start first with deriving the equation for $\boldsymbol{k}$ from the consideration of the chemical potential, then from the the compositional dissipation rate, and we show that the results coincide. Let us consider reservoir of A atoms with a chemical potential μ_r in contact with A_xB sample with chemical potential $\mu(\mathcal{B}, \boldsymbol{k}^*)$, where $\mathcal{B}$ is the set of all parameters affecting the chemical potential (e.g., p_0, $\bar{\boldsymbol{S}}$, x, ...). Tensor $\boldsymbol{k}^*$ designates all possible directing tensors, which are considered as free parameters, among which the actual tensor $\boldsymbol{k}$ is to be chosen. We designate $\Delta\mu(\mathcal{B}, \boldsymbol{k}^*) := \mu_r - \mu(\mathcal{B}, \boldsymbol{k}^*)$. The A_xB sample is assumed to be small enough so that heterogeneities of all parameters can be neglected. Let the magnitude of the flux of A to the sample be described by experimentally determined monotonous function $j = f(\Delta\mu(\mathcal{B}, \boldsymbol{k}))$–e.g., $j = b(\mathcal{B})\overline{V}_B^{-1} x \Delta\mu(\mathcal{B}, \boldsymbol{k})/\Delta y$–with the size Δy of the order of magnitude of the size of a sample.

Insertion. We will consider the possibility of the A transport to the A_xB sample with the arbitrarily prescribed magnitude of the flux j. Due to equation $j = f(\Delta\mu(\mathcal{B}, \boldsymbol{k}))$, this means that the magnitude of $\Delta\mu(\mathcal{B}, \boldsymbol{k})$ is prescribed as well, and it will be designated as $\Delta\mu_0$. Plot $\Delta\mu(\mathcal{B}, \boldsymbol{k}^*)$ vs. $\boldsymbol{k}^*$ for arbitrary fixed parameters $\mathcal{B}$ is schematically shown in Fig. A.1.

We assume that this function has a maximum value $\Delta\mu_{max}(\mathcal{B})$ corresponding to some $\boldsymbol{k}$ for each $\mathcal{B}$, which is clear from the definition in Eq. (35). To find an actual directing tensor $\boldsymbol{k}$ among all possible $\boldsymbol{k}^*$, we will apply the *postulate of realizability* formulated in realizability-I,realizability-II (see also Section 3.2). We will use the following formulation:

If A transport from A reservoir to A_xB small volume with a prescribed magnitude of the flux j can occur, it will occur.

Let us fix j and all parameters $\mathcal{B}$ in such a way that $\Delta\mu(\mathcal{B}, \boldsymbol{k}^*) < \Delta\mu_0$ for all $\boldsymbol{k}^*$,–i.e., horizontal line $\Delta\mu_0$ is above the curve $\Delta\mu(\mathcal{B}, \boldsymbol{k}^*)$–and A transport from A reservoir to A_xB

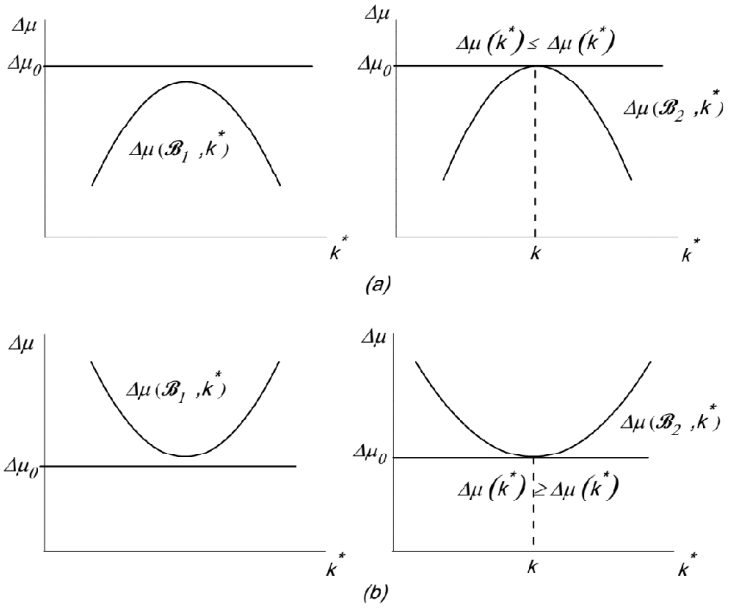

Figure A.1 Variation of $\Delta\mu(\mathcal{B}, \boldsymbol{k}^*)$ vs. $\boldsymbol{k}^*$ for arbitrarily fixed parameters $\mathcal{B}$ for insertion (a) and extraction (b).

small volume cannot occur with a magnitude of the flux j. Let us continuously change $\mathcal{B}$ or μ_r in order to increase $\Delta\mu(\mathcal{B}, \boldsymbol{k}^*)$. A transport from A reservoir with a magnitude of the flux j can occur when the curve $\Delta\mu(\mathcal{B}, \boldsymbol{k}^*)$ and the horizontal line $\Delta\mu_0$ have common points, so that $\Delta\mu(\mathcal{B}, \boldsymbol{k}^*) = \Delta\mu_0$ for some of $\boldsymbol{k}^*$. The first time this happens is when $\Delta\mu_0 = \Delta\mu_{max}(\mathcal{B})$– i.e., when the curve $\Delta\mu(\mathcal{B}, \boldsymbol{k}^*)$ and line $\Delta\mu_0$ touch. Then, according to the postulate of realizability, A transport from A reservoir to A_xB small volume with a prescribed magnitude of the flux j will occur. Thus, actual $\boldsymbol{k}$ corresponds to the $\Delta\mu_{max}(\mathcal{B})$–i.e., an extremum principle of the maximum driving force for the A transport is valid:

$$\Delta\mu(\mathcal{B}, \boldsymbol{k}^*) \;\; \rightarrow \max_{\boldsymbol{k}^*}; \quad \Delta\mu(\mathcal{B}, \boldsymbol{k}^*) \leq \Delta\mu(\mathcal{B}, \boldsymbol{k}) \;\; \forall \boldsymbol{k}^*. \tag{1}$$

Since in Eq. (35) $sign(\dot{x}) > 0$, $H > 0$, and $J > 0$, the extremum principle (1) is equivalent to

$$\bar{\boldsymbol{S}}{:}\boldsymbol{k}^* \;\; \rightarrow \max_{\boldsymbol{k}^*}; \quad \bar{\boldsymbol{S}}{:}\boldsymbol{k} \geq \bar{\boldsymbol{S}}{:}\boldsymbol{k}^* \;\; \forall \boldsymbol{k}^*. \tag{2}$$

Maximizing expression (2) for $\bar{\boldsymbol{S}}{:}\boldsymbol{k}^*$ with respect to $\boldsymbol{k}^*$, we obtain collinearity of $\boldsymbol{k}$ and $\bar{\boldsymbol{S}}$, see Eqs. (36) and (37).

Extraction. Consider the extraction (e.g., delithiation) process–i.e., $\dot{x} < 0$. Plot $\Delta\mu(\mathcal{B}, \boldsymbol{k}^*)$ vs. $\boldsymbol{k}^*$ for arbitrary fixed parameters $\mathcal{B}$ has the minimum value $\Delta\mu_{min}(\mathcal{B})$ corresponding to some $\boldsymbol{k}$ for each $\mathcal{B}$ (Fig. A.1b). The *postulate of realizability* is formulated as follows:
If A transport from A_xB small volume to A reservoir with a prescribed magnitude of the flux j can occur, it will occur.

Let us fix j and all parameters $\mathcal{B}$ in such a way that $\Delta\mu(\mathcal{B}, \boldsymbol{k}^*) > \Delta\mu_0$ for all $\boldsymbol{k}^*$–i.e., horizontal line $\Delta\mu_0$ is below the curve $\Delta\mu(\mathcal{B}, \boldsymbol{k}^*)$ and A transport from A_xB small volume to A reservoir cannot occur with a magnitude of the flux j. Let us continuously change $\mathcal{B}$ or μ_r in order to decrease $\Delta\mu(\mathcal{B}, \boldsymbol{k}^*)$. A transport to A reservoir with a magnitude of the flux j can occur when the curve $\Delta\mu(\mathcal{B}, \boldsymbol{k}^*)$ and the horizontal line $\Delta\mu_0$ have common points, so that $\Delta\mu_0 = \Delta\mu(\mathcal{B}, \boldsymbol{k}^*)$ for some of $\boldsymbol{k}^*$. The first time this happens is when $\Delta\mu_0 = \Delta\mu_{min}(\mathcal{B})$–i.e., when the horizontal line $\Delta\mu_0$ and the curve $\Delta\mu(\mathcal{B}, \boldsymbol{k}^*)$ touch. Then, according to the postulate of realizability, A transport from A_xB small volume to A reservoir with a prescribed magnitude of the flux j will occur. Thus, actual $\boldsymbol{k}$ corresponds to the $\Delta\mu_{min}(\mathcal{B})$–i.e., an extremum principle of minimum driving force for the A transport is valid:

$$\Delta\mu(\mathcal{B}, \boldsymbol{k}^*) \;\; \rightarrow \min_{\boldsymbol{k}^*}; \quad \Delta\mu(\mathcal{B}, \boldsymbol{k}^*) \geq \Delta\mu(\mathcal{B}, \boldsymbol{k}) \;\; \forall \boldsymbol{k}^*. \tag{3}$$

Since in Eq. (35) $sign(\dot{x}) < 0$, $H > 0$, and $J > 0$, the extremum principle (3) is equivalent to the principle (2), which leads to the same Eqs. (36)-(37). Extremum principles Eq. (1) and Eq. (3) can be combined in the principle of the maximum magnitude of the driving force for the A transport, which is valid for both insertion and extraction:

$$|\Delta\mu(\mathcal{B}, \boldsymbol{k}^*)| \;\; \rightarrow \max_{\boldsymbol{k}^*}; \quad |\Delta\mu(\mathcal{B}, \boldsymbol{k}^*)| \leq |\Delta\mu(\mathcal{B}, \boldsymbol{k})| \;\; \forall \boldsymbol{k}^*, \tag{4}$$

APPENDIX B. APPLICATION OF THE POSTULATE OF REALIZABILITY TO COMPOSITIONAL DISSIPATION RATE

While Eqs. (36) and (37) completely determine the compositional dissipation rate, we will apply the postulate of realizability to rederive equation for $\boldsymbol{k}$ for two reasons: (1) for $\zeta = 1$, there is no contribution of $\boldsymbol{k}$ to the chemical potential, and the above derivation is not valid; (2) for $\zeta < 1$, we would like to check whether application of the postulate of realizability to the compositional dissipation rate gives the same results as for its application to the chemical potential.

We assume that functions $\zeta(\bar{\boldsymbol{S}}, x)$ and $H(\bar{\boldsymbol{S}}, x, |\dot{x}|)$ are known from experiment or atomistic simulations; rate $\dot{x}$ is prescribed, and our main task now is to find $\boldsymbol{k}$ for any given $\bar{\boldsymbol{S}}$. Let us consider the possibility of the occurrence of the compositional dissipation rate with an arbitrary prescribed value $\mathcal{D}_{c0}$. We start with deviatoric stress $\bar{\boldsymbol{S}}$, for which $\zeta J \bar{\boldsymbol{S}}{:}\boldsymbol{k}^* H(\bar{\boldsymbol{S}}, x, |\dot{x}|)|\dot{x}| < \mathcal{D}_{c0}$ for all $\boldsymbol{k}^*$, so that the compositional deformation rate with the dissipation rate $\mathcal{D}_{c0}$ is impossible. We will apply the postulate of realizability in the following formulation:

As soon as the compositional deformation rate with the prescribed value of the dissipation rate $\mathcal{D}_{c0}$ is possible, it will occur at the first chance.

We change $\bar{\boldsymbol{S}}$ continuously and check all possible $\boldsymbol{k}^*$. The first possibility to have a compositional deformation rate with the dissipation rate $\mathcal{D}_{c0}$ is the first fulfilment of the equality $\zeta J \bar{\boldsymbol{S}}{:}\boldsymbol{k} H(\bar{\boldsymbol{S}}, x, |\dot{x}|)|\dot{x}| = \mathcal{D}_{c0}$ for one of the $\boldsymbol{k}$. According to the postulate of realizability, this opportunity should be realized, and it can be realized with this $\boldsymbol{k}$ only because for all other $\boldsymbol{k}^*$ we have inequality. Thus,

$$\zeta J \bar{\boldsymbol{S}}{:}\boldsymbol{k} H(\bar{\boldsymbol{S}}, x, |\dot{x}|)|\dot{x}| = \mathcal{D}_c \geq \zeta J \bar{\boldsymbol{S}}{:}\boldsymbol{k}^* H(\bar{\boldsymbol{S}}, x, |\dot{x}|)|\dot{x}|, \quad \rightarrow \quad \bar{\boldsymbol{S}}{:}\boldsymbol{k} \geq \bar{\boldsymbol{S}}{:}\boldsymbol{k}^* \qquad \forall \boldsymbol{k}^*. \tag{1}$$

Extremum principle (1) coincides with that in Eq. (2) and consequently results in the same

Eqs. (36)-(39). Thus, both formulations give equivalent solutions.

APPENDIX C. CHOICE OF THE GENERALIZED THERMODYNAMIC FORCES AND RATES

The choice of the generalized thermodynamic forces and rates in the expression $\mathcal{D}_c := \zeta J \bar{\boldsymbol{S}}{:}\boldsymbol{d}_c^S$ is not unique. In particular, we obtain

$$\bar{\boldsymbol{S}}{:}\boldsymbol{d}_c^S = \bar{\boldsymbol{S}}{:}\boldsymbol{F}_e{\cdot}\dot{\boldsymbol{U}}_c^S{\cdot}\boldsymbol{U}_c^{S-1}{\cdot}\boldsymbol{F}_e^{-1} = \boldsymbol{U}_c^{S-1}{\cdot}\boldsymbol{F}_e^{-1}{\cdot}\bar{\boldsymbol{S}}{\cdot}\boldsymbol{F}_e{:}\dot{\boldsymbol{U}}_c^S = \boldsymbol{F}_e^{-1}{\cdot}\bar{\boldsymbol{S}}{:}\boldsymbol{F}_e{\cdot}\dot{\boldsymbol{U}}_c^S{\cdot}\boldsymbol{U}_c^{S-1}. \tag{1}$$

First, we can postulate the relationship between generalized stress $(\boldsymbol{U}_c^{S-1}{\cdot}\boldsymbol{F}_e^{-1}{\cdot}\bar{\boldsymbol{S}}{\cdot}\boldsymbol{F}_e)_s$ and the conjugate rate $\dot{\boldsymbol{U}}_c^S$, or between $\boldsymbol{F}_e^{-1}{\cdot}\bar{\boldsymbol{S}}{\cdot}\boldsymbol{F}_e$ and $\dot{\boldsymbol{U}}_c^S{\cdot}\boldsymbol{U}_c^{S-1}$. While in principle Eq. (37) can be reduced to the relationship between these new generalized stresses and rate and some additional tensors, if we apply the postulate of realizability to the relationship between these new conjugate variables the results will be different. Thus, the choice of the generalized thermodynamic forces and rates in the expression for the dissipation rate is an additional hypothesis. The convenience of $\bar{\boldsymbol{S}}$ and $\boldsymbol{d}_c^S$ is that they have the same structure–i.e., they are both deviators– and the simplest proportionality between them, $\boldsymbol{d}_c^S = \kappa\boldsymbol{S}$, is not contradictory. What is more important is that it corresponds to experiments (see below). In contrast, the relationship $\dot{\boldsymbol{U}}_c^S = \kappa(\boldsymbol{U}_c^{S-1}{\cdot}\boldsymbol{F}_e^{-1}{\cdot}\bar{\boldsymbol{S}}{\cdot}\boldsymbol{F}_e)_s$ is contradictory because in the double contraction of this equation with $\boldsymbol{U}_c^{S-1}$ the left side $\dot{\boldsymbol{U}}_c^S{:}\boldsymbol{U}_c^{S-1} = 0$, but the right side $(\boldsymbol{U}_c^{S-1}{\cdot}\boldsymbol{F}_e^{-1}{\cdot}\bar{\boldsymbol{S}}{\cdot}\boldsymbol{F}_e)_s{:}\boldsymbol{U}_c^{S-1} \neq 0$. The alternative choice $\dot{\boldsymbol{U}}_c^S{\cdot}\boldsymbol{U}_c^{S-1} = \kappa\boldsymbol{F}_e^{-1}{\cdot}\bar{\boldsymbol{S}}{:}\boldsymbol{F}_e$ (assuming that the right-hand side is nonsymmetric) prescribes not only $(\dot{\boldsymbol{U}}_c^S{\cdot}\boldsymbol{U}_c^{S-1})_s$ but also $(\dot{\boldsymbol{U}}_c^S{\cdot}\boldsymbol{U}_c^{S-1})_a$, which gives three more equations than required. Indeed, we assume that we can neglect the anisotropy of the elasticity rule due to $\boldsymbol{U}_c$ and $\boldsymbol{U}_p$ and $\bar{\boldsymbol{S}} = \boldsymbol{S}$. Then, using the polar decomposition $\boldsymbol{F}_e = \boldsymbol{R}_e{\cdot}\boldsymbol{U}_e$, we have

$$\boldsymbol{F}_e^{-1}{\cdot}\boldsymbol{S}{:}\boldsymbol{F}_e{\cdot}\dot{\boldsymbol{U}}_c^S{\cdot}\boldsymbol{U}_c^{S-1} = \boldsymbol{U}_e^{-1}{\cdot}\boldsymbol{R}_e^t{\cdot}\boldsymbol{S}{\cdot}\boldsymbol{R}_e{\cdot}\boldsymbol{U}_e{:}\dot{\boldsymbol{U}}_c^S{\cdot}\boldsymbol{U}_c^{S-1} = \boldsymbol{R}_e^t{\cdot}\boldsymbol{S}{\cdot}\boldsymbol{R}_e{:}\dot{\boldsymbol{U}}_c^S{\cdot}\boldsymbol{U}_c^{S-1} = \boldsymbol{S}{:}\boldsymbol{R}_e{\cdot}(\dot{\boldsymbol{U}}_c^S{\cdot}\boldsymbol{U}_c^{S-1})_s{\cdot}\boldsymbol{R}_e^t, \tag{2}$$

where we take into account the facts that for the isotropic elasticity rule $\boldsymbol{R}_e^t{\cdot}\boldsymbol{S}{\cdot}\boldsymbol{R}_e = \boldsymbol{f}_e(\boldsymbol{U}_e)$ tensors $\boldsymbol{R}_e^t{\cdot}\boldsymbol{S}{\cdot}\boldsymbol{R}_e$ and $\boldsymbol{U}_e$ have the same principle axes and $\boldsymbol{U}_e$ and $\boldsymbol{U}_e^{-1}$ eliminate each other. Also,

due to the symmetry of $\boldsymbol{R}_e^t \cdot \boldsymbol{S} \cdot \boldsymbol{R}_e$, the conjugate rate should also be symmetric. Thus, accepting $\dot{\boldsymbol{U}}_c^S \cdot \boldsymbol{U}_c^{S-1} = \kappa \boldsymbol{F}_e^{-1} \cdot \bar{\boldsymbol{S}} : \boldsymbol{F}_e$ for the weakly anisotropic elastic rule, we obtain $(\dot{\boldsymbol{U}}_c^S \cdot \boldsymbol{U}_c^{S-1})_a = 0$ in the limit of isotropic elasticity. This is a redundant and contradictory equation, which in general cannot be satisfied because $\dot{\boldsymbol{U}}_c^S$ is a symmetric tensor, which is completely determined by $(\dot{\boldsymbol{U}}_c^S \cdot \boldsymbol{U}_c^{S-1})_s$.

On the other hand, for isotropic elasticity, according to Eq. (2), $\boldsymbol{S}$ and $\bar{\boldsymbol{d}}_c^S := \boldsymbol{R}_e \cdot (\dot{\boldsymbol{U}}_c^S \cdot \boldsymbol{U}_c^{S-1})_s \cdot \boldsymbol{R}_e^t$ are the conjugate stress and compositional deformation rates, respectively, which possess the same properties as $\bar{\boldsymbol{S}}$ and $\boldsymbol{d}_c^S$ considered above. Also, application of the postulate of realizability results in $\boldsymbol{S} = \kappa \bar{\boldsymbol{d}}_c^S$, which is, however, not completely equivalent to $\bar{\boldsymbol{S}} = \kappa \boldsymbol{d}_c^S$ when tensors $\boldsymbol{U}_e$ and $\boldsymbol{U}_c$ are not coaxial. The logical advantage of using $\bar{\boldsymbol{S}}$ and $\boldsymbol{d}_c^S$ is that it is justified for the anisotropic elasticity rule and is not contradictory for the isotropic elasticity rule. Utilization of $\boldsymbol{S}$ and $\bar{\boldsymbol{d}}_c^S$ is valid for the isotropic elasticity rule only and does not coincide with the limit case, which can be obtained from the general expression for the anisotropic elasticity rule when anisotropy disappears.

APPENDIX D. SMALL ELASTIC STRAIN APPROXIMATION FOR A THIN FILM AT RIGID SUBSTRATE: ANALYTICAL SOLUTION

Using Eq. (87) and $\varepsilon_2^L = 0$, we obtain for in-plane strain

$$\varepsilon_{c2}^L = -\varepsilon_{e2}^L. \tag{1}$$

For small elastic strains, equations can be significantly simplified. First, in Eq. (87) we can substitute logarithmic strain with linear strain, $\boldsymbol{\varepsilon}_e = \boldsymbol{U}_e - \boldsymbol{I}$ and $\boldsymbol{\varepsilon}_c = \boldsymbol{U}_c - \boldsymbol{I}$ with $\boldsymbol{\varepsilon}_e \ll \boldsymbol{I}$ and $\boldsymbol{\varepsilon}_c \ll \boldsymbol{I}$. However, we will keep logarithmic strain where necessary in order not to violate some limit cases (see below). Since $\sigma_3 = 0$ and $J_e \simeq 1$, the elasticity rule for in-plane stress simplifies to

$$\sigma_2 = \frac{E}{1-\nu}\varepsilon_{e2} = -\frac{E}{1-\nu}\varepsilon_{c2}^L. \tag{2}$$

Equation (27) for in-plane direction reduces to

$$\frac{\dot{U}_{c2}}{U_{c2}} = \dot{\varepsilon}_{c2}^L = \frac{\dot{U}_{c2}^S}{U_{c2}^S} + \frac{\dot{J}_c}{3J_c}. \tag{3}$$

Substituting Eq. (3) into kinetic Eq. (52) for the principle axis 2,

$$\frac{\dot{U}_{c2}^S}{U_{c2}^S} = \frac{\Lambda}{3}\sigma_2 \dot{J}_c sign(\dot{J}_c), \tag{4}$$

we obtain

$$\dot{\varepsilon}_{c2}^L = \frac{\Lambda}{3}\sigma_2 \dot{J}_c sign(\dot{J}_c) + \frac{\dot{J}_c}{3J_c} = -\frac{\Lambda E}{3(1-\nu)}\varepsilon_{c2}^L \dot{J}_c sign(\dot{J}_c) + \frac{\dot{J}_c}{3J_c}. \tag{5}$$

This differential equation can be simplified to

$$\frac{d\varepsilon_{c2}^L}{dJ_c} = -\frac{\Lambda E}{3(1-\nu)}\varepsilon_{c2}^L sign(\dot{J}_c) + \frac{1}{3J_c}. \tag{6}$$

The analytical solution for constant $E/(1-\nu)$ is

$$\varepsilon_{c2}^{L} = \tfrac{1}{3} exp\left(-\tfrac{J_c E\Lambda}{3(1-\nu)}\right)\left[-ExpIntegralEi[\tfrac{E\Lambda}{3(1-\nu)}] + ExpIntegralEi[\tfrac{J_c E\Lambda}{3(1-\nu)}]\right] \tag{7}$$

for lithiation and

$$\varepsilon_{c2}^{L} = \tfrac{1}{3} exp\left(\tfrac{J_c E\Lambda}{3(1-\nu)}\right)\left[-ExpIntegralEi[\tfrac{E\Lambda}{3(1-\nu)}] + ExpIntegralEi[\tfrac{J_c E\Lambda}{3(1-\nu)}]\right] \tag{8}$$
$$ExpIntegralEi(x) := \textstyle\int_{-\infty}^{x} \frac{e^t}{t} dt = const + \ln|x| + \sum_{k=1}^{\infty} \frac{x^k}{k k!}\,.$$

for delithiation. For the case with no relaxation $\Lambda = 0$, the analytical solution is simplified to $\varepsilon_{c2}^{L} = \frac{1}{3}\ln(J_c)$, which is true for large strain as well. This was the reason why we kept logarithmic strains for small-strain approximation. The in-plane compositional logarithmic strain and biaxial stress for different Λ and constant mechanical properties ($E = 90$ GPa and $\nu = 0.28$) are plotted in Fig. D.1. The plot for stress has a shape similar to that for x-dependent E in Fig. 2.4. Increasing Λ reduces the in-plane compositional strain and consequently decreases the biaxial stress.

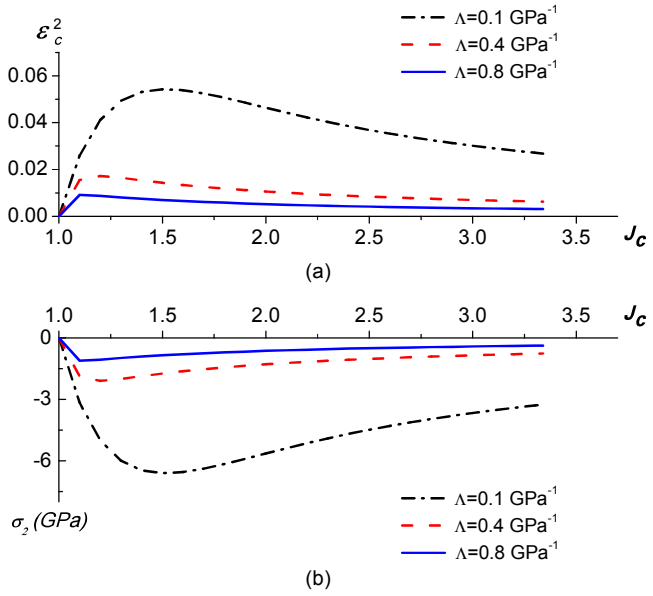

Figure D.1 In-plane compositional strain ε_{c2}^{L} (a) and biaxial stress (b) vs. compositional Jacobian for different Λ for lithiation.